Proton-Knockout Reactions from Neutron-Rich N Isotopes at R^3B

Proton-Knockout Reaktionen an neutronenreichen N Isotopen mit R^3B
vom Fachbereich Physik der Technischen Universität Darmstadt
zur Erlangung des Grades eines Doktors der Naturwissenschaften (Dr. rer. nat.)
genehmigte Dissertation von Ina Josephine Syndikus aus Offenbach am Main
Darmstadt 2018 — D 17

1. Gutachten: Marina Petri, PhD
2. Gutachten: Prof. Dr. rer. nat. Thomas Aumann

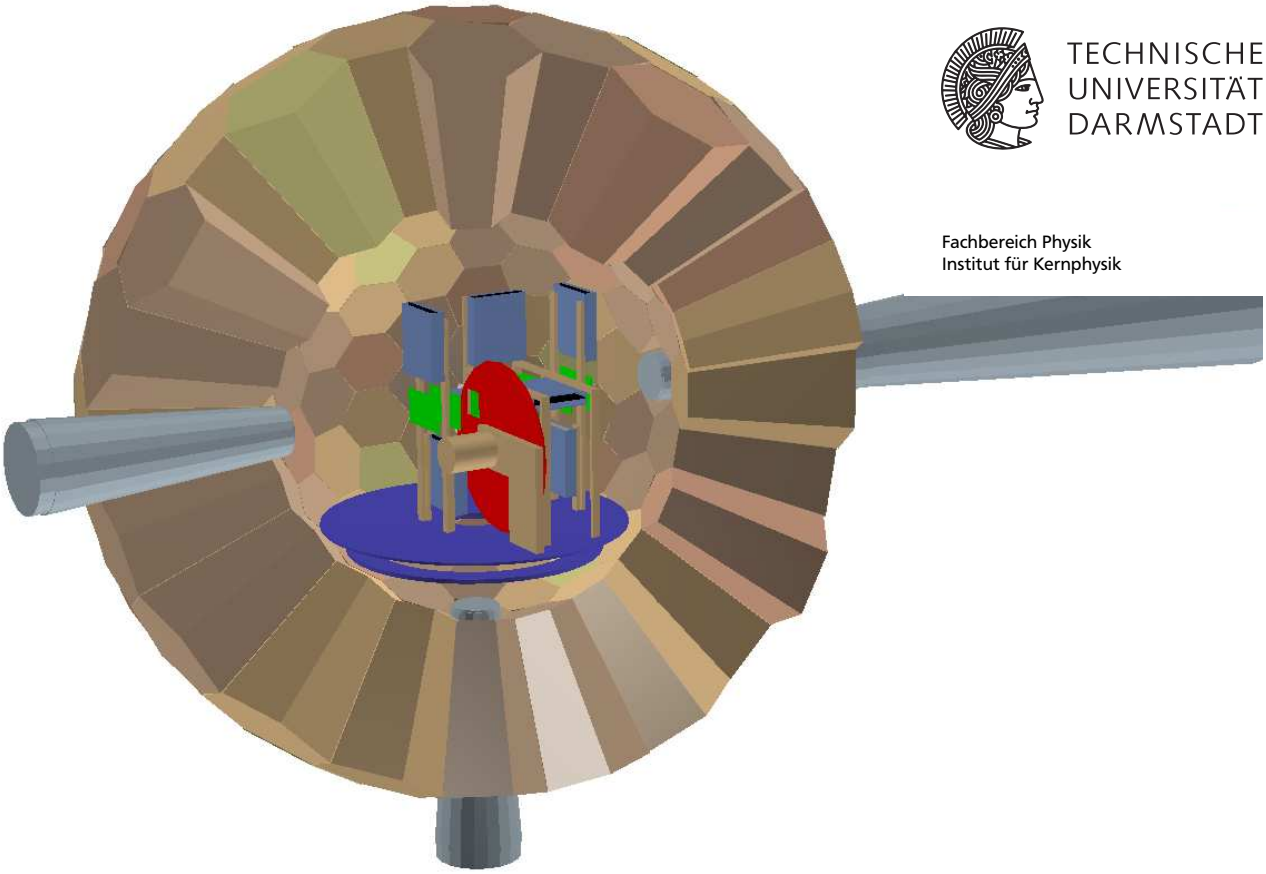

TECHNISCHE UNIVERSITÄT DARMSTADT

Fachbereich Physik
Institut für Kernphysik

GSI

HGS-HIRe for FAIR
Helmholtz Graduate School for Hadron and Ion Research

R3B

Proton-Knockout Reactions from Neutron-Rich N Isotopes at R^3B
Proton-Knockout Reaktionen an neutronenreichen N Isotopen mit R^3B

Genehmigte Dissertation von Ina Josephine Syndikus aus Offenbach am Main

1. Gutachten: Marina Petri, PhD
2. Gutachten: Prof. Dr. rer. nat. Thomas Aumann

Tag der Prüfung: 21.November 2018
Veröffentlichung auf TUprints: 2019

Darmstadt, Technischen Universität Darmstadt — D 17

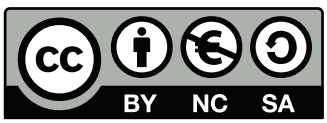

Es ist der Reiz des Lebens, dass man nicht alles für selbstverständlich hält, sondern noch bereit ist, sich zu wundern.
Loriot

Abstract

One-proton knockout reactions from neutron-rich ^{17}N, ^{19}N, and ^{21}N isotopes have been performed in inverse kinematics at the R^{3}B/LAND setup at GSI in Darmstadt during the experimental campaign S393. They have been measured in a kinematically complete way with a beam energy of 490 AMeV.

This thesis presents the inclusive and exclusive cross sections of Quasi-Free Scattering (QFS) and knockout reactions and compares them with calculations in the Glauber framework. The results are interpreted in a configuration mixing model describing the first excited 2^+_1 state of the fragments as a mixture of a pure proton and a pure neutron excitation. The comparison of the experimental and theoretical cross sections shows that this description is missing short- and long-range correlations. Furthermore, the proton amplitude for the neutron-rich, even-even ^{16}C, ^{18}C, and ^{20}C isotopes is extracted from the ratio of the exclusive cross sections of the first excited 2^+_1 state and the 0^+ ground state of the QFS reactions. The results support the two-state mixing picture. The behavior of the proton amplitude can be explained by the reduction of the spin-orbit splitting of the $1p_{1/2}$ and $1p_{3/2}$ proton orbit as an effect of the tensor force between the protons and the neutrons in the *sd* shell. Moreover, it helps to understand the increase of the $B(E2; 2^+_1 \rightarrow 0^+_{\text{g.s.}})$ quadrupole transition strength towards the neutron-rich ^{20}C isotope.

The analysis leading to these results is presented in detail. This includes the identification of the incoming and outgoing particles as well as a discussion of several addback algorithms to reconstruct the γ-ray energies. The number of recorded events and problems with the triggering are identified as the main sources for the experimental uncertainties. The γ-ray spectra are compared to simulations. The simulations have been performed in R3BRoot, a software package making use of the GEANT toolkit dedicated to experiments with the R^{3}B setup. In this context, the proton and γ-ray detection efficiencies of the Crystal Ball detector are discussed.

In addition, two position sensitive silicon prototype detectors which will be used as in-beam tracking detectors in the updated R^{3}B setup have been tested at KVI-CART. Their performance, i.e., their energy and position resolution, is investigated in terms of the integration time of the electronic read out. While the energy resolution is best for large integration times, the position resolution improves with decreasing integration time. These findings are discussed in terms of the noise introduced by the resistive surface of the detectors and the resulting pulse shapes.

Zusammenfassung

Während der S393 Kampagne wurden am R^3B/LAND Aufbau an der GSI in Darmstadt Proton-Knockout Reaktionen an den neutronenreichen Isotopen ^{17}N, ^{19}N und ^{21}N in inverser Kinematik kinematisch vollständig gemessen. Die Reaktionen fanden bei einer Strahlenergie von 490 AMeV statt.

Diese Arbeit präsentiert die Ergebnisse der inklusiven und exklusiven Wirkungsquerschnitte für Quasi-Freie Streuung (QFS) und Knockout-Reaktionen und vergleicht sie mit Berechnungen im Glauber-Modell. Die Ergebnisse werden im Rahmen des Configuration Mixing Modells interpretiert, welches den ersten angeregten 2_1^+ Zustand des Fragments als Mischung einer reinen Protonen- und einer reinen Neutronenanregung beschreibt. Der Vergleich der experimentellen und der theoretischen Wirkungsquerschnitte zeigt, dass diese Beschreibung sowohl kurz- als auch langreichweitige Korrelationen nicht ausreichend berücksichtigt. Zusätzlich wird die Protonenamplitude der neutronenreichen, gerade-gerade Isotope ^{16}C, ^{18}C und ^{20}C aus dem Verhältnis der exklusiven Wirkungsquerschnitte des ersten angeregten 2_1^+ Zustandes und des 0^+ Grundzustandes ermittelt. Die Ergebnisse bestätigen das Bild der sich mischenden Zustände. Der Anstieg der Protonenamplitude für neutronenreichere Kerne kann erklärt werden durch die Reduktion der Spin-Orbit-Aufspaltung zwischen dem $1p_{1/2}$ und dem $1p_{3/2}$ Orbital der Protonen, die durch die Tensorkraft zwischen den Protonen und den Neutronen in der *sd* Schale verursacht wird. Des Weiteren hilft der Ansteig der Protonenamplitude den Anstieg der $B(E2; 2_1^+ \rightarrow 0_{g.s.}^+)$ Quadrupolestärke für das neutronenreiche Isotop ^{20}C zu verstehen.

Die Methodik der Datenanalyse wird in dieser Arbeit ausführlich beschrieben. Die Identifikation der einkommenden und ausgehenden Teilchen wird ebenso diskutiert, wie auch verschiedene Addback-Algorithmen zur Rekonstruktion der Energie der γ-Strahlung. Die Anzahl der gemessenen Ereignisse sowie Triggerprobleme werden als Hauptursache für die experimentellen Unsicherheiten identifiziert. Die γ-Spektren werden mit Simulationen verglichen. Die Simulationen wurden mit R3BRoot durchgeführt, einem Softwarepaket, das das GEANT Toolkit nutzt und auf die Beschreibung von Experimenten mit dem R^3B Aufbau spezialisiert ist. In diesem Zusammenhang wird auch die Detektionseffizienz des Detektors Crystal Ball für γ-Strahlung und Protonen diskutiert.

Zusätzlich wurden zwei Prototypen für positionssensitive Siliziumdetektoren am KVI-CART getestet, die im neuen R^3B Aufbau als Trackingdetektoren genutzt werden sollen. Ihr Verhalten, wie z.B. ihre Energie- und Positionsauflösung, wird in Abhängigkeit der Integrationszeit der elektrischen Auslese untersucht. Während die beste Energieauflösung für lange Integrationszeiten erreicht wird, verbessert sich die Positionsauflösung für kurze Integrationszeiten. Die Ergebnisse werden in Bezug auf das Rauschen, das durch die resistive Oberfläche der Detektoren verursacht wird, und der daraus resultierenden Pulsformen diskutiert.

Contents

1 Introduction

Nuclear physicists try to understand the way the atomic nucleus is built from neutrons and protons. While the first macroscopic descriptions, like the liquid drop model and the semi-empirical mass formula, were able to describe the general behavior of the stable nuclei known at that time, a more sophisticated model was necessary to describe, e.g., the so-called magic numbers. Describing the nucleus with a mean potential acting on the single nucleons, neither a harmonic oscillator nor a square well potential could reproduce these observed shell closures for $Z > 20$ and $N > 20$. In 1949, Maria Goeppert Mayer [May49] and Haxel et al. [HJS49] introduced an additional term to the potential: the spin-orbit coupling. With this term, the levels split according to their total angular momentum $j = l \pm 1/2$. Due to the lower energy of the $j = l + 1/2$ orbit in comparison to the $j = l - 1/2$ orbit, the levels of the principal quantum numbers mix. Large gaps appear between the first level and the rest of the levels of a given principal quantum number, which are consistent with the experimental magic numbers. This breakthrough in the theoretical description of the atomic nucleus was awarded a Nobel Prize in Physics to Wigner, Jensen and Goeppert Mayer in 1963.

Since then, the experimental techniques as well as the computing power developed significantly. On one hand, the production of radioactive ion beams made it possible to exceed the systematic analysis to rare isotopes up to the neutron and proton dripline. On the other hand, the valence space that can be included in shell model calculations has increased significantly. However, this progress revealed some unexpected behavior in nuclei far away from the valley of stability. A broad overview over the experimental progress and the evolution of shell structure is given in [GG08, SP08]. A few dedicated examples are highlighted here. One is the discovery of neutron skins [THK$^+$92, SGB$^+$95] and neutron halos [THH$^+$85] in neutron-rich nuclei. In both cases, matter and neutron Root-Mean-Square (r.m.s.) radii were extracted from interaction cross sections from Glauber model calculations. A comparison with charge r.m.s. radii from isotope shift measurements [HTB$^+$78] for neutron-rich sodium isotopes showed a gradual growth of a neutron skin – defined as the difference of neutron and proton r.m.s. radius – with increasing neutron number. The formation of a neutron skin follows the expectation that a larger difference of the separation energies of protons and neutrons leads to an increase of the distance between proton and neutron r.m.s. radii. The picture for the neutron-halo nucleus ^{11}Li is similar: Its large matter r.m.s. radius is a hint to a strong deformation of the nucleus and a long tale in the matter distribution due to the wave function of the weakly bound nucleons, respectively.

Similarly, the predictions from independent particle model calculations evolve with the number of protons and neutrons in nuclei as outlined, e.g., by Otsuka et al. [OFU$^+$01]. This evolution of the shell model for exotic nuclei leads to changes of shell gaps and different magic numbers as well as to deformations of ground states of nuclei. For a start, no shell closure at $N = 20$ was found for some neutron-rich isotopes and an inversion of orbits was observed in the same region of the nuclear chart. This well known island of inversion and its extent was predicted among others by Warburton et al. [WBB90]. One of its examples is the ^{32}Mg nucleus. Its $B(E2; 0^+_{\text{g.s.}} \rightarrow 2^+_1)$ strength indicates no shell closure at $N = 20$ between the sd and the fp shell in contrast to neighboring nuclei like ^{38}Ar and ^{36}Si. It is therefore characterized by a large

deformation of the ground state, which can be described as a $2p2h$ intruder state from the fp shell, and a spherical shape coexistent 0^+_2 state, which corresponds to $0p0h$, as measured by Coulomb excitation [MII+95] and two neutron transfer reactions [WKK+10], respectively. Another example for the shell evolution is the formation of a shell gap at $N = 28$ for ^{46}Ar as indicated by the decreasing $B(E2; 0^+_{\text{g.s.}} \rightarrow 2^+_1)$ strength from intermediate energy Coulomb excitation cross sections [SGB+96]. On the other hand, the neighboring nuclei ^{38}S, ^{40}S, and ^{42}S exhibit deformation near $N = 28$ characteristic for mid-shell regions. The last example is the light ^{12}Be nucleus for which the shell gap at $N = 8$ vanishes. A degeneracy of the $1p_{1/2}$ and $2s_{1/2}$ orbits could be found in both inelastic scattering reactions on lead and carbon targets [IMA+00] and ^{12}Be(^{9}Be,Xγ)^{11}Be knockout reactions [NAA+00]. Furthermore, a mixed ground state configuration was found due to this degeneracy.

These examples are only a short outlook to the huge amount of experimental and theoretical work done in the field of nuclear physics.

1.1 Neutron-Rich Carbon Isotopes

The interest of this work lies on the neutron-rich side of the carbon isotopic chain. With six protons and up to 16 neutrons at the neutron dripline, the carbon isotopes are a good testing ground for nuclear theories with a variety of unexpected experimental results. As an example, an enormously hindered magnetic dipole ($M1$) transition strength of the $1/2^+$ excited state in ^{17}C [SIO+08] makes the inclusion of three-body forces and states in the continuum necessary [SIN+15]. Furthermore, the disappearance of the $N = 14$ shell gap in comparison to the neutron-rich oxygen isotopes [SSS+08] and the formation of a $Z = 6$ shell gap in ^{14}C [MW75] makes the neutron-rich carbon isotope an interesting area for shell model calculations. Additionally, ^{19}C [OBC+01, KNT+12] and ^{22}C [TYS+10, KNT+12] were found to have one-neutron and two-neutron halo structure, respectively. Furthermore, the discussion about unexpected low $B(E2; 2^+_1 \rightarrow 0^+_{\text{g.s.}})$ values for the even-even isotopes called for new theoretical descriptions of the nucleus, as will be discussed later in this chapter. Therefore, my work focuses on the even-even isotopes ^{16}C, ^{18}C, and ^{20}C.

In Figure 1.1 the occupation of the shells in an independent particle model picture is depicted for these nuclei. The protons fill the $1s_{1/2}$ and the $1p_{3/2}$ orbit. The large gap between the $1p_{3/2}$ and $1p_{1/2}$ orbit prevents protons from being located in the $1p_{1/2}$ orbit. This is indicated by the decreasing spectroscopic factors for protons in the $1p_{1/2}$ orbit from ^{12}C to ^{14}C measured with charge exchange reactions by Mairle and Wagner [MW75]. For the neutrons, the $1s_{1/2}$, $1p_{3/2}$, and $1p_{1/2}$ orbit are completely filled. The additional neutrons are located in a degenerate sd shell. The $1d_{5/2}$ and the $2s_{1/2}$ neutron single particle energies experience a degeneracy for neutron-rich carbon isotopes in contrast to the neutron-rich oxygen isotopes with a large energy difference between these two orbits, as described, e.g., by Stanoiu et al. [SSS+08]. As a result, the oxygen isotopes display a shell gap for $N = 14$ [SAD+04], while the carbon isotopes show no sign of a (sub)shell closure. This difference in the behavior of the single particle energies can be explained by a reduction of the proton-neutron tensor force and the neutron-neutron interaction in comparison to the oxygen isotopes. Therefore, in neutron-rich carbon isotopes the pairing gap with $\Delta \approx 3\,\text{MeV}$ dominates over the single-particle spacing of $\Delta E \approx 1.5\,\text{MeV}$.

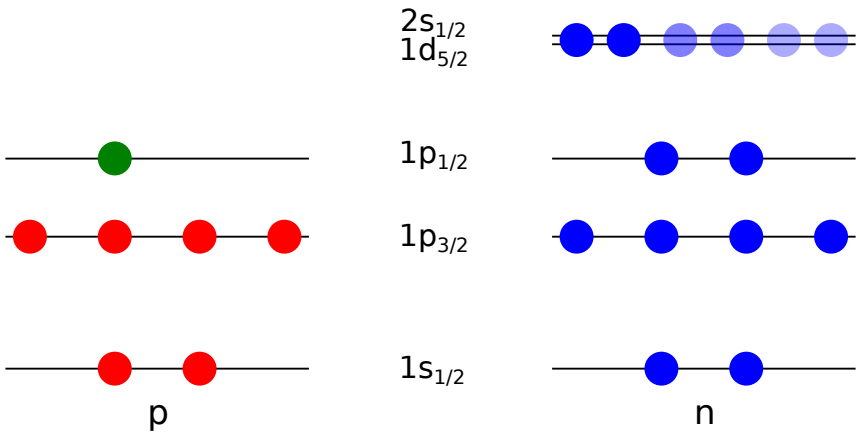

Figure 1.1: Shell structure in the independent particle model for neutron-rich carbon isotopes. The occupation number of the carbon isotopes ^{16}C, ^{18}C, and ^{20}C are indicated with red circles for protons and blue circles for neutrons. The neutrons in the degenerate *sd* shell are displayed with different brightness to indicate the different neutron numbers of $N=10$, $N=12$, and $N=14$ for ^{16}C, ^{18}C, and ^{20}C, respectively. The additional proton in the nitrogen isotopes ^{17}N, ^{19}N, and ^{21}N, from which the knockout reactions take place, is shown in green.

Several theory predictions [HS06, HS07, FMO$^+$07] as well as additional measurements support the degeneracy of the *sd* shell for neutron-rich carbon isotopes. Wuosmaa et al. [WBB$^+$10], e.g, investigate the neutron-transfer reaction ^{15}C(d,p)^{16}C and calculate relative spectroscopic factors for the measured excited states in comparison to Distorted Wave Born Approximation (DWBA) calculations. Shell model calculations which reproduce these spectroscopic factors exhibit a strong mixing of the $1d_{5/2}$ and the $2s_{1/2}$ orbit. Additionally, the analysis of the $3/2^+$ state in ^{19}C by Whitmore et al. [WSI$^+$15] shows a strongly hindered $B(M1)$ strength. The authors conclude that the *sd* degeneracy suppresses the $M1$ transitions since shell model calculations limited to this model space let the $B(M1)$ strength vanish completely. Furthermore, the lowering of the $2s_{1/2}$ state leads to the formation of a neutron halo not only for the ground state but also for the analyzed first excited state. Finally, the halo structure of the ground state of ^{19}C [OBC$^+$01, KNT$^+$12] and ^{22}C [TYS$^+$10, KNT$^+$12] can be attributed to the occupation of the $2s_{1/2}$ orbit by neutrons.

As mentioned above the development of the quadrupole transition strength $B(E2)$ of the first excited 2^+_1 state was under discussion in recent years. Since the first excited state of even-even nuclei is usually a 2^+ state, it decays via electrical quadrupole radiation to the $0^+_{\text{g.s.}}$ ground state. Therefore, this transition is a measure for the structure of nuclei – like shell closure and deformation – over a wide range of the nuclear chart. A minimum in $B(E2;2^+_1 \rightarrow 0^+_{\text{g.s.}})$ is a signature of a shell closure together with a large excitation energy $E(2^+_1)$. Also, the $B(E2)$ value is sensitive to the decoupling of protons and neutrons and can be affected by small changes in the nucleon wave functions. It is linked to the expectation value of the reduced **E2** matrix element and in general given as

$$B(E2;J_i \rightarrow J_f) = \frac{1}{2J_i+1}\langle \psi_f || \mathbf{E2} || \psi_i \rangle^2 \tag{1.1}$$

with $|\psi_i\rangle$ and $\left|\psi_f\right\rangle$ the wave functions of the initial and final state and J_i and J_f the angular momenta of these states.

In the shell model picture the $B(E2)$ strength can be calculated by taking into account the effective charges e_p and e_n of the proton and neutron, respectively. Effective charges are effective operators introduced to compensate for the truncation of the model space necessary to perform the shell model calculations of electric quadrupole observables. This effect can be described by virtual excitation of particles from the closed shell – i.e., the assumed inert core – to higher shells with a change of the major quantum number $N = 2(n-1)+l$ of $\Delta N = 2$. It is stronger for a larger overlap of the radial wave function of the valence nucleon(s) with the core and is often called core polarization. An introduction to effective charges is given by Amos de-Shalit [dS59], while a broader overview using Woods-Saxon wave functions and both microscopic and macroscopic models is given by Brown et al. [BAM77]. Using appropriate effective charges for the isotope of interest the $B(E2)$ value can then be calculated by

$$B(E2; J_i \rightarrow J_f) = \frac{\left|M_\mathrm{p} e_\mathrm{p} + M_\mathrm{n} e_\mathrm{n}\right|^2}{2J_i + 1} \tag{1.2}$$

with M_p and M_n the shell model quadrupole matrix elements of the proton and neutron. With this the connection between the decoupling of the protons and neutrons in the nucleus and a quenched $B(E2)$ strength can be explained. If the low lying 2_1^+ state is dominated by neutron excitation – as it is the case for the neutron-rich carbon isotopes – the core polarization becomes smaller, when the neutrons are less bound, i.e., the wave function is more spread out. Therefore, the effective charge of the neutron as well as the quadrupole transition strength decreases.

In recent years, several measurements of the $B(E2; 2_1^+ \rightarrow 0_{\mathrm{g.s.}}^+)$ strength for neutron-rich, even-even carbon isotopes were conducted. In principle, an increase of the quadrupole transition strength between $N = 8$ and $N = 10$ was expected since the $B(E2; 2_1^+ \rightarrow 0_{\mathrm{g.s.}}^+)$ is usually inverse proportional to the excitation energy $E(2_1^+)$ of the first excited state [RNB88], which is $E(2_1^+) = 7.012(4)\,\mathrm{MeV}$ for ^{14}C [AS91] and $E(2_1^+) \approx 1.65\,\mathrm{MeV}$ for ^{16}C, ^{18}C, and ^{20}C [PFM$^+$11, VBB$^+$12, PPC$^+$12]. However, the very first measurement via the Recoil Shadow Method (RSM) [GKS$^+$01] by Imai et al. [IOA$^+$04] reported a strongly suppressed quadrupole transition strength for ^{16}C. Although a re-evaluation of this indirect measurement together with additional measurements for ^{16}C and ^{18}C by Ong et al. [OIS$^+$08] corrected this value, the $B(E2)$ values stay nearly constant at the value of the magic nucleus ^{14}C up to $N = 12$. Direct measurements via the Recoil Distance Method (RDM) [CAB$^+$06, AEM$^+$09] for ^{16}C [WFM$^+$08, PPC$^+$12] and ^{18}C [VBB$^+$12] confirmed this trend. Only the $N = 14$ isotope ^{20}C shows an increase in $B(E2)$ as was measured by Petri et al. [PFM$^+$11] again with the RDM. All these results are summarized in Figure 1.2.

These experimental findings stimulated a wide range of theoretical studies within different frameworks, like shell model, molecular dynamics, or mean field calculations. The shell model calculations range from classic shell model to No Core Shell Model (NCSM) calculations. To give an overview over the broad range of theory predictions, a few calculations are presented in the following.

Petri et al. [PFM$^+$11, PPC$^+$12] describe shell model calculations in the p shell model space for protons and the sd shell model space for neutrons. The $B(E2; 2_1^+ \rightarrow 0_{\mathrm{g.s.}}^+)$ strength as well as the level scheme is calculated for ^{16}C, ^{18}C, and ^{20}C with the OXBASH shell model code with three different two-body nucleon-nucleon effective interactions, namely WBP [WB92], WBT

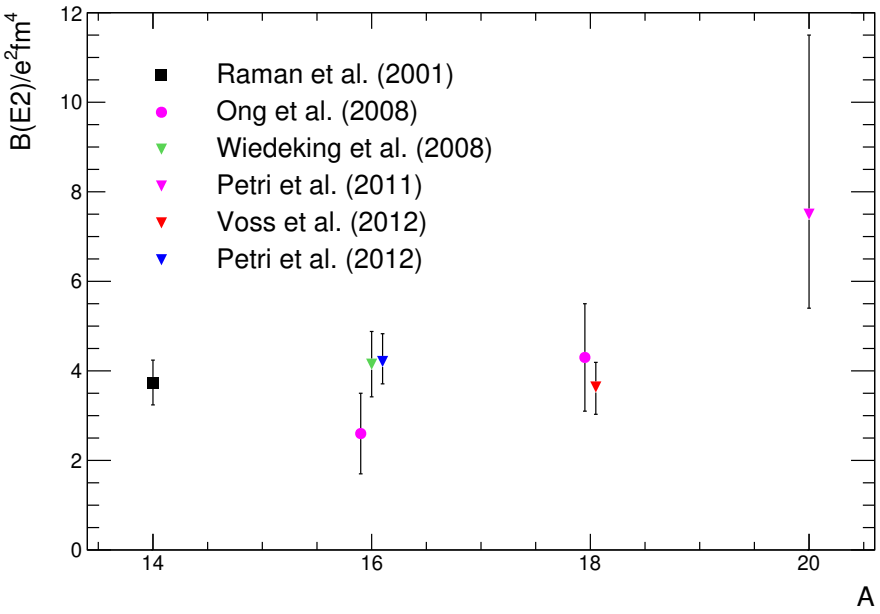

Figure 1.2: Summary of measured quadrupole transition rates from the first excited 2^+_1 state to the $0^+_{\text{g.s.}}$ ground state for neutron-rich, even-even carbon isotopes. The $B(E2;2^+_1 \rightarrow 0^+_{\text{g.s.}})$ values are taken from [RNJT01] for ^{14}C, [OIS$^+$08, WFM$^+$08, PPC$^+$12] for ^{16}C, [OIS$^+$08, VBB$^+$12] for ^{18}C, and [PFM$^+$11] for ^{20}C.

[WB92], and WBT* [SSS$^+$08]. In this approach the $B(E2)$ values can be nicely reproduced using Equation 1.2 together with effective charges following an $\propto 1/A$ dependency. This dependency of the core polarization is explained by Bohr and Mottelson [BM69, BM75] with the analogous dependency of the eccentricity of the density distribution and the nonspherical potential of the valence nucleons, respectively. With this, the increase in $B(E2)$ strength for ^{20}C is attributed to an increase in the proton matrix element M_{p}, while the majority of the transition strength for ^{16}C and ^{18}C stems from the neutron matrix element M_{n}.

Another microscopic shell model calculation by Fujii et al. [FMO$^+$07] uses the whole $0s0p1s0d1p0f$ shell without any core. The CD-Bonn potential [MSS96] together with the Coulomb interaction is used to calculate the $B(E2;2^+_1 \rightarrow 0^+_{\text{g.s.}})$ strength for ^{14}C, ^{16}C, and ^{18}C. Originally, the authors use bare charges, which implies that the $B(E2)$ strength includes no neutron contribution. However, with bare charges only very small $B(E2)$ values – compatible with the original analysis by Imai et al. [IOA$^+$04] – can be reproduced, while a reasonable transition strength can only be achieved with small effective charges.

The first large scale ab-initio NCSM for such heavy, neutron-rich carbon isotopes are reported by Forssén et al. [FRN13]. The authors compare calculations with four different interactions, including the pure nucleon-nucleon interaction CDB2k [Mac01], the INOY interaction [Dol04] including some effects of three-nucleon forces, a chiral N^{3}LO two-body interaction [EM03], and a local chiral N^{2}LO three-nucleon interaction [GQN09]. Since a full convergence of the calculation is not (yet) possible, the results of the finite model space are extrapolated to infinite model space. Additionally, some calculations are done with the Importance Truncated NCSM (IT-NCSM) approach to reduce the model space to a manageable size. In these calculations, no effective charges need to be included since no core is assumed. The comparison with experimental data, as, e.g., in [VBB$^+$12, PPC$^+$12], shows a good reproduction of the $B(E2;2^+_1 \rightarrow 0^+_{\text{g.s.}})$ strength.

Again, the results indicate a neutron-dominant nature of the first excited 2_1^+ state. However, it seems that three-body forces need to be included to reproduce the experimental branching ratios for ^{16}C.

Additionally, several authors use shell model calculations as the basis of their analysis. Ma et al. [MDY10], e.g., calculate the polarization effect for protons and neutrons explicitly with the particle-vibration approach. Their calculation of the $B(E2; 2_1^+ \rightarrow 0_{g.s.}^+)$ strength using microscopic polarization effects together with Hartree-Fock (HF) wave functions results in an overall good reproduction of the experimental data.

Furthermore, Antisymmetrized Molecular Dynamics (AMD) calculations [KE05, KEKS13] explain the small $B(E2; 2_1^+ \rightarrow 0_{g.s.}^+)$ strength with the deformation of neutron-rich carbon isotopes. Yoshiko Kanada-En'yo [KE05] uses the MV1 central potential including three-nucleon forces [AITS80] together with the G3RS description of the spin-orbit potential [YKNA79] and the Coulomb potential to extract an oblate deformation of the proton distribution and a prolate deformation of the neutron distribution with perpendicular symmetry axes for ^{16}C. Since the first excited 2_1^+ state can be portrayed as a collective rotation, the small quadrupole transition strength is explained by a reduced proton contribution due to the alignment of the rotational axis and the symmetry axis of the proton distribution. Thus, the $B(E2)$ strength is dominated by the neutrons. On the other hand, ^{20}C displays an oblate deformation for both the proton and neutron distribution. Thus, their symmetry axes and the rotational axis align and the $B(E2)$ strength increases for $N = 14$.

On the other hand, Yao et al. [YMR$^+$11] describe the axial and triaxial deformation of even-even carbon isotopes with the Relativistic Mean Field (RMF) approach. The authors use the Angular Momentum Projection (AMP) method to restore the broken rotational symmetry and the Generator Coordinate Method (GCM) to include configuration mixing of states with different triaxial shapes. The RMF + Bardeen-Cooper-Schriefer (BCS) calculations are done using the PC-F1 energy functional [BMMR02], which is fitted to properties of nuclear matter and ground state observables of spherical nuclei. The investigation of the axial deformation shows two minima in the potential energy curves of ^{16}C, ^{18}C, and ^{20}C, which correspond to a prolate and an oblate deformation and whose energy difference is small. The analysis of the triaxial deformation indicates a larger deformation for the neutrons than for the protons in all three isotopes. In addition, the deformation of the protons and neutrons is decoupled. This effect is stronger in ^{16}C than in ^{20}C. Furthermore, all three isotopes show large fluctuations in the γ deformation, as indicated by the two minima in the calculation of the axial deformation. The shape evolution from a prolate deformation in ^{16}C to an oblate deformation in ^{20}C is clearly visible from the calculation. The experimental values for the energy of the first excited 2_1^+ state and the $B(E2)$ strength are reproduced rather well, with the stretching of the calculated spectrum being caused by the use of Projection After Variation (PAV). The comparison of the axial and triaxial calculations shows no significant difference in these values, since even in the triaxial calculation the deformation is mainly axial symmetric.

Finally, the simple picture of two shell model states mixing is used for the interpretation of the experimental results [WFM$^+$08, MPF$^+$14]. The first of the two mixing states is motivated by the first excited 2_1^+ state of ^{18}O, which is interpreted as an excitation of the two neutrons outside the ^{16}O core. The second one corresponds to the first excited 2_1^+ state of ^{14}C, which is interpreted as a proton excitation of the $2h$ ground state. Thus, the first excited 2_1^+ states in ^{16}C, ^{18}C, and ^{20}C are seen as a superposition of a pure proton excitation and a pure neutron excitation, as illustrated in Figure 1.3. The increase in $B(E2; 2_1^+ \rightarrow 0_{g.s.}^+)$ strength for $N = 14$ is then explained

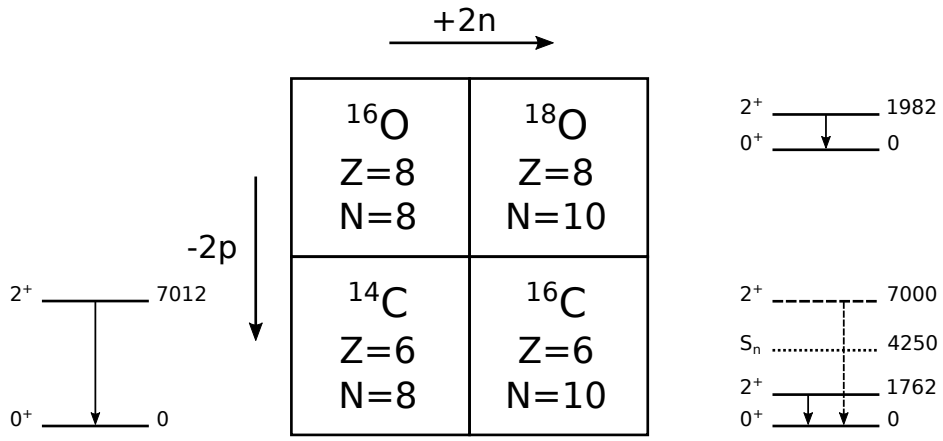

Figure 1.3: Sketch of two state mixing for ^{16}C. The first 2^+_1 state in ^{18}O with an energy of 1.982(1) MeV [AS87] is interpreted as an excitation of the two neutrons outside the ^{16}O core, while the one in ^{14}C with an energy of 7.012(4) MeV [AS91] is interpreted as a proton excitation of the *2h* ground state. The mixing of these two states in ^{16}C leads to a first excited 2^+_1 state, which can be found at an energy of 1.762(2) MeV [PPC$^+$12]. An additional mixed symmetry state is expected with an energy of $\approx$ 7 MeV. This state would lie well above the neutron separation energy of $S_n = 4.250$ MeV [WAW$^+$12] and is therefore expected to be unbound. The sketch is based on [WFM$^+$08].

by an increase of the proton contribution due to a reduction of the gap between the proton $1p_{3/2}$ and $1p_{1/2}$ orbit as described by Otsuka et al. [OSF$^+$05]. This approach is the basis of the concept of the proton amplitude and discussed in more detail in Section 2.2 and 2.3.

To investigate the first excited 2^+_1 state of these neutron-rich, even-even carbon isotopes in the light of a two-state mixing model, knockout and Quasi-Free Scattering (QFS) reactions from neutron-rich nitrogen isotopes are analyzed in this work. The experiment was performed at GSI Helmholtzzentrum für Schwerionenforschung GmbH (GSI) with the Reactions with Relativistic Radioactive Beams (R^{3}B)/Large Area Neutron Detector (LAND) setup, taking advantage of the possibility to perform kinematically complete measurements with heavy ion beams in inverse kinematics.

In Chapter 2, the two different reaction mechanisms and the way they are described in Glauber theory are introduced. Additionally, the idea of two-state mixing and its applications in terms of the proton amplitude are discussed. Furthermore, a short overview over previous measurements is given. Chapter 3 introduces the experimental setup, the detectors used and the Data Acquisition (DAQ) with which the data were recorded. In Chapter 4, the analysis framework as well as the major analysis steps are outlined. This includes the identification of the incoming and outgoing ions as well as the detection of the emitted γ rays and potential protons from the QFS reactions. Additionally, different fit algorithms are introduced with which simulated and measured data are compared. In Chapter 5 the simulation framework is introduced. The simulation to determine the efficiency of the γ-ray detection is introduced and verified. A second set of simulations determines the efficiency for proton detection and generates γ-ray spectra which are afterwards compared with experimental spectra to determine the contribution from the different excited states. Finally, the results of the whole analysis are presented and discussed

in Chapter 6. Inclusive and exclusive cross sections are calculated for knockout and QFS reactions and compared with theoretical predictions from the Glauber model. The proton amplitude is determined for ^{16}C, ^{18}C, and ^{20}C.

In addition to the study of neutron-rich carbon isotopes, a new silicon strip prototype detector for simultaneous energy and position measurement was tested. The detector, called Micron X5, will be used in future versions of the R^{3}B setup. Its working principle as well as the developed algorithms to calibrate the detector are presented in Chapter 7. Data from a test beam time at KVI-Center for Advanced Radiation Technology (KVI-CART) are analyzed to determine the best settings for the electronic readout and the overall performance of the detector.

2 Theory

This chapter introduces the theory which is employed in this thesis. The first part describes the reaction theory used to calculate cross sections for knockout and QFS reactions. The second part describes the concept of configuration mixing using states of the independent particle or shell model. Additionally, it introduces one of its implications: the proton amplitude in neutron-rich, even-even carbon isotopes. The chapter ends with an overview over previous measurements of the excited states and the proton amplitude.

2.1 Reaction Theory

Cross sections are a major tool in nuclear physics to examine the structure of the nucleus. With the comparison of experimental and theoretical cross sections, one can verify the models on which the calculations are based. This includes both the reaction mechanism and the model describing the nucleus itself. Choosing a reaction mechanism, the probability for a reaction with a nucleon in a certain single particle state nlj is calculated. On one hand, the resulting single particle cross section $\sigma_{\mathrm{sp}}(nlj)$ can then be used to calculate the total cross section taking into account all possible single particle states

$$\sigma_{\mathrm{theo}} = \sum_{nlj} C^2 S_{nlj} \sigma_{\mathrm{sp}}(nlj). \tag{2.1}$$

In this case, C^2S_{nlj} is the theoretical spectroscopic factor for a given state nlj in the isospin representation, with C^2 being the square of the isospin coupling coefficient. If wave functions normalized to unity are used, the spectroscopic factors are linked to the occupancy of the orbits: $C^2S_{nlj} = 1$ for a pure single particle state nlj and $C^2S_{nlj} = 2j+1$ for a filled orbit with total angular momentum j. Furthermore, for more elaborate models the theoretical spectroscopic factor can be calculated via the reduced matrix element of the creation operator $\mathbf{a}^+$ as described by Alex Brown [Bro11] as

$$S = \frac{\left|\langle \psi^A \,||\, \mathbf{a}^+ \,||\, \psi^{A-1}\rangle\right|^2}{2J+1} \tag{2.2}$$

with the wave functions $\left|\psi^A\right\rangle$ and $\left|\psi^{A-1}\right\rangle$ of the incoming and outgoing nuclei with the masses A and $A-1$, respectively, and the angular momentum J of the heavier nucleus. On the other hand, the single particle cross section $\sigma_{\mathrm{sp}}(nlj)$ can be compared to experimental, exclusive cross sections σ_{exp} for a given excited state. This way the occupation number of a certain orbit in the state of interest can be determined by calculating the experimental spectroscopic factor

$$S_{\mathrm{exp}} = \frac{\sigma_{\mathrm{exp}}}{\sigma_{\mathrm{sp}}(nlj)}. \tag{2.3}$$

To calculate the relevant reaction cross sections the Glauber theory of nuclear scattering is used. It is based on several assumptions. First of all, the energy of the incoming particles and the reaction, respectively, needs to be several hundred MeV. In this region, the nucleon-nucleon cross section has a minimum as depicted and parametrized by Bertulani and De Conti in [BC10] with experimental data from the Particle Data Group [Y$^+$06]. Therefore, the probability for a second reaction of the scattering partners in the nucleus is small. With this, the assumption of the Distorted Wave Impulse Approximation (DWIA) of a single interaction between the target and the nucleon is reasonable for a thin target. Absorption and scattering along the way are described by an optical potential and incorporated in the distorted wave description of the particles. The general form of the optical potential is $U_{\text{opt}}(\mathbf{r}) = V(\mathbf{r}) + \mathrm{i}W(\mathbf{r})$ with the real potential $V(\mathbf{r})$ describing the elastic scattering as well as nuclear reactions and the imaginary part $W(\mathbf{r})$ responsible for the absorption as described in [Kra88]. In addition, the Glauber framework uses the eikonal approximation. In the eikonal picture the incoming and outgoing particles are following a straight line through the medium. This picture is most valid for high-energy particles scattered in forward direction. Finally, with the so-called sudden or adiabatic approximation it is assumed that the internal motion of the nucleus is frozen on the time scale of the interaction. This is true, when the kinetic energy E of the system is large in comparison to the potential depth V.

The use of the eikonal wave function is described, e.g., in [BD04, ABR13]. It is written as

$$\psi_k^{+/-}(\mathbf{r}) = e^{\mathrm{i}\mathbf{k}\cdot\mathbf{r}}\, S^{+/-}(b) \tag{2.4}$$

for incoming (+) and outgoing (−) particles. Hereby, b is the absolute value of the transverse component of the coordinate $\mathbf{r} = (z, \mathbf{b})$. It is often interpreted as the classical impact parameter but since it is associated with the quantum mechanical state $\psi_k^{+/-}(\mathbf{r})$, effects like smearing and interference are included in this ansatz. The scattering matrix $S^{+/-}(b)$ describes the scattering of the incoming and outgoing wave function. It can also be called survival amplitude since it is a measurement of the distortion and absorption of the incoming and outgoing particles. In the eikonal approximation it is written as

$$S^{+/-}(b) = \exp\left[\mathrm{i}\chi^{+/-}(b)\right]. \tag{2.5}$$

$\chi^{+/-}(b)$ is called the eikonal phase and is in general given by

$$\chi^{+/-}(b) = -\frac{1}{\hbar v} \int_{a(+/-)}^{c(+/-)} \mathrm{d}z\; U_{\text{opt}}^{+/-}(\mathbf{r}) \tag{2.6}$$

with the relative velocity v and the optical potential $U_{\text{opt}}(\mathbf{r})$ that describes the core+target or nucleon+target scattering. The limits $a(+/-)$ and $c(+/-)$ depend on the reaction mechanism and whether an incoming (+) or outgoing (−) particle is described. For knockout and QFS reactions they are given in the corresponding sections below.

As mentioned before, the optical potential "accounts [...] for elastic scattering in the presence of absorptive effects" [Kra88]. It can be described, e.g., by the sum of a nuclear potential and the Coulomb potential. However, this general expression leads to problems with the convergence of

the Coulomb potential when calculating the eikonal phase. To avoid this, the eikonal phase can be expressed for the nuclear and the Coulomb part of the interaction potential separately

$$\chi(b) = \chi_{\mathrm{N}}(b) + \chi_{\mathrm{C}}(b). \tag{2.7}$$

The Coulomb part is usually [BD04, BH04] given by

$$\chi_{\mathrm{C}}(b) = 2\eta \, \ln(kb) \tag{2.8}$$

with $\eta = Z_{\mathrm{p}} Z_{\mathrm{t}} e^2/\hbar v$, the charge Z_i of the projectile p and target t, and their wave number k in the center of mass system. Since the nuclear charge is not point like but extended, one needs to account for this distribution. For light nuclei, for which a Gaussian distribution of the nuclear densities can be assumed, the eikonal phase is modified to

$$\chi_{\mathrm{C}}(b) = 2\eta \left[\ln(kb) + \frac{1}{2} E_1\left(\frac{b^2}{R^2}\right) \right] \tag{2.9}$$

with $R = \sqrt{R_{\mathrm{p}}^2 + R_{\mathrm{t}}^2}$, R_{p} and R_{t} being the radius of the projectile and target, and the error function

$$E_1(x) = \int_x^\infty \frac{\mathrm{e}^{-t}}{t} \mathrm{d}t. \tag{2.10}$$

Finally, the Coulomb scattering amplitude is independent of the eikonal approximation and given by

$$f_{\mathrm{C}}(\theta) = \frac{Z_{\mathrm{p}} Z_{\mathrm{t}} e^2}{2\mu v^2 \sin^2(\theta/2)} \, \exp\left\{ -\mathrm{i}\eta \ln[\sin^2(\theta/2)] + \mathrm{i}\pi + 2\mathrm{i}\phi_0 \right\} \tag{2.11}$$

with $\phi_0 = \arg\Gamma(1 + \mathrm{i}\eta/2)$.

For the nuclear eikonal phase, on the other hand, an optical potential is used to describe the interaction between the involved particles. The simplest version is the $t\rho$ or $t\rho\rho$ approach which neglects spin-orbit and surface terms. For a nucleon-nucleus collision the optical potential is given by

$$U_{\mathrm{opt}}(\mathbf{r}) = t_{\mathrm{Nn}} \, \rho_{\mathrm{n}}(\mathbf{r}) + t_{\mathrm{Np}} \, \rho_{\mathrm{p}}(\mathbf{r}) \tag{2.12}$$

with ρ_{p} and ρ_{n} the proton and neutron ground-state densities and $t_{\mathrm{N}i}$ the transition matrix elements for nucleon-nucleon scattering in forward direction. The transition matrix elements can be described as

$$t_{\mathrm{N}i}(\mathbf{q} = 0) = -\frac{2\pi\hbar^2}{\mu} f_{\mathrm{N}i}(\mathbf{q} = 0) = -\frac{\hbar v}{2} \sigma_{\mathrm{N}i}(\alpha_{\mathrm{N}i} + \mathrm{i}) \tag{2.13}$$

with the free nucleon-nucleon cross section $\sigma_{\mathrm{N}i}$, the ratio of the imaginary and real part of the scattering amplitude $\alpha_{\mathrm{N}i}$ and the momentum transfer $\mathbf{q} = \mathbf{k} - \mathbf{k}' = 0$.

For nucleus-nucleus collisions this approach can then be extended to the potential

$$U_{\mathrm{opt}}(\mathbf{r}) = \int \langle t_{\mathrm{NN}}(\mathbf{q}=0)\rangle \; \rho_{\mathrm{p}}(\mathbf{r}-\mathbf{r}') \; \rho_{\mathrm{t}}(\mathbf{r}') \; \mathrm{d}^3 r' \tag{2.14}$$

with ρ_{p} and ρ_{t} the density of the projectile p and target t, respectively. $\langle t_{\mathrm{NN}}\rangle$ is the isospin average of the transition matrix elements in Equation 2.13. It can be parametrized using the nucleon-nucleon scattering amplitude introduced by [Ray79]

$$f_{\mathrm{NN}}(\mathbf{q}) = \frac{k_{\mathrm{NN}}}{4\pi} \; \sigma_{\mathrm{NN}}(i+\alpha_{\mathrm{NN}}) \; \exp\left(-\beta_{\mathrm{NN}}\mathbf{q}^2\right). \tag{2.15}$$

This way the nuclear optical potential is described with a real and an imaginary part with σ_{NN}, α_{NN}, and β_{NN} being parameters fitted to high-energy nucleon-nucleon scattering data at forward angles. Finally, the nuclear part of the eikonal phase in the optical limit of the Glauber theory can be written as

$$\chi_{\mathrm{N}}(b) = \frac{1}{k_{\mathrm{NN}}} \int_0^\infty \mathrm{d}q \; q \; \tilde{\rho}_{\mathrm{p}}(q) \; \tilde{\rho}_{\mathrm{t}}(q) \; f_{\mathrm{NN}}(q) \; J_0(qb) \tag{2.16}$$

with the Fourier transformation $\tilde{\rho}_i(q)$ of the nuclear densities of projectile p and target t and the Bessel function J_0. Depending on the reaction of interest, the nuclear densities are either described by Gaussian shapes for light nuclei or by Fermi shapes for heavier nuclei. Furthermore, for a higher accuracy one can take density distributions from HF calculations as has been done for the calculation in Section 6.1.1. In principle, Equation 2.15 describes the free scattering of two nucleons independent of the surrounding nucleus, while the in-medium scattering amplitude is needed in Equation 2.16. The difference of the free and the in-medium nucleon-nucleon cross section is that the latter takes into account that the nucleon cannot scatter into occupied states. This so-called Pauli blocking can be included in the scattering amplitude as described, e.g., in [BD04, BC10].

2.1.1 Knockout Reactions

Knockout reactions are reactions in which a bound nucleus hits a target consisting of nuclei itself (in case of this thesis ^{12}C but most often ^{9}Be) and loses a nucleon in this process. Because of the composite nature of the target, this reaction type is surface dominated, i.e., it is only sensitive to the external part of the wave function of the removed nucleon.

This thesis follows the description in the eikonal and sudden approximation, described in general in the previous section and for knockout reactions in detail in [BG06, BH04, BC10]. In this picture, the incoming nucleus A consists of the nucleon of interest N and the rest of the nucleus called core c. Both interact with a target nucleus t. After the reaction, the remaining fragment B might be in an excited state. The naming convention and all involved particles are shown in Figure 2.1.

Knockout reactions include two kind of reactions. The first one is called stripping or inelastic breakup. In this case, the removed nucleon reacts with and excites the target. Usually, it is

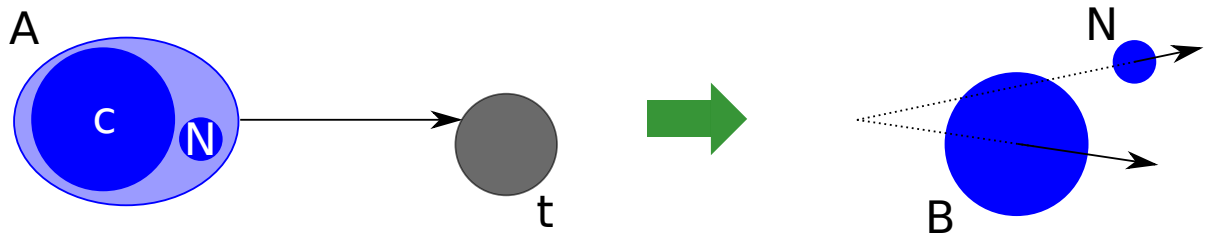

Figure 2.1: Sketch of particles involved in knockout reactions.

stuck in the target and will not be detected with the surrounding detectors (like in our case the particle and γ-ray detector Crystal Ball). With the assumption of the sudden approximation the momentum of the core after the reaction corresponds to the momentum of the nucleon before the reaction: $\mathbf{k}_\mathrm{B} = \mathbf{k}_\mathrm{N}$. Following Bertulani and De Conti [BC10], the cross section for this type of reaction can be described as the survival of the core ($|S_\mathrm{c}(b_\mathrm{c})|^2$) and the removal of the nucleon ($[1-|S_\mathrm{N}(b_\mathrm{N})|^2]$). This leads to the cross section

$$\sigma_\mathrm{str} = (C^2S)\,\frac{2\pi}{2l+1}\int_0^\infty \mathrm{d}b_\mathrm{N}\;\; b_\mathrm{N}\,[1-|S_\mathrm{N}(b_\mathrm{N})|^2]\int \mathrm{d}^3\mathbf{r}\;\,|S_\mathrm{c}(b_\mathrm{c})|^2\sum_m |\psi_{lm}(\mathbf{r})|^2. \tag{2.17}$$

The second kind of reaction is called diffractive or elastic breakup. It describes the dissociation of the nucleon from the core because of the interaction with the target. The core and the removed nucleon have a similar velocity and both can be detected in forward direction. The target stays in its ground state. The cross section for this reaction is given by

$$\begin{aligned}\sigma_\mathrm{diff} = (C^2S)\,\frac{2\pi}{2l+1}\sum_m\int_0^\infty \mathrm{d}b_\mathrm{N}\;\, b_\mathrm{N}\\ \times\left\{\int \mathrm{d}^3\mathbf{r}\,|S_\mathrm{N}(b_\mathrm{N})\,S_\mathrm{c}(b_\mathrm{c})\,\psi_{lm}(\mathbf{r})|^2 - \sum_{m'}\left|\int \mathrm{d}^3\mathbf{r}\,\psi_{lm'}(\mathbf{r})\,S_\mathrm{N}(b_\mathrm{N})\,S_\mathrm{c}(b_\mathrm{c})\,\psi_{lm}(\mathbf{r})\right|^2\right\}.\end{aligned} \tag{2.18}$$

In both cases (C^2S) is the spectroscopic factor, l the angular momentum of the knocked-out nucleon, b_N and b_c the impact parameters of the nucleon N and the core c with $b_\mathrm{c} = \sqrt{r^2\sin^2\theta + b_\mathrm{N}^2 - 2r\sin\theta\, b_\mathrm{N}\cos\phi}$, and $\psi_{lm}(\mathbf{r})$ the wave function of the incoming nucleus A. As described in more detail in [BG06], the wave function $\psi_{lm}(\mathbf{r}) = R_l(r)Y_{lm}(\mathbf{r})$ is calculated solving the radial Schrödinger equation using a potential

$$V(\mathbf{r}) = V_0(r) + V_\mathrm{ls}(r)\,\mathbf{l}\cdot\mathbf{s} + V_\mathrm{C}(r) \tag{2.19}$$

with the central potential $V_0(r)$, the spin-orbit potential $V_\mathrm{ls}(r)$, and the Coulomb potential $V_\mathrm{C}(r)$. The eikonal scattering matrices $S_i^{+/-}(b_i)$ are calculated using Equation 2.5 and 2.6 with

$a(+) = -\infty$ and $c(+) = z$ for the incoming wave function and $a(-) = z$ and $c(-) = \infty$ for the outgoing wave function. The scattering amplitude $S_i(b_i)$ is then given by

$$\langle \psi^-_{i,\mathbf{k}} | \psi^+_{i,\mathbf{k}'} \rangle = e^{\mathrm{i}\mathbf{q}\cdot\mathbf{r}}\, S_i(b_i) = e^{\mathrm{i}\mathbf{q}\cdot\mathbf{r}}\, S_i^+(b_i)\, S_i^-(b_i) \tag{2.20}$$

with $a = -\infty$, $c = \infty$ and $\mathbf{q} = \mathbf{k} - \mathbf{k}'$.

Additionally, in case of elastic scattering the scattering amplitude $f_{\mathrm{el}}(\theta)$ can be expressed in terms of the eikonal phase from Equation 2.6 with $a = -\infty$ and $c = \infty$. As described in [BD04] for reactions in forward direction ($\theta \ll 1$ and $(\mathbf{k} - \mathbf{k}') \cdot \mathbf{k} \cong 0$) the scattering amplitude is given by

$$f_{\mathrm{el}}(\theta) = \frac{\mathrm{i}k}{2\pi} \int \mathrm{d}^2 b\; \mathrm{e}^{\mathrm{i}\mathbf{q}\cdot\mathbf{b}} \{1 - \exp[\mathrm{i}\chi(b)]\} \tag{2.21}$$

with the momentum transfer $q = 2k \sin(\theta/2)$ and the scattering angle θ. With the additional assumption of a spherically symmetric potential, the scattering amplitude can be simplified to

$$f_{\mathrm{el}}(\theta) = \mathrm{i}k \int \mathrm{d}b\; b\, J_0(qb) \{1 - \exp[\mathrm{i}\chi(b)]\} \tag{2.22}$$

depending only on the eikonal phase $\chi(b)$ and the Bessel function $J_0(qb)$. Separating the eikonal phase from the Coulomb interaction as described in the previous section, the scattering amplitude can then be written as

$$f_{\mathrm{el}}(\theta) = f_{\mathrm{C}}(\theta) + \mathrm{i}k \int_0^\infty \mathrm{d}b\; b\, J_0(qb)\; \exp[\mathrm{i}\chi_{\mathrm{C}}(b)]\; \{1 - \exp[\mathrm{i}\chi_{\mathrm{N}}(b)]\}. \tag{2.23}$$

The Coulomb phase $\chi_{\mathrm{C}}(b)$ and scattering amplitude $f_{\mathrm{C}}(\theta)$ are given by Equation 2.9 and 2.11, respectively.

2.1.2 QFS Reactions

Traditionally, in QFS reactions a proton beam hits a target consisting of the particles of interest and scatters on a single nucleon in the nucleus. Therefore, these reactions are also referred to as (p,2p) or (p,pn) reactions depending on the type of the removed nucleon. However, nowadays most of the particles of interest have a too short lifetime to make a target out of them. Thus, the reactions are investigated in inverse kinematics in which a beam of radioactive ions hits a proton target.

The reaction can be seen as a proton scattering on a nucleon without any interaction with the rest of the nucleus. Thus, it is possible to study strongly bound nucleons and probe the inner shells, respectively. Due to momentum conservation, the momentum of the remaining nucleus matches the one of the knocked-out nucleon before the scattering: $\mathbf{k}_{\mathrm{B}} = \mathbf{k}_{\mathrm{N}}$. This way, the momentum distribution and with it the angular momentum of the nucleon can be measured by determining the momentum distribution of the fragment. However, since in my case the protons

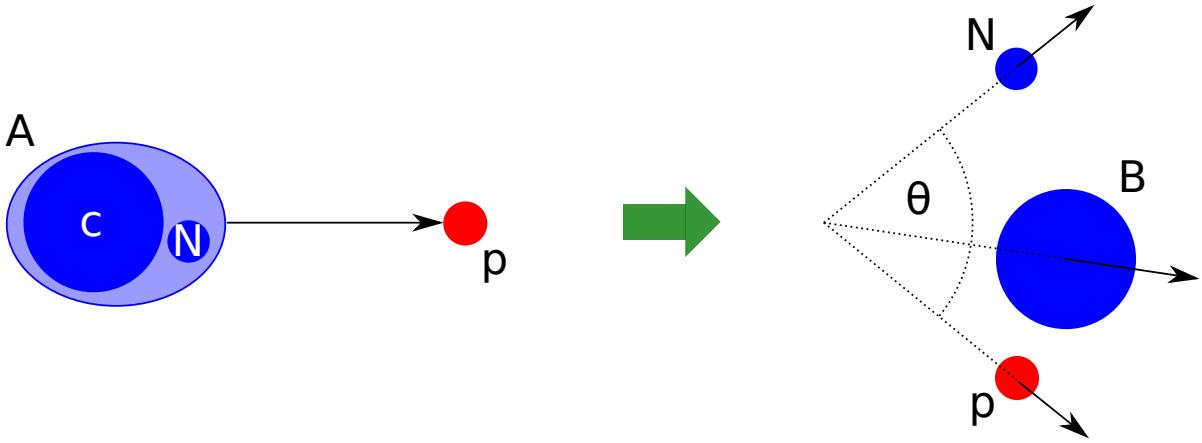

Figure 2.2: Sketch of particles involved in QFS reactions.

of interest are both located in the $1p$ shell, this method is not available to distinguish between the two orbits. Furthermore, due to the internal momentum of the nucleon, the scattering angle does not match the expectation for free scattering reactions. In addition, the relativistic energies of the incoming nuclei lead to an increased relativistic mass of one of the scattering nucleons. Therefore, the angle θ between the two outgoing nucleons depends on the energy of the incoming beam. For the carbon isotopes in the analyzed experiment the angle is $\theta \approx 80°$ in contrast to free scattering reactions for which it is 90°. On the other hand, the azimuthal angle ϕ is unaffected by this: The two nucleons are scattered back-to-back.

To calculate the cross section for QFS reactions, the DWIA is used together with the eikonal description of the wave functions. The general approach is described in the previous section, while the details for QFS reactions can be found in [ABR13]. In this description, the incoming nucleus A consists of the nucleon N and the core c, which acts as a spectator. The nucleon N scatters on the proton p in the target and is removed from the nucleus. After the reaction, the remaining fragment B might be in an excited state. The naming convention used for all involved particles are shown in Figure 2.2.

In general, the transition matrix element in the DWIA is given by

$$T_{\mathrm{p,pN}} = \sqrt{S(lj)}\ \langle \chi^{(-)}_{\mathbf{k'}_\mathrm{p}}\ \chi^{(-)}_{\mathbf{k}_\mathrm{N}} | \tau_{\mathrm{pN}} | \chi^{(+)}_{\mathbf{k}_\mathrm{p}}\ \psi_{jlm} \rangle \tag{2.24}$$

$$= \sqrt{S(lj)}\ \tau(\mathbf{k'}_{\mathrm{pN}}, \mathbf{k}_{\mathrm{pN}}; E) \int \mathrm{d}^3\mathbf{r}_{\mathrm{NB}}\ \chi^{(-)}_{\mathbf{k'}_\mathrm{p}}(\mathbf{r}_{\mathrm{NB}})\ \chi^{(-)}_{\mathbf{k}_\mathrm{N}}(\mathbf{r}_{\mathrm{NB}})\ \chi^{(+)}_{\mathbf{k}_\mathrm{p}}(\alpha\mathbf{r}_{\mathrm{NB}})\ \psi_{jlm}(\mathbf{r}_{\mathrm{NB}}) \tag{2.25}$$

with $\alpha = (A-1)/A$, $\chi^{(+/-)}_{\mathbf{k}_i}$ the distorted wave of the incoming (+) and outgoing (−) nucleons i involved in the reaction, ψ_{jlm} the bound state wave function of the knocked-out nucleon, τ_{pN} the two-body pN scattering matrix, $\tau(\mathbf{k'}_{\mathrm{pN}}, \mathbf{k}_{\mathrm{pN}}; E)$ its Fourier transformation, and $\sqrt{S(lj)}$ the spectroscopic factor.

Together with the eikonal description (Equation 2.4) for the distorted wave functions $\chi^{(+/-)}_{\mathbf{k}_i}$ the transition matrix can be simplified to

$$T^{(\mathrm{eik})}_{\mathrm{p,pN}} = \sqrt{S(lj)}\ \tau(\mathbf{k'}_{\mathrm{pN}}, \mathbf{k}_{\mathrm{pN}}; E) \int \mathrm{d}^3\mathbf{r}\ \mathrm{e}^{-\mathrm{i}\mathbf{Q}\cdot\mathbf{r}}\ S(b,\theta)\ \psi_{jlm}(\mathbf{r}) \tag{2.26}$$

with $\mathbf{Q} = \mathbf{k}'_{\mathrm{p}} + \mathbf{k}_{\mathrm{N}} - \alpha\mathbf{k}_{\mathrm{p}}$ the missing momentum, θ the angle between the two outgoing particles, and $S(b,\theta)$ the product of the survival amplitudes given by

$$S(b,\theta) = S_{\mathrm{pA}}(E_{\mathrm{p}}, b) \cdot S_{\mathrm{p'B}}(E'_{\mathrm{p}}, \theta'_{\mathrm{p}}, b) \cdot S_{\mathrm{NB}}(E_{\mathrm{N}}, \theta_{\mathrm{N}}, b). \tag{2.27}$$

The single survival amplitudes are given by Equation 2.5 and 2.6 with $a = -\infty$ and $c = b$ for incoming and $a = \infty$ and $c = b$ for outgoing nucleons. In case of QFS reactions the optical potential for the eikonal phase is given by a term describing the Coulomb interaction and a real and an imaginary part of the nucleus-nucleus interaction. The real part is given by the M3Y potential [BBML77], while the imaginary part is given explicitly in the $t\rho\rho$ approximation described in Section 2.1

$$U(\mathbf{r}) = U_{\mathrm{M3Y}}(\mathbf{r}) + U_{\mathrm{C}}(\mathbf{r}) - \mathrm{i}\frac{E}{k}\sigma_{\mathrm{N}}(E) \int \mathrm{d}^3\mathbf{r}'\ \rho_{\mathrm{A(B)}}(\mathbf{r}-\mathbf{r}')\ \rho_{\mathrm{p}}(\mathbf{r}'). \tag{2.28}$$

Similar to the knockout reactions described in the previous section, the wave function of the bound nucleon is the solution of the radial Schrödinger equation using the potential in Equation 2.19. It can be written as

$$\psi_{jlm}(\mathbf{r}) = \frac{u_{lj}(r)}{r} \sum_{m_l, m_s} \langle l m_l s m_s | j m \rangle Y_{l m_l}(\mathbf{r}) \chi_{m_s} \tag{2.29}$$

with the Clebsch-Gordan coefficients $\langle l m_l s m_s | j m \rangle$, the radial part of the wave function $u_{lj}(r)/r$, the spherical harmonics $Y_{l m_l}(\mathbf{r})$, and the spinors χ_{m_s}.

Finally, the eikonal transition matrix in Equation 2.26 is used to calculate the cross section for QFS reactions to be

$$\sigma_{\mathrm{QFS}} = S(lj)\frac{2\pi}{2j+1}\sum_m \left\langle \frac{d\sigma_{\mathrm{pN}}}{d\Omega} \right\rangle |C_{lm}|^2 \int \mathrm{d}b\ b\ |\langle S(b) \rangle|^2 \int_{-\infty}^{\infty} \mathrm{d}z\ \left| \frac{u_{lj}(r)}{r}\ P_{lm}(b,z) \right|^2 . \tag{2.30}$$

Here, P_{lm} are Legendre polynomials with $Y_{lm}(\theta, 0) = C_{lm} P_{lm}(\cos\theta)$. Both the quasifree pN cross section $d\sigma_{\mathrm{pN}}/d\Omega$ and the scattering matrix $S(b)$ are averaged over all final momenta constraint by energy and momentum conservation.

2.2 Configuration Mixing

This section introduces a way to predict realistic states in isotopes by mixing two pure states, e.g., from shell model calculations. Afterwards, one application using this concept is described in detail, which is the proton amplitude in neutron-rich carbon isotopes.

In general the state of a nucleus is described by the wave function $|\psi\rangle$ which is a solution of the Schrödinger equation

$$\mathbf{H}|\psi\rangle = E|\psi\rangle \tag{2.31}$$

with the Hamiltonian $\mathbf{H}$ describing the interaction between the nucleons in the nucleus and the energy E of the system. Since solving the Schrödinger equation with a realistic nucleon-nucleon interaction is a tedious and computational challenging task, several ways to solve it

approximately were developed. One is the independent particle or shell model for which the force acting on one nucleon and caused by all other nucleons is averaged. But before this so-called mean field approach is introduced in the following section, I want to show how the resulting basis states of these calculations can be used to semiquantitatively describe a situation in which these states interact with each other.

The mixing of two basis states $|\phi_1\rangle$ and $|\phi_2\rangle$ with the energies E_1 and E_2 via an interaction V is described by the matrix equation

$$\begin{pmatrix} E_1 & V \\ V & E_2 \end{pmatrix} \begin{pmatrix} \psi_\mathrm{I} \\ \psi_\mathrm{II} \end{pmatrix} = \begin{pmatrix} E_\mathrm{I} \\ E_\mathrm{II} \end{pmatrix} \begin{pmatrix} \psi_\mathrm{I} \\ \psi_\mathrm{II} \end{pmatrix} \tag{2.32}$$

as it is done, e.g., by Richard Casten in [Cas00]. The resulting mixed wave functions $|\psi_\mathrm{I}\rangle$ and $|\psi_\mathrm{II}\rangle$ have the energies E_I and E_II, respectively. They are given by

$$|\psi_\mathrm{I}\rangle = \alpha\,|\phi_1\rangle + \beta\,|\phi_2\rangle \tag{2.33}$$

$$|\psi_\mathrm{II}\rangle = -\beta\,|\phi_1\rangle + \alpha\,|\phi_2\rangle \tag{2.34}$$

with the mixing amplitudes α and β and $\alpha^2 + \beta^2 = 1$. The mixing of the two states depends only on two variables. One is the energy difference between the unperturbed basis states ΔE_u, the other one the strength of the mixing interaction V. They can be combined to the mixing ratio $R = \Delta E_\mathrm{u}/V$. The energies of the mixed states are then given by

$$E_\mathrm{I,II} = \frac{1}{2}(E_1 + E_2) \mp \frac{\Delta E_\mathrm{u}}{2}\sqrt{1 + \frac{4}{R^2}}. \tag{2.35}$$

Additionally, the mixing amplitude β can be expressed as

$$\beta = \frac{1}{\sqrt{1 + \left[\frac{R}{2} + \sqrt{1 + \frac{R^2}{4}}\right]^2}}. \tag{2.36}$$

A comparison of the unmixed basis states with the mixed final states is sketched in Figure 2.3.

One can now examine the two limiting cases. The first one is the one in which the basis states are degenerate, i.e., $\Delta E_\mathrm{u} = 0$. In this so-called strong mixing case the energy of the mixed states are given by

$$E_\mathrm{I,II} = E_0 \mp V \tag{2.37}$$

with the energy E_0 of the degenerate states. Furthermore, the mixing amplitudes are $\alpha = \beta = 1/\sqrt{2} \approx 0.707$, i.e., the two states are completely mixed. This leads to two conclusions: First of all, the smallest energy difference ΔE_p of perturbed final states is twice the interaction strength V. Furthermore, for degenerate states the mixing is independent of this strength.

On the other hand, in case of weak mixing the matrix element of the interaction strength V is much smaller than the energy gap of the unperturbed states. The mixing amplitude β is then given by $\beta \approx 1/R$ and the amount ΔE_s by which each energy is shifted is small. Therefore, one can extract the strength of the interaction easily from the energy gap ΔE_p, since

$$V \approx \beta \Delta E_\mathrm{u} \approx \beta \Delta E_\mathrm{p}. \tag{2.38}$$

The configuration mixing will be used in Section 2.2.2 for the description of the first excited 2_1^+ state as the mixing of a pure proton and a pure neutron excitation. But to start with, the basic concepts of the models forming the basis states will be introduced in the following section.

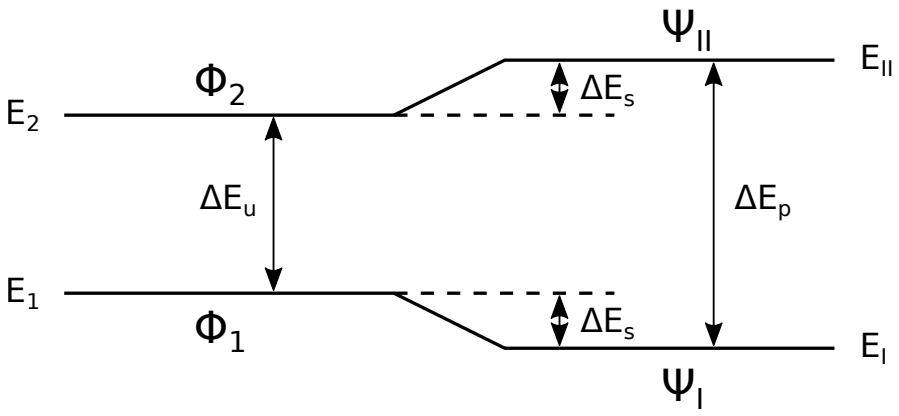

Figure 2.3: Sketch of the energy levels of two unperturbed states $|\phi_1\rangle$ and $|\phi_2\rangle$ (left) and of the two perturbed states $|\psi_I\rangle$ and $|\psi_{II}\rangle$ (right). The states mix via an interaction *V*. The sketch is based on [Cas00].

2.2.1 Independent Particle and Shell Model

To describe the nucleons in the nucleus one needs a model for the force between the nucleons. In addition to the well known Coulomb force acting on the protons, the nuclear force is described in several different ways. All of them have in common that the nuclear force is short range and attractive with a repulsive core. Due to its short range, it saturates. Although the nuclear force stems from the residual interaction of the strong force between the quarks and gluons within the nucleons, it is rather weak in comparison to the typical kinetic energies of the nucleons inside the nucleus.

However, the nucleus is usually not described via the nuclear force directly but via a potential as part of the Hamiltonian **H** in the Schrödinger equation, c.f. Equation 2.31. The Hamiltonian consists of the kinetic energy **T** and the potential **V** between the nucleons. This potential can be approximated by a mean field describing the effect of all the surrounding nucleons on a single nucleon. The residual interactions between the single nucleons can then be treated as a small modification to the overall Hamiltonian. To justify the picture of particles moving independently in a mean field, one needs to assume no interaction between the nucleons and a large free path of the nucleons, respectively. Although the nucleus is densely packed, this assumption is valid, since the Pauli principle forbids the scattering of nucleons into already filled states. Therefore, only states close to the Fermi surface can contribute to the scattering processes.

There are several ways to describe this mean field potential. It can, e.g., be extracted from two- or three-body interactions. The Yukawa potential is one of the first general descriptions [Yuk35] of such an interaction. Nowadays phenomenological descriptions of the interaction like the Argonne V18 potential [WSS95] or modern chiral effective field theories [ME11] are used. In most of these cases the description of the nucleus is based on two-body interactions. However, exotic nuclei call for the inclusion of three-body interactions to be able to, e.g., predict the neutron dripline for neutron-rich oxygen isotopes correctly [OSH+10].

In this work, I want to shortly introduce one of the simplest potentials able to reproduce the magnetic numbers for stable nuclei. This independent particle model describes noninteracting particles in a spherically symmetric potential. It is introduced in various textbooks, e.g., in

the one from Richard Casten [Cas00] or Kenneth Krane [Kra88]. Although it is only valid for nuclei with one particle or hole away from a closed shell, it can be used to get a feeling for the behavior of nuclei all over the chart of nuclei. The potential is given by a central potential $V_0(r)$, a potential $V_{ls}(r)$ describing the strength of the spin-orbit coupling and the Coulomb potential $V_C(r)$

$$V(\mathbf{r}) = V_0(r) + V_{ls}(r)\,\mathbf{l}\cdot\mathbf{s} + V_C(r) \tag{2.39}$$

with the angular momentum $\mathbf{l}$ and the spin $\mathbf{s}$ of the nucleon. Since the spin-orbit term is surface dominated, its strength is proportional to the derivative of the central potential $V_{ls}(r) \propto \partial V_0(r)/\partial r$. The most common descriptions of the central potential $V_0(\mathbf{r})$ are the harmonic oscillator and the Woods-Saxon potential. The harmonic oscillator potential at a distance r together with a term including the centrifugal force is given by

$$V_0(\mathbf{r}) = \frac{1}{2}m\omega^2 r^2 + \frac{\hbar^2}{2m}\frac{l(l+1)}{r^2}. \tag{2.40}$$

In this case, m is the mass and l is the angular momentum of the nucleon in the potential, while ω is the eigen frequency. The Woods-Saxon potential [WS54], which is connected to the density distribution of the nucleons in the nucleus, is given by

$$V_0(\mathbf{r}) = \frac{-V_0}{1+\exp\left(\frac{r-R_0}{a_0}\right)}, \tag{2.41}$$

where R_0 is the radius of the nucleus, V_0 the depth and a_0 the diffuseness parameter of the potential.

Solving the Schrödinger equation with the potential from Equation 2.39 separately for protons and neutrons results in wave functions with distinct energy levels called single particle energies depicted in Figure 2.4. The ordering of the levels is only an example. It differs for heavier nuclei due to the influence of the number of nucleons and the size of the nucleus on the energy and the extension of the wave functions. Since the Pauli principle forbids fermions to be in exactly the same state, these levels are filled consecutively beginning with the lowest energy. Each level is labeled with its principal quantum number n, its angular momentum l, and the total angular momentum $j = l \pm 1/2$. The angular momentum is labeled with s for $l = 0$, p for $l = 1$, d for $l = 2$, and so forth. A single level is usually called an orbit, while a group of orbits with similar energies forms a shell. Large gaps between shells correspond to the so-called magic numbers. They emerge when an additional nucleon needs to occupy a new shell. Due to the notably higher single particle energy, this nucleon and the corresponding nucleus is less bound than the magic nucleus.

If only the central potential – either harmonic oscillator or Woods-Saxon – is taken into account, the sequence of orbits follows the one shown on the left in Figure 2.4. Taking into account the magnetic substates and the spin of the protons and neutrons, each orbit can be filled with $2(2l+1)$ particles. However, as one can see in Figure 2.4, the shell gaps do not fit to the magic numbers above 20 observed in stable nuclei.

Including the spin-orbit potential as proposed by Maria Goeppert Mayer [May49] and Haxel et al. [HJS49] leads to a splitting of the states belonging to the angular momentum l into a

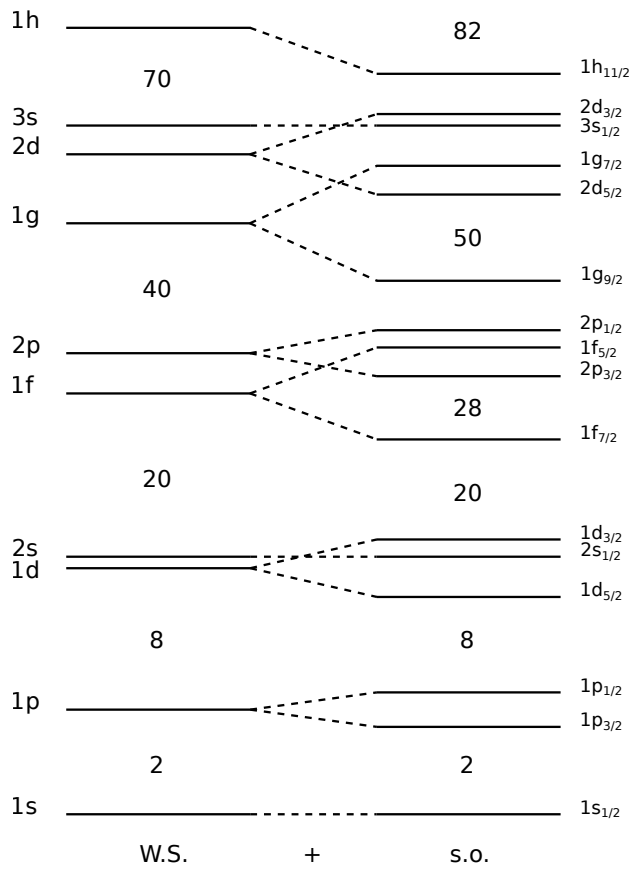

Figure 2.4: Single particle energies for the independent particle model with the Woods-Saxon potential (left) plus the spin-orbit potential (right). With the inclusion of the spin-orbit term, the large gaps between groups of orbits reproduce the magic numbers examined in stable nuclei. The exact ordering of the levels depends on the nucleus of interest. The sketch is based on [Cas00].

$j = l + 1/2$ and a $j = l - 1/2$ orbit. Each of these orbits can be filled with $2j + 1$ particles. Due to the negative value of $V_{\mathrm{ls}}(r)$, the energy of the $l + 1/2$ orbit is significantly lowered. Because of the intrusion of orbits belonging to higher shells into the subjacent shell, the shell gaps are shifted and the magic numbers appear as one can see on the right side of Figure 2.4. Since the intruding orbit stems from a different harmonic oscillator shell, it has a different parity than the rest of the shell. States belonging to this unique parity orbit are usually very pure and do not mix with neighboring states since only the weak force can mix states with different parities.

Finally, the Coulomb potential, which has only an effect on protons due to their electric charge, is the only long range part of the potential. For nuclei with a large number of protons Z it leads to a larger neutron to proton ratio in stable nuclei. This can be seen by the bending of the valley of stability in the chart of nuclei.

While the independent particle model contains only the mean field in which the nucleons move independently, the shell model includes residual interactions between valence nucleons. Thus, it is not only valid for nuclei with one valence particle but also for nuclei with multiple valence particles. The residual interaction is, e.g., responsible for the $J = 0$ coupling of two nucleons in the same orbit. Additionally, it includes the breaking of shells and the interaction of valence

nucleons with the lower lying nucleons in the closed shells. The strength of this interaction depends on the overlap of the wave function of the valence nucleon with the wave functions of the nucleons in the closed shell and – since all closed shells are spherically symmetric – only on its radial part. Therefore, the magnetic subshell m has no influence.

Today, several shell models exist which incorporate such residual interactions. They are usually specialized on a certain part of the chart of nuclides. For neutron-rich carbon isotopes, e.g., the WBP and WBT interactions [WB92] are a good choice to describe the nucleons in the $1p$ and $2s1d$ orbits.

2.2.2 Proton Amplitude

The concept of configuration mixing introduced in Section 2.2 can be used to describe the first excited 2^+_1 state in neutron-rich, even-even carbon isotopes. To motivate the picture of the proton amplitude, a closer look to the occupation of the different orbits in the carbon and nitrogen isotopes of interest is helpful. As given by Petri et al. [PPC+12] and depicted in Figure 1.1, the $0^+_{\text{g.s.}}$ ground state of the carbon isotopes can be described within the shell model as

$$|0^+_{\text{g.s.}}; {}^A\text{C}\rangle = \gamma \, |\nu(sd)^n; J=0\rangle \otimes |\pi(1p_{3/2})^4; J=0\rangle \tag{2.42}$$

$$+ \delta \, |\nu(sd)^n; J=2\rangle \otimes |\pi(1p_{3/2})^4; J=2\rangle \tag{2.43}$$

with $n = 2, 4, 6$ for ^{16}C, ^{18}C, and ^{20}C, respectively. Here, the last neutrons are located in a degenerate sd shell as described in Section 1.1. Since a higher excitation energy is expected for the second term, it can be assumed that only the first term contribute to the ground state, i.e., $\gamma = 1$ and $\delta = 0$. Additionally, the 2^+_1 excited state can be described as

$$|2^+_1; {}^A\text{C}\rangle = \alpha \, |\nu(sd)^n; J=2\rangle \otimes |\pi(1p_{3/2})^4; J=0\rangle \tag{2.44}$$

$$+ \beta \, |\nu(sd)^n; J=0\rangle \otimes |\pi(1p_{3/2})^3(1p_{1/2})^1; J=2\rangle. \tag{2.45}$$

In doing so, α and β are the mixing amplitudes from Section 2.2, which denote the amount of pure neutron or pure proton excitation contributing to the excited state. β is called the proton amplitude and can be accessed via one-proton knockout reactions from nitrogen isotopes. Their ground state is given by

$$|1/2^-_{\text{g.s.}}; {}^{A+1}\text{N}\rangle = |\nu(sd)^n; J=0\rangle \otimes |\pi(1p_{3/2})^4(1p_{1/2})^1; J=1/2\rangle. \tag{2.46}$$

The proton in the $1p_{1/2}$ orbit coupling to the first excited 2^+_1 state in ^{A}C cannot produce the $1/2^-$ ground state in $^{A+1}$N. Therefore, the removal of a proton from the ground state of the nitrogen isotopes does not populate the neutron component but only the proton component of the excited 2^+_1 state. With this, the reaction is suitable to populate only the pure proton excitation and to determine the proton amplitude, respectively. The removal of the proton in the $1p_{1/2}$ orbit populates the 0^+ ground state of ^{A}C. Thus, its spectroscopic factor is expected to be 1. The 2^+_1 excited state of interest is populated if one of the protons in the $1p_{3/2}$ orbit is knocked-out and the remaining protons in the $1p_{3/2}$ and $1p_{1/2}$ orbit couple to 2^+. This happens in five out

of eight cases. With four protons in the $1p_{3/2}$ orbit, the ratio of the spectroscopic factors is then proportional to the square of the proton amplitude

$$\frac{C^2S(2_1^+)}{C^2S(0_{\text{g.s.}}^+)} \approx \frac{\beta^2 \times 4 \times \frac{5}{8}}{1} = \beta^2 \times \frac{5}{2}. \tag{2.47}$$

Since the spectroscopic factor is the connection between the experimental cross section σ_{exp} and the cross section from reaction theory σ_{theo}, this relationship can be translated into a ratio of the experimental cross section of the excited and the ground state

$$\frac{\sigma_{\text{exp}}(2_1^+)}{\sigma_{\text{exp}}(0_{\text{g.s.}}^+)} = \frac{C^2S(2_1^+)}{C^2S(0_{\text{g.s.}}^+)} \times \frac{\sigma_{\text{theo}}(1p_{3/2})}{\sigma_{\text{theo}}(1p_{1/2})} \approx \beta^2 \times \frac{5}{2} \times \frac{\sigma_{\text{theo}}(1p_{3/2})}{\sigma_{\text{theo}}(1p_{1/2})} \tag{2.48}$$

with $\sigma_{\text{exp}}(2_1^+) = C^2S(2_1^+)\ \sigma_{\text{theo}}(1p_{3/2})$ and $\sigma_{\text{exp}}(0_{\text{g.s.}}^+) = C^2S(0_{\text{g.s.}}^+)\ \sigma_{\text{theo}}(1p_{1/2})$. The theoretical cross sections $\sigma_{\text{theo}}(1p_{3/2})$ and $\sigma_{\text{theo}}(1p_{1/2})$ are calculated in the Glauber framework as explained above. The results for both knockout and QFS reactions are presented in Section 6.1.1.

Although this equation is valid for both reaction types, the proton amplitude in Section 6.2 is determined only from QFS data. The reason for this is the smaller uncertainty of the experimental cross sections for QFS reactions in comparison to the ones for knockout reactions due to a larger number of events and a cleaner selection mechanism.

In addition, one expects to find a second state with

$$|2_2^+; {}^A\text{C}\rangle = -\beta\ |\nu(sd)^n; J=2\rangle \otimes |\pi(1p_{3/2})^4; J=0\rangle \tag{2.49}$$

$$+\alpha\ |\nu(sd)^n; J=0\rangle \otimes |\pi(1p_{3/2})^3(1p_{1/2})^1; J=2\rangle. \tag{2.50}$$

In this case, the proton excitation is proportional to α, and with this, the cross section to populate this state is proportional to α^2. With a relatively small contribution of the protons to the first excited 2_1^+ state, the second 2_2^+ state is dominated by the proton excitation. Thus, the probability to populate the mixed symmetry state is much larger than the one for the first excited 2_1^+ state. However, if a relatively weak mixing is assumed, the energies of the mixed states are close to the energies of the unperturbed states. The energies of the unperturbed states can be estimated by the comparison with ^{14}C and ^{18}O depicted in Figure 1.3. For ^{14}C the 2_1^+ state at $E(^{14}\text{C}, 2_1^+) = 7.012(4)\,\text{MeV}$ [AS91] is caused mostly by proton excitation, while for ^{18}O the 2_1^+ state at $E(^{18}\text{O}, 2_1^+) = 1.982(1)\,\text{MeV}$ [AS87] is caused mostly by neutron excitation. Therefore, one expects the first 2_1^+ state at $E(2_1^+) \approx 2\,\text{MeV}$ and the second one at $E(2_2^+) \approx 7\,\text{MeV}$, c.f. Wiedeking et al. [WFM+08]. The energies of the first excited 2_1^+ states in ^{16}C, ^{18}C, and ^{20}C listed in the following section and in Figure 2.5 match this expectation. Thus, the mixed symmetry state will be above the neutron separation energy S_{n} for these nuclei. In this case, the $^{A-1}$C fragment and the emitted neutron need to be measured. The energy of the resonance can then be reconstructed with the invariant-mass method from the four-momenta of the fragment and the neutron.

2.3 Previous Measurements

As mentioned before, the focus of this work lies on the extraction of inclusive and exclusive cross sections for knockout and QFS reactions as well as the determination of the proton

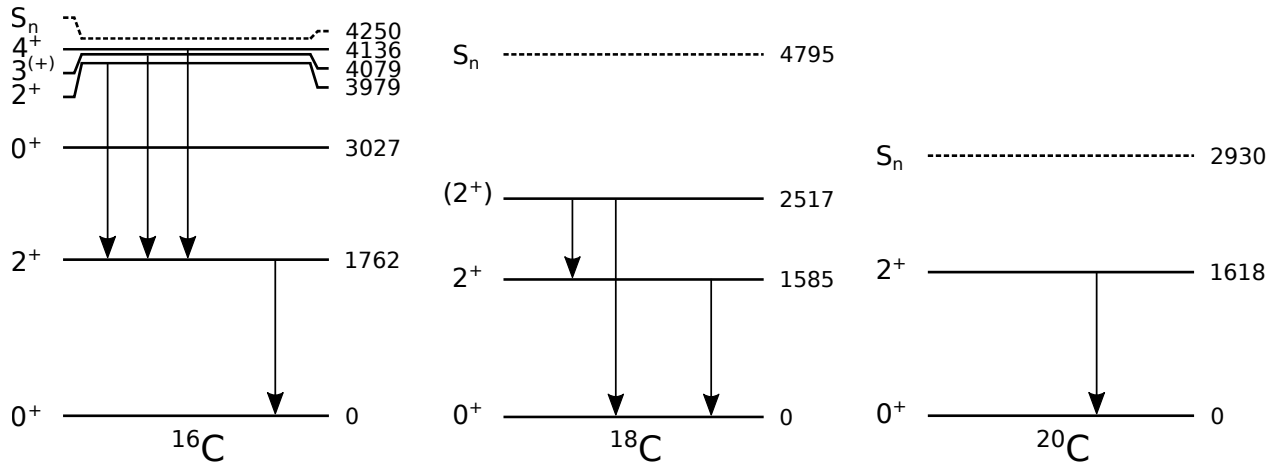

Figure 2.5: Level schemes of ^{16}C (left), ^{18}C (middle), and ^{20}C (right). The energies of the levels are given in keV and are taken from [PPC$^+$12, WBB$^+$10] for ^{16}C, from [VBB$^+$12] for ^{18}C, and from [PFM$^+$11] for ^{20}C. The neutron separation energies S_n are given in keV as well and taken from [WAW$^+$12].

amplitude. Hence, the first excited 2^+_1 states of the isotopes ^{16}C, ^{18}C, and ^{20}C are of special interest. The energy of these states, as well as additional higher lying excited states feeding the states of interest, were measured before with the use of several experimental techniques. This includes among others [WFM$^+$08, WBB$^+$10, PPC$^+$12] for ^{16}C, [SSS$^+$08, VBB$^+$12] for ^{18}C, and [SSS$^+$08, PFM$^+$11] for ^{20}C. Since there are no big discrepancies between the different measurements, I chose one level scheme for each isotope as input for my simulations introduced in Section 5.3. The adopted level schemes are depicted in Figure 2.5.

The proton amplitude for ^{16}C was measured before by Petri et al. [PPC$^+$12]. The experiment was conducted at the National Superconducting Cyclotron Laboratory (NSCL) using the A1900 fragment separator for the production and the identification of the incoming ^{17}N isotope and the S800 spectrometer and the γ-ray spectrometer SeGA for the identification of the outgoing particles and their excited states. The states of interest were populated with a proton knockout reaction on a beryllium target: ^{17}C(^{9}Be,^{16}C)X. Among others, the proton amplitude was found to be $\beta^2 = 11(1)\,\%$ using the same approach as introduced in the previous section.

Additionally, Macchiavelli et al. [MPF$^+$14] predicted the proton amplitude for ^{18}C and ^{20}C from the measured $B(E2; 2^+_1 \rightarrow 0^+_1)$ values, c.f. Figure 1.2 in Section 1.1. To do so, the authors assume a two-state mixing of a pure proton and a pure neutron excitation for the first excited 2^+_1 state. Afterwards, they calculate the quadrupole transition strength in the seniority scheme and compare them with the experimental values. This indirect, phenomenological analysis results in a proton amplitude of $\beta^2(^{18}\text{C}) = 13\,\%$ and $\beta^2(^{20}\text{C}) \gtrsim = 30\,\%$ since the increase in $B(E2)$ strength for ^{20}C is explained by an increase of the contribution of the proton excitation.

This increase of the proton amplitude can be understood by taking the tensor force into account in shell model calculations. Otsuka et al. [OSF$^+$05] describe the tensor force as a distinct manifestation of the nuclear force caused by the meson exchange as, e.g., described by the Yukawa potential [Yuk35] or the chiral effective field theory [ME11]. It influences the single

particle energies and with this drives the shell evolution. The most common description of the tensor force is

$$V_{\mathrm{T}}(r) = (\tau_1 \cdot \tau_2)\, S_{12} V(r) \tag{2.51}$$

with the function S_{12} given, e.g., by [Kra88], as

$$S_{12} = 3\left(\mathbf{s_1} \cdot \frac{\mathbf{r}}{r}\right)\left(\mathbf{s_2} \cdot \frac{\mathbf{r}}{r}\right) - (\mathbf{s_1} \cdot \mathbf{s_2}). \tag{2.52}$$

$V(r)$ is a function of the distance r, while τ_i and $\mathbf{s}_i$ are the isospin and spin operator of the particle i.

With this force, nucleons in an orbit j' influence the single particle energies of nucleons in the orbit j. The monopole component of the interaction V can be described by

$$V^T_{j,j'} = \frac{\sum_J (2J+1)\, \langle jj'|V|jj'\rangle_{JT}}{\sum_J (2J+1)}, \tag{2.53}$$

where $\langle jj'|V|jj'\rangle_{JT}$ is the diagonal matrix element for the state $|jj'\rangle_{JT}$ in which the two nucleons couple to total angular momentum J and isospin T. The sum takes only those states into account which fulfill the antisymmetrization condition. Therefore, Equation 2.53 is angle independent, i.e., it describes the monopole part of the interaction. Nevertheless, it is still isospin dependent. It can be shown [OSF+05] that this monopole interaction is two times stronger for neutron-proton interactions than for the $T = 1$ interaction, i.e., for nucleons of the same kind. Furthermore, the larger the angular momentum l, the stronger the tensor monopole interaction.

Finally, the shift of the single particle energy of a proton in the j orbit due to neutrons in the j' orbit is given by

$$\Delta\epsilon_{\mathrm{p}}(j) = \frac{1}{2}\left(V^{T=0}_{j,j'} + V^{T=1}_{j,j'}\right) n_{\mathrm{n}}(j') \tag{2.54}$$

with $n_{\mathrm{n}}(j')$ the expectation value of the neutrons in the j' orbit. The shift of the neutron single particle energies due to protons are calculated accordingly. One can now compare the effect of the neutrons in the $j' = j'_> = l' + 1/2$ orbit on the proton orbits $j = j_> = l + 1/2$ and $j = j_< = l - 1/2$. The tensor force is repulsive between $j_>$ and $j'_>$, while it is attractive between $j_<$ and $j'_>$. For an increasing neutron number, this raises the single particle energy of the $j_>$ orbit and lowers the one of the $j_<$ orbit. Therefore, the gap between the $j_>$ and the $j_<$ orbit shrinks. On the other hand, neutrons in the $j'_< = l' - 1/2$ orbit have an attractive effect on the protons in $j_>$ and a repulsive effect on the ones in $j_<$.

However, Equation 2.54 is only valid for protons and neutrons in different orbits. In addition, both orbits should be close to the Fermi surface. In this case the radial wave functions have a sharp peak at the surface and, therefore, have a large overlap. Both assumptions are valid for the carbon isotopes of interest. With more and more neutrons filling the $1d_{5/2}$ orbit, the single particle energy of the $1p_{3/2}$ orbit is lifted up, while the energy of the $1p_{1/2}$ orbit is lowered. Due to this reduction of the spin-orbit splitting between the $1p_{3/2}$ and the $1p_{1/2}$ orbit, the excitation of protons becomes easier and the proton amplitude increases.

3 Experimental Setup

The experimental data were taken during the campaign S393 with the R^{3}B/LAND setup at GSI in 2010. This setup allows kinematically complete measurements of nuclear reactions in inverse kinematics. In this chapter, the production of the incoming radioactive ion beam and the R^{3}B/LAND setup with all its detectors will be introduced. The detectors used for this work will be explained in more detail afterwards. In the last part of this chapter, the DAQ and the trigger system will be introduced.

3.1 Beam Production

The radioactive ion beam cocktail delivered to the R^{3}B/LAND setup is produced with the in-flight technique at the GSI accelerator facility in Darmstadt. An overview of the GSI facility available in 2010 is depicted in Figure 3.1. In the case of the S393 campaign, stable ^{40}Ar is used as a primary beam. The ions from the source are accelerated by the UNIversal Linear ACcelerator (UNILAC) up to an energy of ≈ 11.5 AMeV. They are partly stripped and as $^{40}Ar^{11+}$ ions injected into the SchwerIonenSynchrotron18 (SIS18), which has a maximum available magnetic rigidity of 18 Tm as implied by its name. It accelerates the ions further to an energy of 490 AMeV, before they are guided to the FRagment Separator (FRS). The beam is extracted in so-called spills. During the S393 campaign, the spills had a length of 2 s and the intensity of the primary ions at the target area of the FRS was 6×10^{10} /s.

The FRS is a high resolution forward spectrometer used for the production and analysis of radioactive ion beams. Its technical design is explained in detail by Hans Geissel et al. [GAB$^+$92], while its layout is depicted in Figure 3.2. At the entrance of the FRS the production target – in the case of this work a Be target with a thickness of 4011 mg/cm^2 – is placed. A wide range of radioactive ions are produced via fragmentation reactions. The ions are then separated and selected with a series of four dipole magnets. Additional quadrupole and sextupole magnets are used to focus and stabilize the beam. The dipole magnets separate the fully stripped ions according to their mass-over-charge ratio A/Z using

$$B\rho \propto \frac{A}{Z}\beta\gamma \tag{3.1}$$

with the magnetic rigidity $B\rho$ consisting of the magnetic field B of the dipole magnet and the curvature ρ of the trajectories through the field, the Lorentz factor γ and the relativistic velocity β of the traversing particles. The use of six different $B\rho$ settings during the experimental campaign allowed for the measurement of a wide range of radioactive ions.

At each focal plane, several detectors for beam diagnostics are placed. For the presented analysis the scintillators at the focal planes S2 and S8 are of special interest. Together with the first detector in the R^{3}B/LAND setup, POS, they are used for Time-Of-Flight (TOF) measurements to deduce the velocity of the particles. Although the scintillator at S2 is preferred due to its large distance to POS ($\approx$ 136 m), the scintillator at S8 with a distance of $\approx$ 55 m is used since the scintillator at S2 was overloaded with the high intensity of the beam.

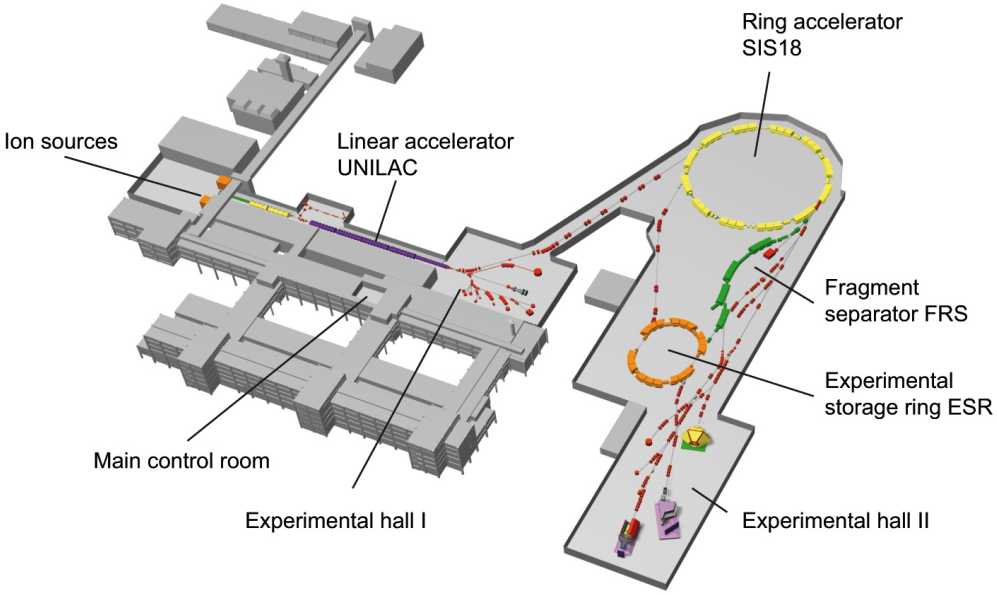

Figure 3.1: Sketch of the GSI accelerator complex. The stable primary beam is accelerated by UNILAC and SIS18 before it hits the production target at the entrance of the FRS. The secondary beam of radioactive ions is then guided to Cave C in the experimental hall II in which the R^{3}B/LAND setup is placed. The picture is taken from [GSI18].

Additionally, a wedge-shaped degrader can be inserted in the beam in the dispersive focus S2 to further select the outgoing fragments. With this so-called $B\rho - \Delta E - B\rho$ method, the fragments are slowed down by the degrader making use of the dependency of the energy loss on Q^2. Furthermore, after the first two dipole magnets the isotopes are separated according to their A/Z ratio on the focal plane. Because of the shape of the degrader, the different species are passing through different thicknesses and therefore experience a different energy loss. Thus, unwanted isotopes can be bent out of the beam in the second stage of the FRS. However, due to the wide range of topics addressed in this experimental campaign, a sharp selection of single isotopes was not favored and therefore no degrader was used at S2. Instead a cocktail beam with a wide range of isotopes was guided to Cave C, where the R^{3}B/LAND setup is located.

3.2 R^{3}B/LAND Setup

The R^{3}B/LAND setup is a versatile setup with a variety of detectors that can be used depending on the aim of the experiment. It is located in Cave C in the experimental hall II where A Large Acceptance DIpole magNet (ALADIN) was placed. The goal of the experimental campaign S393 was the investigation of light neutron-rich nuclei. It included measurements of (n,γ) rates for the r-process nucleosynthesis derived from Coulomb dissociation [AAA$^+$14, RAA$^+$16, HTW$^+$17] as well as various studies on shell evolution and structure using QFS reactions [Naj13, Hol14, Kah15, FAPC$^+$18] including a systematic study on the quenching of single-particle spectroscopic factors for oxygen isotopes [APB$^+$18]. Additionally, properties like ground state energy, width and lifetime of nuclei beyond the dripline, e.g., ^{25}O and ^{26}O [CSA$^+$13]

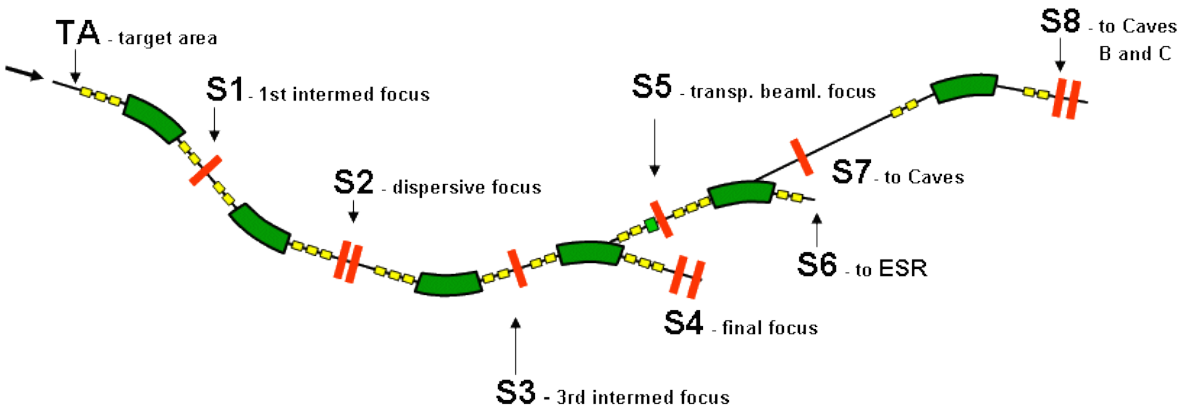

Figure 3.2: Sketch of the FRS. Radioactive isotopes are produced via fragmentation reactions when the incoming stable beam hits the production target at the target area TA. The fragments are separated using a sequence of dipole magnets (green), while the quadrupole magnets (yellow) focus the beam in the x and y direction. At the dispersive focus S2 a wedge-shaped degrader can be installed to select certain fragments in the outgoing beam. The fragments can either be analyzed at the final focus S4 or can be guided to other experimental setups like, e.g., the R^{3}B/LAND setup in Cave C. At each focal plane S1 - S8 several detectors for beam diagnostics are placed. The picture is taken from [frs18].

or ^{13}Be [RNT$^+$18] were investigated. Moreover, studies of the effective proton-neutron interaction in neutron-rich fluorine isotopes [VLS$^+$17] and of fragmentation reactions on light carbon and boron isotopes [THA$^+$16] were carried out.

All these measurements use the feasibility of kinematically complete measurements of reactions at relativistic energies at the R^{3}B/LAND setup shown in Figure 3.3. It allows to measure the incoming particles and the outgoing fragments as well as the produced neutrons, protons and γ rays on an event-by-event basis. To cover the wide range of isotopes required by the experiment proposal, six different FRS settings were used ranging from $A/Z \approx 1.66$ up to $A/Z \approx 3$ with an energy of $(390-430)$ AMeV. The high energy of the incoming beam results in forward focusing of the outgoing particles. Therefore, in the laboratory system only a relatively small acceptance is necessary to detect almost all reaction products.

The scintillators S8 and POS, as well as the Position Sensitive Pin diode (PSP) in the beginning of the setup, are used to identify the incoming particles. The TOF between S8 in the FRS setup and POS in Cave C is used to determine their velocity β. Together with the energy loss in the PSP, the charge Q of the fully stripped ions arriving from the FRS is determined via the Bethe formula [PoPDG16, p. 442]

$$-\frac{dE}{dx} = K\frac{Z}{A}\frac{Q^2}{\beta^2}\left[\frac{1}{2}\ln\frac{2m_e c^2\beta^2\gamma^2 W_{\max}}{I^2} - \beta^2\right]. \tag{3.2}$$

Here $W_{\max}$ is the maximum possible energy transfer of a single collision, I the mean excitation energy, $K = 4\pi N_A r_e^2 m_e c^2$ and $r_e = e^2/(4\pi\epsilon_0 m_e c^2)$ the classical electron radius. Since the ions are fully stripped, the charge number Z and the measured charge Q are equivalent. The mass-over-charge ratio A/Z and the mass A, respectively, can then be determined via the flight path through the FRS dipole magnets using Equation 3.1.

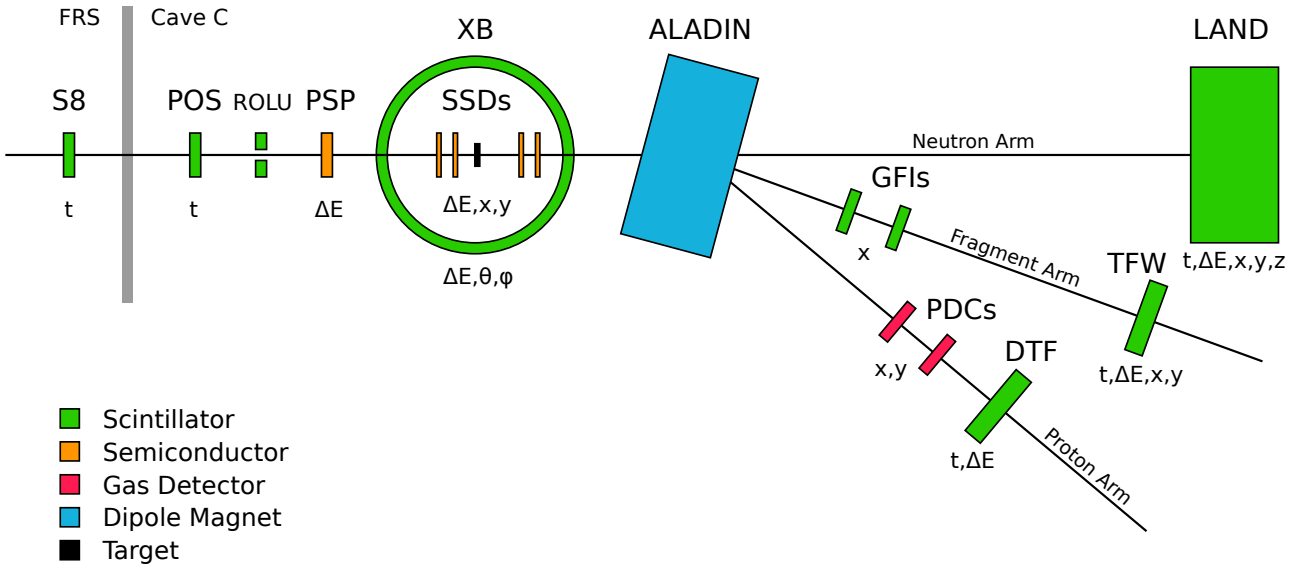

Figure 3.3: Schematic picture of the R^{3}B/LAND setup at GSI in Darmstadt during the experiment S393. The detectors in front of the target are used for the ID of the incoming isotopes, while the detectors after the target are used for the ID of the reaction products. XB surrounds the target chamber and detects γ rays, protons, and neutrons from reactions in the target. Fast neutrons are emitted in forward direction and are detected by LAND in the neutron arm. The outgoing fragments and fast protons are emitted in forward direction as well and bend by the dipole magnet ALADIN into the fragment and proton arm, respectively. All detectors in front of ALADIN except XB are placed in vacuum, while all detectors behind it are operated in air. The detectors and their purposes are explained in the text.

For the outgoing particles a similar procedure is necessary, which is explained in detail in Section 4.3. The TOF measurement to determine the velocity of the outgoing particles is done between POS and the Time-of-Flight Wall (TFW). Since this time information includes energy loss within the tracking detectors as well as during the reaction in the target, it is corrected using ATIMA [Wei18a] and *Ralf's tracker* [Pla18b] to estimate the energy losses. Together with the energy loss in two Silicon Strip Detectors (sSSDs) behind the target and the TFW, the charge number Z of the outgoing fragments is then determined as explained before for the incoming particles. Position information from the two SSDs, two Großer FIber detectors (sGFIs), which are placed behind the dipole magnet ALADIN and determine the x-position of the traversing particles, and the TFW is used to determine the flight path of the outgoing fragments. Again the mass-over-charge ratio A/Z is determined using Equation 3.1. It takes into account the flight path, the velocity β of the outgoing fragments and the magnetic field B of the dipole magnet, which bends the fragments into the fragment arm consisting of the aforementioned GFIs and the TFW.

Finally, several additional reaction products like neutrons, protons, and γ rays need to be detected and identified. Since neutrons are not bent by the magnetic field of ALADIN, those emitted in forward direction are detected with the neutron detector LAND. Neutrons not flying in forward direction, e.g., from QFS reactions, are detected with Crystal Ball (XB). Similarly, protons are either detected in the proton arm – when they are emitted in forward direction and

bent by ALADIN – or with XB around the target area. The proton arm is equipped with two Proton Drift Chambers (sPDCs) measuring the position of the protons and the Dicke ToF Wand (DTF) for the time measurement. γ rays, which are emitted instantaneously, are detected with XB.

All detectors placed behind ALADIN are in air, while almost all detectors in front of ALADIN are located in the beam pipe or the target chamber and are therefore in vacuum. The only exception is XB, which surrounds the target chamber. The detectors in air include LAND as well as all detectors in the fragment arm (GFIs, TFW) and the proton arm (PDCs, DTF).

3.3 Detectors

After the overview over the R^3B/LAND setup in the previous section, selected detectors and their functionalities are presented in this section. I focus on detector systems important for the analysis done for this work. Since I am neither interested in protons emitted in forward direction nor in neutron-removal reactions, I do not introduce the detectors in the proton arm or LAND. Information about LAND can be found, e.g., in [BEE+92]. Likewise. I do not present the PSP detector, whose layout and calibration is described in detail by Stefanos Paschalis in [Pas08]. The calibration of each detector is not described in this section but is mentioned and if necessary explained in detail in Chapter 4.

POS and ROLU

The POS detector is the start detector of the R^3B/LAND setup. It detects the incoming particles. A valid POS signal (without a Rechts-Oben-Links-Unten (ROLU) signal) is an essential part of every on-spill trigger. Its time signal is used for velocity determination via TOF measurements of the incoming particles (TOF between S8 and POS) and the outgoing fragments (TOF between POS and TFW).

It consists of a square of scintillating material which is coupled via a light guide to four Photo Multiplier Tubes (sPMTs). It has an active area of $(5 \times 5)\,\mathrm{cm}^2$ and its thickness is chosen depending on the kinetic energy and the charge of the incoming ions. In case of the experiment S393 it was 2 mm thick. A sketch of the detector is shown in Figure 3.4 a). In addition to the TOF, the detector can be used for energy-loss measurements as well as for the determination of the position of the incoming particles using the time difference of two opposite PMTs. However, during the experimental campaign S393 the PSP and the SSDs are used for energy-loss and position measurements in front of the target and only the time information of POS is used for TOF measurements.

The purpose of the ROLU detector is to define the spot size of the beam. It consists of four movable scintillator paddles each with an area of $(9.5 \times 10)\,\mathrm{cm}^2$, a thickness of 5 mm, and read out by a PMT. The paddles are arranged around the beam in a way that only a small rectangle in the middle is not covered by them. A picture of the arrangement is shown in Figure 3.4 b). Only particles traversing through the empty spot are accepted. All particles which hit at least one scintillator paddle produce a signal used as a veto for recording. By moving the paddles mounted on drives the size of the accepted beam can be varied. It is usually chosen in a way that all accepted particles hit the target.

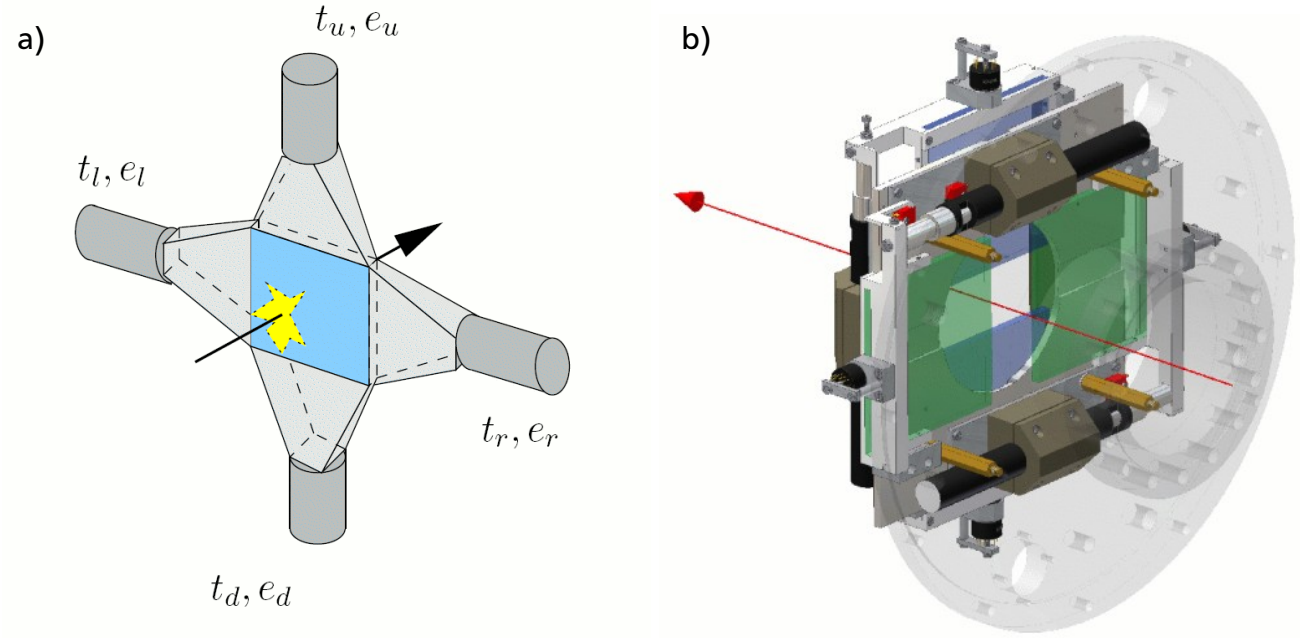

Figure 3.4: a) The sketch of the POS detector shows a passing ion (black arrow) producing light in the scintillator (blue square). Light guides are attached to each side of the square leading to four PMTs for time and energy measurements. b) On the technical drawing of the ROLU detector two scintillator plates each in the x (green) and y (blue) direction are shown together with the drive for moving them. The red arrow indicates the direction of an accepted ion not interacting with the ROLU scintillators. Both pictures are taken from [Pla18a].

SSDs

The trajectory of the incoming and outgoing particles is measured with eight SSDs surrounding the target area. The same kind of detectors are used for the tracker of the Alpha Magnetic Spectrometer (AMS) installed on the International Space Station (ISS), for which a detailed description is available [Zuc08]. Two detectors each are placed before and after the target, while the other four detectors build a box around the beam directly after the target. The positions of the detectors with respect to the target wheel inside the target chamber is sketched in Figure 3.5 a). These semiconductor detectors do not only provide position information with a very high resolution but also come with an energy-loss measurement for charge determination.

Each detector has an active area of $(72 \times 40)\,\mathrm{mm}^2$ and is 0.3 mm thick. Its ohmic side, called k-side, is segmented into 384 strip with a pitch width of $104\,\mu$m. The junction side, called s-side, is segmented into 2560 strips with a width of $27.5\,\mu$m, but only every fourth strip is read out to limit the number of readout channels. The strips are connected directly to the front-end electronics board through flexible capton cables. A detector together with the front-end electronics is depicted in Figure 3.5 b). The amplified signals are read out by the SIlicon DEtector REadout Modules (sSIDEREMs), which were especially designed for the readout of these detectors. They perform baseline and common-noise subtraction and digitize the signals to be recorded by the DAQ.

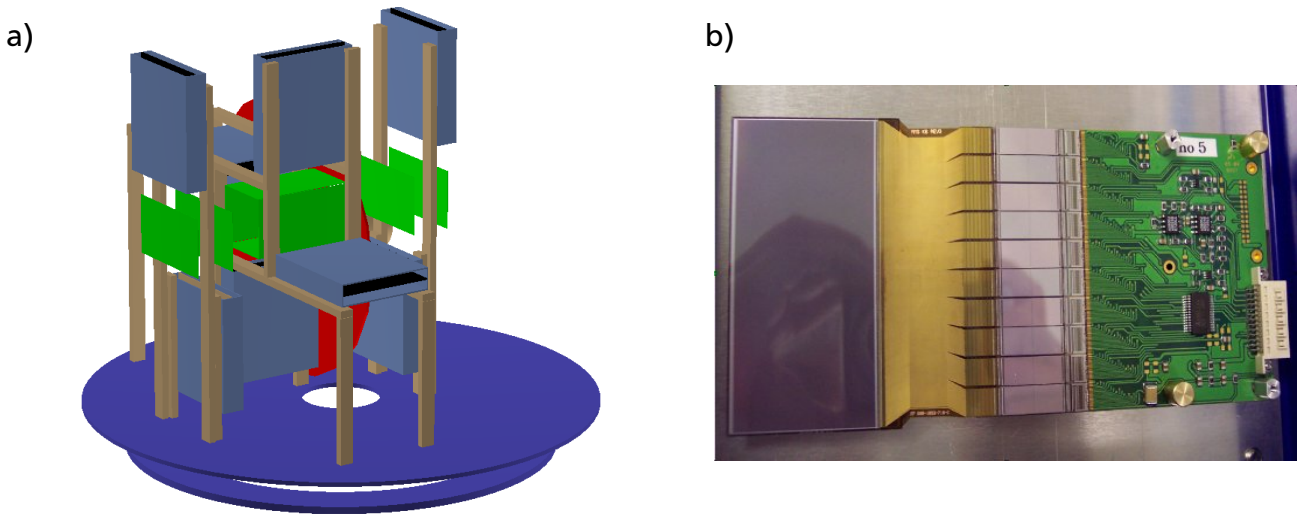

Figure 3.5: a) The arrangement of the eight SSDs around the targets in the target wheel is sketched as used for R3BRoot simulations: The active area of the detectors is depicted in green, the boards connected directly to the active area are enclosed in an aluminum housing depicted in grey-blue. The target wheel in red can be seen in the background. The whole construction is mounted on a disk (blue) which is placed in the spherical target chamber within XB. b) Photo of an SSD with the active area on the left connected via capton cables to the front-end electronics board on the right. The picture is taken from [Pla18a]

XB

To measure γ rays from the deexcitation of excited fragments and scattered protons, the XB detector is placed around the target area. XB was built beginning in 1979 and started its operation in 1982. It was used at the Universität Heidelberg before it moved to GSI. The technical specification of the original setup is described by Metag et al. [MHH+82]. It is made out of 162 NaI crystals, which cover almost 4π. Only the area of the beam pipe and the holding structure of the target chamber inside XB is not covered. The surface pointing to the target of 12 crystals are pentagons, while the surface of the other 150 crystals are hexagons in three different shapes. This way, all crystals cover the same area of the inner sphere with a diameter of 25 cm. Hence, they have an opening angle of 14°. The crystals are 20 cm thick and read out with PMTs. The arrangement of the crystals is depicted in Figure 5.1. The segmentation allows for multiplicity studies and the Doppler correction of the detected γ-ray energies and is therefore suited for experiments in inverse kinematics in which the particles emitting the γ rays are moving. However, the relatively large opening angle of each crystal introduces the dominant contribution to the energy resolution since the fragments are moving with a velocity of $v \approx 0.73\,c$.

In 2007, the readout of 64 crystals was modified to be able to measure the energy of protons (and neutrons) in QFS experiments. For this purpose, each of these crystals is read out twice. One signal, called γ-ray branch, is read out at the final pickup anode of the PMT as before, while the second signal, called proton branch, is read out at the last dynode. The proton branch is not amplified any further, whereas the γ-ray branch is preamplified. Hence, the proton branch has

a factor of 15 smaller amplification and its energy range is suited to measure the energy of the traversing protons. Additional differences exist in the readout. For the proton branch, only the energy is recorded using a Charge-to-Digital Converter (QDC), while the signal from the γ-ray branch is split to measure both its time and energy. On one end, the energy is recorded with a QDC. On the other end, the time signal is processed with a Constant Fraction Discriminator (CFD) and then recorded with a Time-to-Digital Converter (TDC). Furthermore, the time signals of several crystals together are used to provide a trigger signal for the whole detector. However, the trigger signal is produced before the CFD and experiences a walk effect. The modification is described in more detail by Felix Wamers [Wam11].

GFIs

Two fiber detectors called GFIs are used to measure the position of the outgoing fragments behind ALADIN. Each detector measures the position in one direction. During the S393 campaign, both GFIs were placed in a way that they measured the x position of the traversing particle, but they can also be used to measure both the x and y direction by rotating one detector by 90°. The position information is used to reconstruct the flight path of the fragments through the magnetic field of ALADIN and to calculate the mass-over-charge ratio A/Z of the reaction products.

Each detector consists of 480 scintillator fibers with a square cross section of $(1.0 \times 1.0)\,\mathrm{mm}^2$ and a length of 50 cm. The fibers are covered with a material with a lower refractive index to guide the light and an additional layer of white coating to avoid cross talk. Overall, they cover an area of $(50 \times 50)\,\mathrm{cm}^2$. Each fiber is read out on both ends. One end is connected to a conventional PMT for timing and triggering purposes together with the other 479 fibers. The readout of this PMT was not used during the experiment s393. The other end is connected to a Position-Sensitive PMT (PSPM) via a specially designed mask. The PSPM has 16 mesh type dynodes and a rectangular grid of anodes with 18 wires in one direction and 16 wires perpendicular to them. With this grid, the position on the PSPM can be determined. It is then correlated to the fiber number, and with this, to the position of the beam. An overview over the design and technical drawings are given in [CSG+98], while a detailed explanation of the calibration procedure of these detectors is given in [MJP+09].

TFW

As the last detector in the fragment arm, the TFW is mainly used for timing and energy-loss measurements but can be used as well for rough position measurements in both directions. It is built of two layers of scintillator paddles. The first plane is made out of 18 vertical paddles with a length of 147 cm. The second layer consists of 14 horizontal paddles with a length of 189 cm. With a width of 10 cm and a depth of 0.5 cm of each paddle, they cover an active area of $(147 \times 189)\,\mathrm{cm}^2$. Each paddle is wrapped to avoid cross talk and is read out with PMTs on both ends. The signal of the PMTs are split and digitized with an Analog-to-Digital Converter (ADC) for the energy-loss measurement and a TDC for the time measurement.

The energy-loss measurement is used to determine the charge of the outgoing particles using Equation 3.2. The TOF measurement between POS at the beginning of the setup and the TFW at the end of the fragment arm defines the velocity of the outgoing particles. Together with the various position measurements of other detectors, it is a key component to determine the

mass-over-charge ratio A/Z via Equation 3.1. The position of the hit can be either calculated using the time difference between both ends or the ratio of the energy-loss measurements at both ends. Since the position measurement is less precise than the one from, e.g., the GFIs, it is mainly used for cross checks.

The design with crossed paddles allows for a more precise time and energy measurement. A fragment passes both layers of the detector and, therefore, produces signals in four PMTs. For the TOF measurement, e.g., the time of the TFW is then calculated by the mean of all four times.

3.4 Trigger

For the R^3B/LAND setup, the Multi Branch System (MBS) is used as the DAQ system. It takes care of the data of all detector systems and stores them on disk in List Mode Data (lmd) files. As mentioned before, the data are taken on an event-by-event basis. However, at first it needs to be decided when a detector signal is called an event and when it is just random background not to be recorded. For the decision, several detectors in the setup provide logic signals to notify that they measured something above their detector specific threshold. These signals are called triggers. A combination of such triggers within a given time window sets a so-called Trigger BIT (Tbit) in the Trigger PATtern (Tpat). Several combinations of triggers can lead to multiple Tbits set in the Tpat of an event.

I distinguish between two different kind of Tbits. The first one is in coincidence with a trigger signal from the FRS monitor system correlating to the delivery of beam to the R^3B/LAND setup. This group of Tbits is called on-spill and marks the data of interest for the analysis of the reaction channels. The second group is in anti-coincidence with the trigger signal from the FRS monitor system. It is called off-spill and marks the data of interest for the calibration of detectors like LAND or XB. Data with these Tbits are either recorded in the time between the spills or before and after the beam time in dedicated calibration runs. In both cases, several detector systems need to provide a trigger signal in (anti-)coincidence for a Tbit to be set. Usually, the trigger signals are aligned timewise by delaying the signals from the different detectors. This way, the trigger signal from the start detector – with the condition POS!ROLU as explained later – is supposed to always come last and define the event time. An overview over on-spill and off-spill triggers used in this thesis can be found in Table 3.1 and 3.2, respectively.

In addition to the coincidence with the FRS trigger, on-spill Tbits are built by a combination of detector triggers with conditions on the time of the trigger signal. The *early pile-up* trigger is generated from POS. It requires a time delay to the previous and next event. The *late-trigger kill* signal is a pending trigger rejecting triggers within 150 ns after the *Min Bias* signal. This way late triggers are not taken into account.

After all possible Tbits are constructed this way, the event has to survive the dead-time veto of the DAQ. If an event is recorded, the DAQ needs around 400 μs to collect the data from all detectors and to store them on disk. During this interval, the DAQ is in dead time and no new event can be processed and stored. If an event with a valid Tpat arrives within the dead time, it is discarded.

As a last step, only a fraction of the events are selected for recording, depending on their Tbits. This step is called downscaling. It is done to reduce the dead time of the DAQ and the storage space. The goal is to record as many data as possible of the reactions of interest. In return only a small fraction of unreacted events are saved to disk. To do so, for each Tbit a downscaling factor n is defined, i.e., for each Tbit only every nth event is accepted, all other events are discarded. If

Table 3.1: On-spill trigger conditions for S393 used in this thesis. Triggers needed to build the corresponding Tbit are marked with x.

	Tbit	Early pile-up	Late-trigger kill	POS!ROLU	TFW	XB Sum	LAND Mult
Min Bias	1			x			
Fragment	2	x		x	x		
XB Sum	8	x	x	x	x	x	
Neutron	128	x		x	x		x

Table 3.2: Off-spill trigger conditions for S393 used in this thesis. Triggers needed to build the corresponding Tbit are marked with x, while triggers in anti-coincidence with this Tbit are marked with !.

	Tbit	POS!ROLU	XB Sum delayed	XB or delayed
XB Muon	256	!	x	
XB Gamma	2048	!		x

for an event several Tbit combinations are true, each one has to pass the downscaling process individually. As a result, the *Fragment* Tbit might not be set, although the *Neutron* Tbit is set and its trigger logic includes the *Fragment* Tbit. Reaction Tbits like *XB sum* or *Neutron* are usually not downscaled ($n = 1$), while the *Fragment* Tbit is heavily downscaled (e.g., $n = 128$). The downscaling factors are chosen during the experiment to optimize the data rate. Therefore, they vary between different settings and sometimes even between different runs of a setting.

Finally, if the original trigger survived the construction of a Tpat, the dead-time veto, and the downscaling, the event is saved.

For the analysis in this thesis, only a few Tbits are relevant. The most important on-spill Tbits are the *Fragment* and *XB Sum* Tbit. The former is used for the unreacted events since it is defined by a coincidence of a trigger from the start detector POS in anti-coincidence with ROLU (POS!ROLU) and a trigger from the TFW, the last detector in the fragment arm. For all events fulfilling this condition, the incoming and outgoing particles are detected and can be identified. Hence, it is the basis for all reaction Tbits. The latter is the reaction trigger for QFS reactions. In addition to the *Fragment* Tbit, a coincidence with the *XB Sum* trigger is required. For the *XB Sum* trigger the time signals of up to 16 crystals are combined and converted into a logical signal using a leading edge discriminator. These trigger signals are then combined with a logical OR to produce the *XB Sum* trigger. Due to the use of a leading edge discriminator small signals experience a walk effect, which leads to a late *XB Sum* trigger. In this case, it is possible that the POS!ROLU is not the last trigger and the timing of the event is no longer based on the POS time. Presumably, the *late-trigger kill* condition, which is only applied to the *XB Sum* Tbit, should remove these events. Unfortunately, this leads to a mismatch of the downscaling factors. By comparing events with only *XB Sum* Tbit set with those with *XB Sum* and *Fragment* Tbit set, one can reconstruct the downscaling factor for the *Fragment* Tbit. Doing so, the determined downscaling factor is around 15 % smaller than expected. This means that events which should have a *XB Sum* Tbit set were not recorded since the *XB Sum* Tbit was not set due to the walk

effect and the additional *Fragment* Tbit did not survive the downscaling process. This problem was already mentioned by Julian Kahlbow [Kah15].

For QFS reactions, the missing triggers due to the walk effect do not pose a problem since the protons from the reaction deposit a large amount of energy in the crystals. Hence, the trigger signal produced by the protons arrives before the POS trigger signal, which then defines the time of the event. On the contrary, in case of knockout reactions the emission of a proton and its detection in XB is not guaranteed. Therefore, small energy-loss entries from emitted γ rays or background radiation lead to a late trigger. For that reason, the inclusive cross sections for knockout reactions in Section 6.1 are calculated using only the *Fragment* Tbit to avoid problems with the triggers. However, the exclusive cross sections for the excited states can be calculated using the *XB Sum* Tbit since the γ rays from the deexcitation guarantee the deposition of enough energy in XB.

Additionally, a second reaction Tbit is listed in Table 3.1. Although the *Neutron* Tbit, which requires a coincidence of POS!ROLU, a trigger from the TFW, and a trigger from LAND, is not used for the analysis of the proton amplitudes and the reaction cross sections, it is used to clean plots for the identification of reaction products in Section 4.3. Problems with the *LAND Mult* trigger efficiency and the downscaling factors for the *Neutron* Tbit as mentioned, e.g., by Julian Kahlbow [Kah15], are therefore not relevant for my analysis. The same applies for the *Min Bias* Tbit which only requires a trigger from POS in anti-coincidence with ROLU. Both are mentioned here for the sake of completeness.

4 Analysis

This chapter describes the analysis of the experimental data in detail. At first it gives an overview over the *land02* framework used for conversion and calibration of the data, before it sheds light to individual analysis steps. The first two essential steps are the IDentification (ID) of the incoming and outgoing particles. They are necessary to select the reaction channels of interest. The next two sections focus on different aspects of the XB detector: the detection of γ rays and protons. The influence of addback algorithms on the spectra are analyzed. Angular distributions of the protons as well as their influence on the background of the γ-ray spectra are examined. The last section focuses on a slightly different aspect of the analysis and introduces different fit procedures with which the experimental and simulated data are compared.

The analysis is mainly done within the ROOT framework [BR97]. ROOT is written in C++ and, due to its object-orientation, a very versatile software compilation used for data analysis. A detailed documentation as well as various examples can be found on the corresponding webpage [ROO18]. All histograms and most of the analysis steps in this thesis are done with this tool.

The recorded data are divided into several runs belonging to one setting. All data with the focus on the same incoming particle are called a setting. For each setting different targets were used. Additionally, detector and trigger settings changed during the experiment. In all these cases a new run was taken. The runs are analyzed separately as long as statistics allow it.

In the experiment S393 data for $^{17}\mathrm{N} \rightarrow {}^{16}\mathrm{C}$ correspond to setting 3, while data for $^{19}\mathrm{N} \rightarrow {}^{18}\mathrm{C}$ correspond to setting 4 and data for $^{21}\mathrm{N} \rightarrow {}^{20}\mathrm{C}$ to setting 6. An overview of the runs used for the different settings is listed in Table A.1. Because the focus of this work lies on knockout and QFS reactions, I am only interested in runs with a carbon (C) or polyethylene (PE or CH_2) target. For calibration purposes, runs without any target, called empty target runs, are recorded and used in the analysis as well.

4.1 *land02* Framework

land02 is a software package developed by Håkan Johansson [Joh06]. It is used for converting data from lmd files for storing experimental data into ROOT files for further analysis. This process is called unpacking. For its parallelization the program GNU parallel [Tan11] was used. In addition to the conversion, *land02* provides algorithms for calibration tasks. Afterwards an additional unpacking step can be used to apply calibration parameters to the recorded data. To be able to follow the calibration procedure and check the results, the data are sorted into several levels which summarize all detectors in the setup up to a certain calibration step. The levels are briefly explained in the following. The flow and the involved calibration algorithms and parameters are depicted in Figure 4.1 for the example of the TFW. In general, all detectors record either deposited energies or times of occurrence. This information can then be combined to determine energy losses, charges, TOFs, positions, and masses of the involved particles.

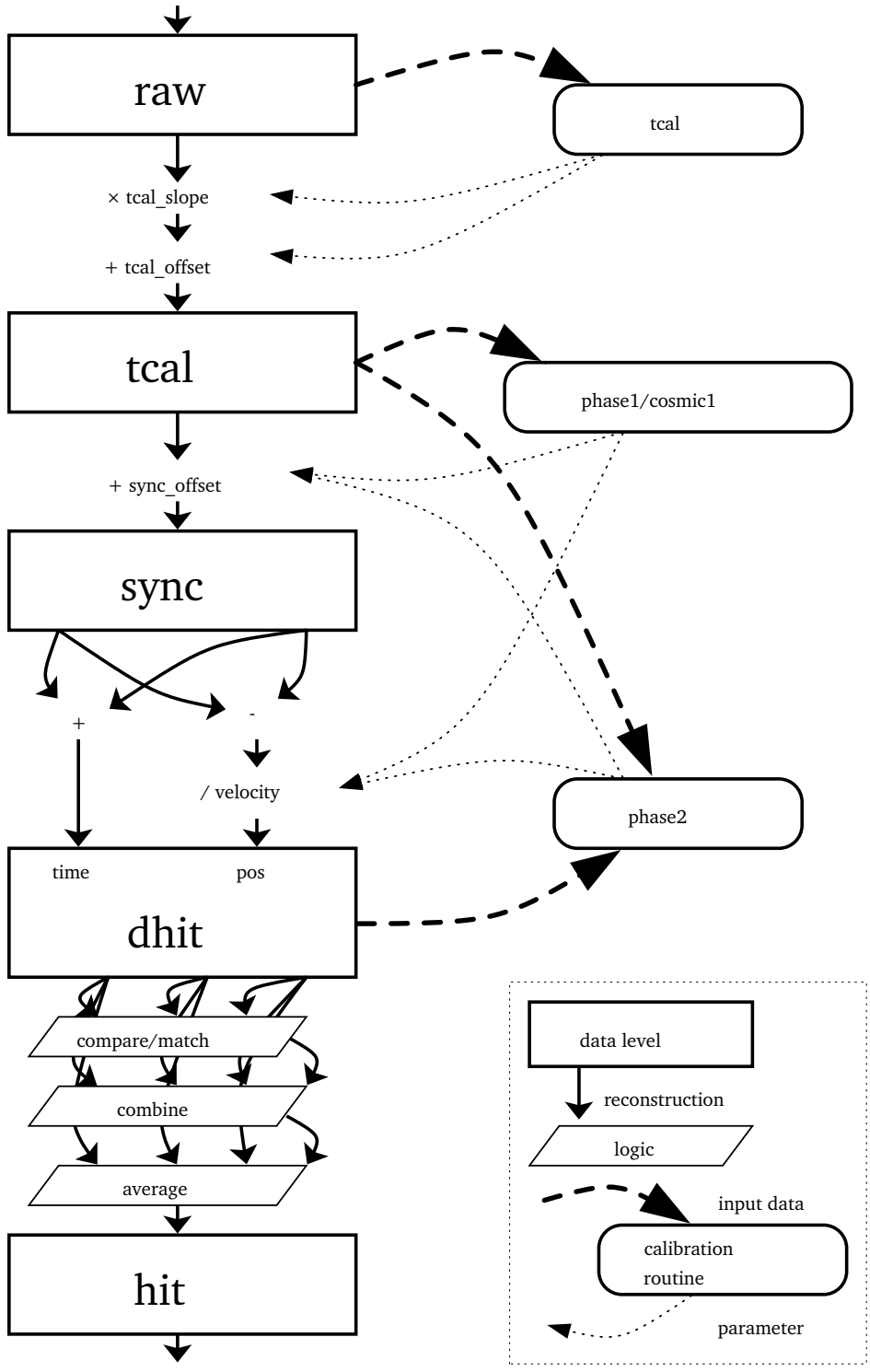

Figure 4.1: *land02* data levels and unpacking flow for the example of the TFW. The boxes on the left indicate the levels, while the rounded boxes on the right name the calibration algorithms used to determine the calibration parameters. The arrows indicate the usage of parameters between the different steps of the calibration process from the top to the bottom. The figure is taken from [Joh06].

RAW The lowest data level includes uncalibrated detector data as they were recorded. Energies are given in ADC/QDC channels and times in TDC channels. They are stored as integers.

TCAL The first calibration step is done. For the energy entries baseline offsets are subtracted but no conversion to physical units has taken place. Times are converted into ns using an offset and slope. The calibration parameters were determined for each detector channel using the `clock` and `tcal` routine from the *land02* package. The data are stored with floating point precision from now on.

SYNC Within this level the energy and time calibration is completed. This includes the synchronization of all channels of one detector. For time measurements, two different offset are applied to match them within one subsystem (e.g., a scintillator bar) and detector wide. The same is done for energy entries with two gain factors, one for matching the energies within a subsystem and one within the whole detector. The calibration parameters are determined with the `cosmic1` and `phase1` routine. Times are given in ns, energies in MeV.

DHIT On this level the time and energy information from the previous level is combined into information about the hit for each detector. This includes time, energy deposition, and position. Positions, e.g., for the PSP and the GFIs, are given in detector intrinsic coordinates u and v.

HIT The information for each detector is no longer given in a detector specific but in a global coordinate system with its center in the center of each detector. A detector specific transformation (from uv) to xy positions is applied. The xy position is given in cm. The position of the detectors within the setup is not yet taken into account.

TRACK The combination of several detectors lead to the reconstruction of particle trajectories. This step needs information about the geometry of the setup. It is available for the incoming beam and neutrons in LAND. In this thesis, TRACK level data are only used for the incoming beam for which information from S8, POS, and PSP are combined to determine the proton number Z, the mass A, and the velocity β of the incoming particles.

The calibration for the analysis in this thesis was mainly done by other PhD students, namely Christoph Caesar, Marcel Heine, Matthias Holl, Alina Movsesyan, Paloma Díaz Fernández, and Ronja Thies, who all started their analysis earlier. Therefore, the data shown in this thesis is in SYNC, HIT, or TRACK level. A good overview over the general calibration procedures can be found in [Pas08, Ros09]. Further information, hands on help, and documentation can be found on the *land02* webpage [Pla18a].

4.2 Incoming ID

The first step in the selection of the reaction channel of interest is the determination of the incoming particles. For this purpose, information on TRACK level can be unpacked with *land02* as explained in the previous section. To identify the incoming particles, their mass A and proton number Z need to be determined. The energy loss in the PSP before the target is proportional to the square of the charge state Q of the ions according to the well known Bethe formula, c.f. Equation 3.2. With the ions delivered from the FRS being fully stripped, the proton number Z and the charge state Q are equal and can be easily measured. The mass A, or the mass-over-charge ratio A/Z, can be determined with the help of the track of the particle through the FRS dipole magnets as described by Equation 3.1. The velocity is measured via the TOF between the

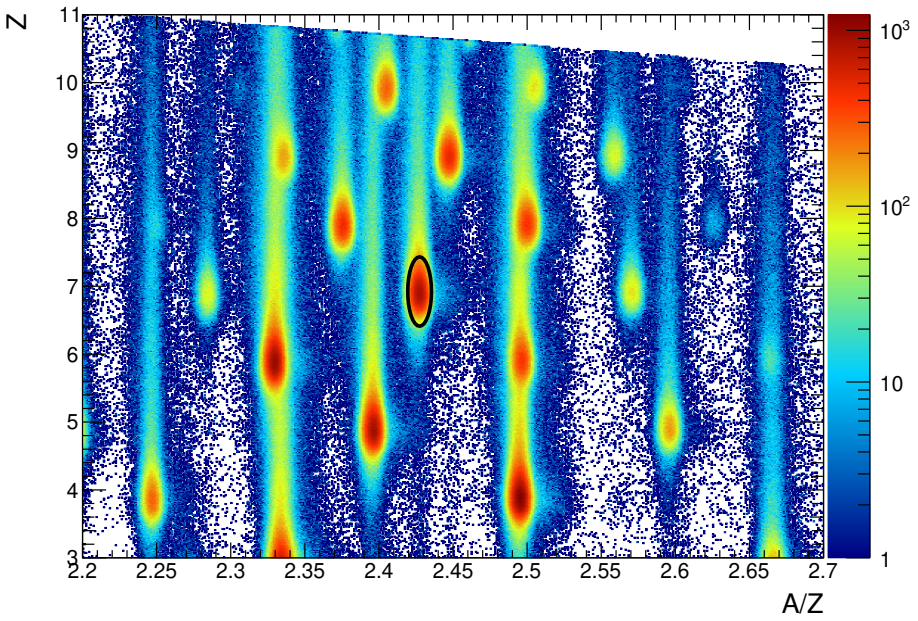

Figure 4.2: Incoming ID for setting 3 and the CH_2 target. The applied cut in A/Z and Z on incoming ^{17}N is shown in black. This plot is drawn for the *Min Bias* Tbit.

S8 detector in the FRS setup and the POS detector at the entrance of Cave C. The nominal $B\rho$ value of the FRS is known for the different settings. The calibration of the incoming ID was done by Marcel Heine and is described in [Hei15].

The result of this first analysis step can be seen in Figure 4.2 for setting 3 and the CH_2 target. It shows the incoming cocktail beam. The isotope of interest ^{17}N is marked with a black ellipse. The semi-axes and the position of the ellipse are determined with fits of a normal distribution to the charge and the A/Z spectrum separately. The means of the distributions are used as the center of the ellipse, while twice the standard deviations are used for the semi-axes. For the following analysis, a cut is applied to the data and only those events are analyzed whose charge and mass lie within the ellipse. As long as this cut is not contaminated by other isotopes it does not influence the result of the analysis but only increases or decreases the available statistics. Incoming ID plots for the other two settings (setting 4 and 6) and the various targets (CH_2, C, and empty target) are depicted in Figure A.1, A.5, and A.8.

4.3 Outgoing ID

The next step is the ID of the reaction products, i.e., the outgoing particles. This is done within two steps: The first step is the determination of the charge Q and proton number Z, respectively, with energy-loss measurements in the SSDs after the target and the TFW at the end of the fragment arm. Afterwards, this charge information is used together with the flight path through the magnetic field of ALADIN to reconstruct the mass of the outgoing isotopes. Both steps will now be explained in detail.

4.3.1 Charge ID

To determine the charge Q of the outgoing particles, the energy deposition in three detectors is available. Two SSDs are placed behind the target. Additionally, the TFW at the end of the fragment arm measures the energy loss.

For the TFW, the calibration routines `clock`, `tcal`, and `phase1` are available within the *land02* package [Pla18a]. On the lowest level, the calibration includes the subtraction of the baseline for the energy measurement and a gain and offset to convert channel numbers into times in ns for the time measurement for each PMT. Within the next step, gain factors are applied to match the energy and offsets to match the times of the two PMTs of one paddle. Additional gain factors are then used to match the paddles with each other to finally get one time, position, and energy-loss measurement for the whole detector. A detailed description of the procedure can be found in [Ros09]. The calibration used in this work was done by Christoph Caesar [Cae15]. I will use his calibration parameters without further explanation of the calibration procedure.

For the SSDs, the first step of the calibration is the same as for the TFW. The *land02* routine `clock` is used to determine the baseline and the width σ of the noise. After the subtraction of the baseline, energy entries in neighboring strips are sorted into clusters. The energy and the position of these clusters are then used to determine the energy loss and the position of the transversing particles. This procedure is explained by Matthias Holl [Hol14] in detail. He describes that the charge collection varies with the position η within one strip. This leads to a variation of the measured energy depending on η. Furthermore, hits seem to occur more often close to the border of a strip than in the center. This effect needs to be corrected for to calculate the correct cluster energy as well as the correct cluster position. Additionally, Matthias Holl describes how to reconstruct the cluster energy, when some strips in a cluster – especially in the center – are broken and do not provide an energy signal.

During the analysis, it became clear that the existing calibration was not sufficient. The baseline and noise information provided by Matthias Holl is used, but the calibration parameters for the η correction seem to be run dependent. Therefore, the η correction was redone for the analyzed data using a dedicated script written by Matthias Holl. The first step of this procedure is the η-position correction. Without the correction, the probability for a reconstructed position is higher at the edges of each strip, i.e., $\eta = 0$ and $\eta = 1$. After the correction the probability is the same for all η. An intermediate step corrects for the different gains of the strips by fitting normal distributions to the energy loss depending on the position. The resulting correction factor is the inverse of the mean of the distribution. In the last step, the η-energy calibration, the energy loss is plotted over the position within a strip η. Again a normal distribution is fitted to the energy loss and the inverse of its mean is used as the correction factor. The effect of the whole correction is depicted in Figure 4.3, in which the energy loss is plotted over the position for the k-side of SSD3 before and after the η correction exemplary for run 427 of setting 4.

After the calibration of the SSDs is done, a charge cut can be applied to the data. The k-side of SSD4 has a lot of broken strips, which makes it a bad choice for the charge cut. Furthermore, the s-side of SSD3 and SSD4 have a bad energy resolution even after the η correction. Therefore, only the energy loss measured with the k-side of SSD3 and the TFW are used to determine the charge of the outgoing fragments. An example together with the applied cuts can be seen in

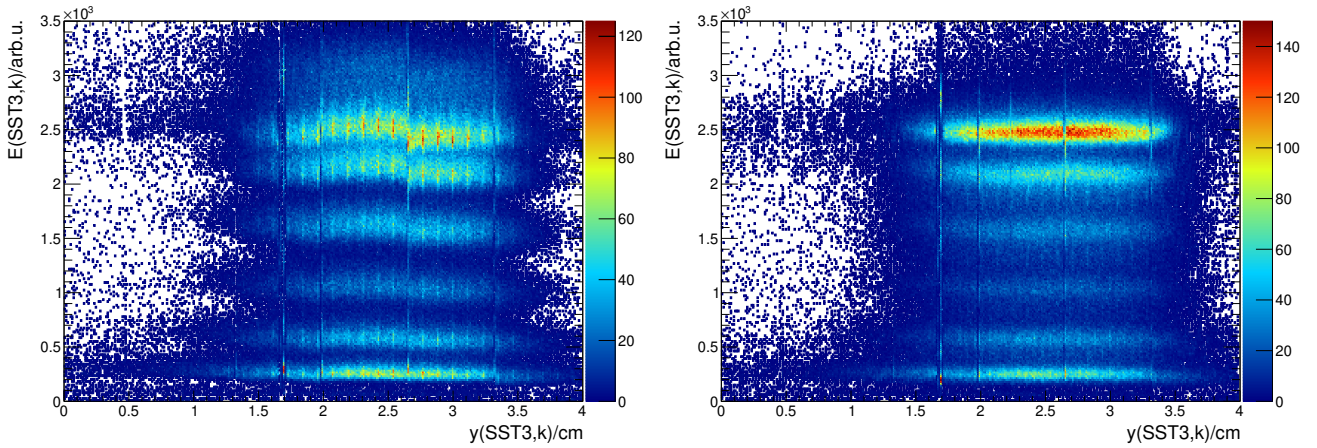

Figure 4.3: Effect of the η correction on the outgoing charge measurement with the SSDs. The cluster energy over the cluster position is shown for SSD3, k-side before (left) and after (right) the correction. Before the correction one can see the boarder of the strips due to an accumulation of events. This is corrected for in the first step, the position correction. The last step, the energy correction, eliminates the position dependency of the measured energy and improves the energy resolution. The position is given in a detector specific coordinate system. This plot is drawn for the *XB Sum* Tbit to enhance the visibility of the reaction products.

Figure 4.4 for setting 3 and the CH_2 target. The *LAND* Tbit is chosen to enhance the visibility of the reaction products and to suppress the unreacted beam. On the diagonal, all reaction products down to helium can be seen with nitrogen on the top right. The straight line to the bottom for $E_{\mathrm{SSD3}} = 2500\,\mathrm{arb.u.}$ corresponds to break-up of the unreacted beam during the flight between SSD3 and the TFW.

For the following analysis, two cuts are needed. First of all, the particles of interest, namely carbon isotopes, need to be selected. This is done with an asymmetric elliptic cut with a different semi-axis on the right than on the left side of the ellipse. Usually one would use an ordinary ellipse to cut on the charge of interest, but due to the contamination from the break-up during the flight, it is not possible to use a symmetric cut without either loosing statistics or contaminating the mass spectrum. Therefore, the semi-axis in the y direction corresponds to $2 \cdot \sigma_{E,\mathrm{TFW}}$, while for the x direction, the semi-axis to the left corresponds to $3.5 \cdot \sigma_{E,\mathrm{SSD3}}$ and the semi-axis to the right either to $2 \cdot \sigma_{E,\mathrm{SSD3}}$ or the value that separates the carbon blob from the break-up residue. As before, the standard deviation is determined with a fit of a normal distribution to the energy spectrum of the TFW and SSD3 separately.

Additionally, the number of unreacted particles is used as the number of incoming particles for the calculation of the reaction cross sections. This has the advantage that the efficiencies for detecting the particles in the fragment arm are the same for reaction products and unreacted particles and, therefore, cancel out in the calculation of the cross sections. The assumption is valid when the reaction cross section is small and the intensity loss in the target is linear. A detailed calculation why this approximation is valid is given by Julian Kahlbow [Kah15]. To determine the number of unreacted particles, a cut on the outgoing nitrogen isotopes is needed. As one can see in Figure 4.4, the energy-loss measurement for nitrogen displays no asymmetric smearing to one direction. Therefore, a symmetric cut with $2 \cdot \sigma_{E,\mathrm{SSD3}}$ and $2 \cdot \sigma_{E,\mathrm{TFW}}$ for the semi-axes is applied to the data, which is depicted in Figure 4.4 as well. The value of $2 \cdot \sigma$, which

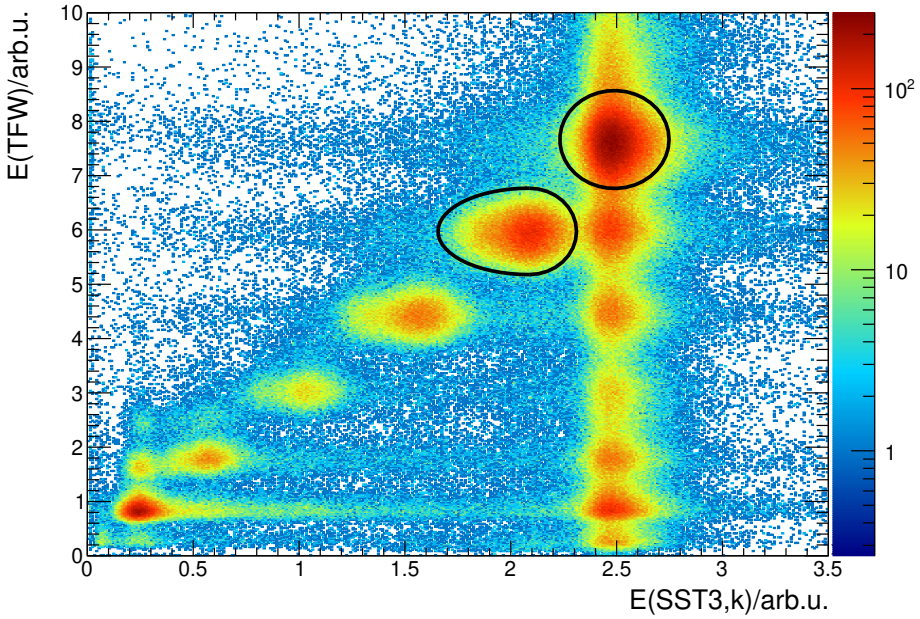

Figure 4.4: Outgoing charge for setting 3 and the CH_2 target. Two cuts are marked with black ellipses. The one in the top right is a cut on outgoing $Z = 7$ (N), while the asymmetric cut on $Z = 6$ (C) contains the reaction products of interest. This plot is drawn for the *LAND* Tbit to enhance the visibility of the reaction products.

is again determined with a fit of normal distributions to the energy spectra, is chosen such that the number of particles taken into account is maximized while reducing the contamination, e.g., from reactions within the fragment arm, to a minimum.

Plots including cuts for other setting-target combinations are depicted in Figure A.2, A.6, and A.9. For consistency, the cuts are chosen the same way as explained above for setting 3 and the CH_2 target.

4.3.2 Mass ID

To finally identify the outgoing isotopes, the fragment mass needs to be determined. For this purpose *Ralf's tracker*, a software package developed by Ralf Plag, was used. The source code and a detailed How-To can be found on the corresponding webpage [Pla18b]. It uses position and time information from the various detectors in the setup to determine the flight path and the velocity of the particles. This is done by matching the position and time information with the magnetic field of ALADIN according to Equation 3.1 for a given charge Z determining the mass A within this process. In principle, the *tracker* can be used to calculate both incoming and outgoing trajectories, but in this work, it is only used for the outgoing particles. The incoming particles and their trajectories are already identified using *land02*.

To be able to calculate the flight path after the target, the *tracker* needs either two positions before and one behind ALADIN (forward tracking, used in this work) or one position before and two positions behind ALADIN (backward tracking) to determine the angle and position with which the particle enters the magnetic field. In the setup, three positions before and three positions behind ALADIN are available. The position on the target is provided by *land02* using information from detectors before the target. Additionally, SSD3 and SSD4 between the target

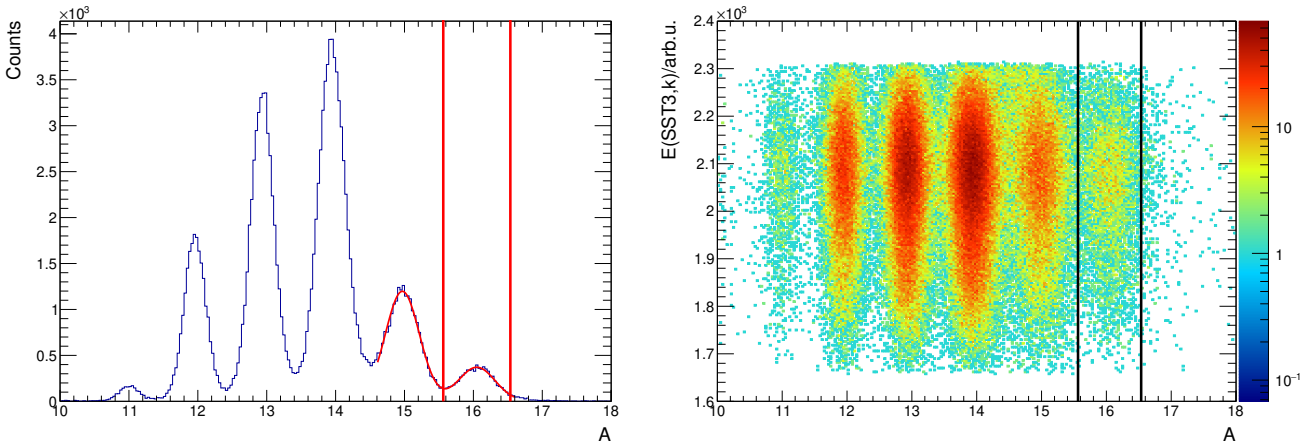

Figure 4.5: Outgoing mass for setting 3 and the CH_2 target with a cut on $Z = 6$ (C). The left picture shows the tracked mass with the applied cut on outgoing $A = 16$ in red, while the right picture shows the charge measured with the SSD3 over the tracked mass with the same cut in black. The plot is drawn without a trigger condition.

and the magnet provide position information in the x and y direction. After the target, two GFIs are placed in the fragment arm. Both of them provide an x position but no y position. At the end of the fragment arm, the TFW provides x and y position together with a time measurement used to determine the TOF between POS and the TFW. This time is used to determine the velocity of the outgoing fragments taking into account the energy loss in the different detectors and the target. Due to the orientation of the dipole field of ALADIN, the y position is only used for consistency checks and not for the mass determination. The missing y positions of the GFIs is therefore no problem and the y position of the TFW is used instead. As mentioned before, the calibration of the TFW was done by Christoph Caesar, while the calibration of the GFIs was done by Alina Movsesyan and is described for a different experiment in [Mov13]. The positions of the detectors within the setup are adopted from Paloma Díaz Fernández, while the time calibration of the *tracker* itself is done following the instructions on the webpage [Pla18b].

The result of the tracking procedure is depicted in Figure 4.5 for setting 3 and the CH_2 target. The mass spectrum on the left shows a small peak at the mass of interest, $A = 16$, while most of the carbon isotopes lost additional neutrons during the reaction. The even-even nucleus ^{14}C is hereby the nucleus with the highest yield. Again, a cut needs to be applied to the data to select the nucleus of interest. In this case, two normal distributions are fitted simultaneously to the peaks at $A = 15$ and $A = 16$. The point at which the two distributions intersect is used as the minimum accepted mass, while the same distance to the mean of the normal distribution at $A = 16$ is used as the maximum accepted mass. As one can see in Figure A.10, in case of setting 6 the number of tracked events is too small to allow for a fit. Therefore, $A = 19.5$ is used as minimum and $A = 20.5$ as maximum accepted mass.

The mass spectra of all isotopes of interest are clean enough and the peaks are clearly separated such that a two or even three dimensional cut on the outgoing mass and charge is not necessary. Together with the small statistics for setting 6, a two dimensional cut is omitted to treat all settings in a consistent way and to avoid loss of tracked events. The energy loss in the SSD3 plotted over the mass in Figure 4.5 on the right shows that this decision is valid and that the

cut on the mass is reasonable. Additional plots for all available setting-target combinations are depicted in Figure A.3, A.7, and A.10.

4.4 γ-ray Spectrum

One of the goals of this thesis is the comparison of the production of the outgoing isotopes in their $0^+_{g.s.}$ ground state, their first excited 2^+_1 state, and in case of ^{16}C and ^{18}C additional higher lying states. To distinguish them, the γ ray(s) from the deexcitation process are measured with XB. Before the γ-ray spectra can be analyzed, several analysis steps are necessary, which are described in the following. Since the γ rays are emitted by particles moving with $v \approx 0.73\,c$, the γ rays are boosted in forward direction and their energies need to be Doppler corrected. Additionally, their higher energies in the laboratory system favor the interaction with the XB crystals via the Compton instead of the photoelectric effect. To reconstruct the energy of a γ ray, energy entries from several crystals close to each other are summed up into a cluster. This process is called addback and several algorithms are introduced and compared. Furthermore, especially protons produced in QFS reactions are detected with XB as well. Although they are treated separately as explained in Section 4.5, they introduce background to the γ-ray spectra.

The calibration of XB consists of three parts: the energy calibration of the γ-ray and the proton readout of every single crystal and the synchronization of the time information of all crystals among each other. First of all, the calibration of the γ-ray branch is done with dedicated calibration runs with γ-ray sources. For the experimental campaign S393 (and S389), ^{22}Na, ^{56}Co, ^{60}Co, and ^{88}Y sources were available with energies up to 3.3 MeV. The lack of high energy calibration sources results in a systematic uncertainty for high energy entries. Next, the proton branch is calibrated using muons from the cosmic background radiation. They are measured off-spill during physics runs and in dedicated cosmic runs during the whole experiment. The energies of the transversing muons are then compared to simulations. Finally, the time synchronization is done using runs with a source emitting two coincident γ rays. For this calibration step, events in which the full energy of both γ rays was deposited in exactly one crystal each are selected and the time difference between these crystals is saved. With time differences between each combination of crystals, the time offset for each crystal can be determined. In this case only the γ-ray readout is used for synchronization. The resulting calibration parameters are then applied to both, the γ-ray and the proton readout. The `gamma2` routine provided by *land02* helps with the calibration using muon events and the time calibration. The calibration used in this work was done by Ronja Thies and is described in detail in [Thi11].

During the energy calibration it was observed that the energy resolution of several crystals is too bad to calibrate them, since the photopeaks from the source measurements merge or could not be identified at all. Those detectors are excluded from the analysis completely. Furthermore, crystals whose energy resolution is bad and which have a big uncertainty in their energy calibration are used during the addback procedure but are excluded from the γ-ray spectrum if they are the dominating crystal, i.e., the cluster center.

After the calibration is done, an event contains a list of crystals with time information in ns and energy information in MeV. However, not all crystals have a valid time and energy entry. On one hand, the energy deposition is not recorded if it is below a certain threshold set in the electronic readout. On the other hand, if the deposited energy is above the maximum range of the QDC, the energy is set to *inf*. Due to the Doppler boost the expected energies in forward and

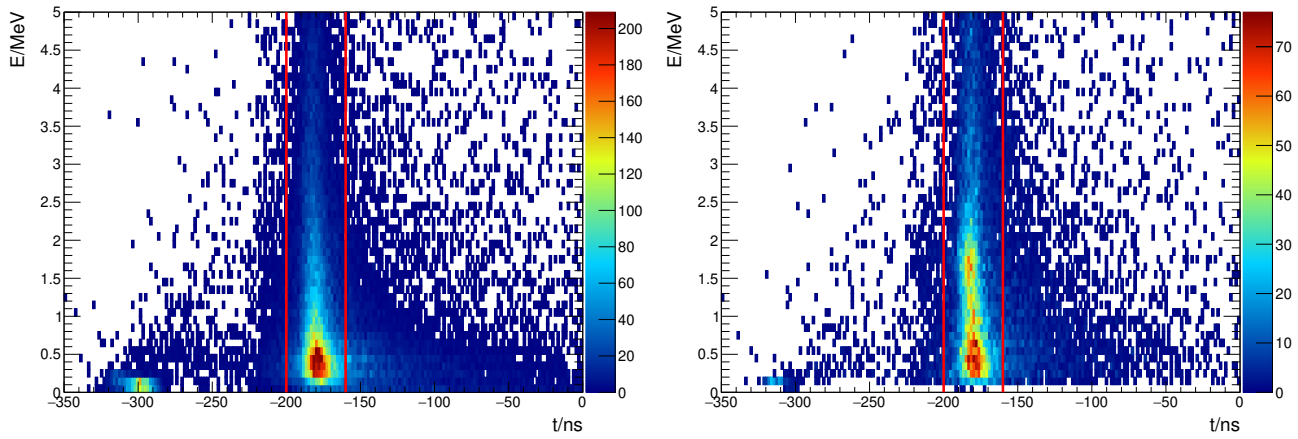

Figure 4.6: XB γ-ray energy over detector time for setting 3 and the CH_2 target. For the calibrated energy (left) the majority of the detected γ-ray entries has a time around −180 ns. The energy after NN addback and Doppler correction (right) shows a similar time dependency. For both cases a time cut of $-200\,\text{ns} < t < -160\,\text{ns}$ is applied. It is depicted in red. This plot is drawn for the *XB Sum* Tbit.

backward directions in the laboratory frame vary a lot, resulting in different thresholds for each crystal. Whereas these thresholds are included in the experimental data by default, they need to be applied explicitly to the simulation introduced in Chapter 5.

Examining the time dependency of the energy of the γ-ray branch shown in Figure 4.6, one realizes that most of the crystals detect a γ ray around $t = -180\,\text{ns}$. These energy entries correspond to prompt γ rays from the outgoing fragment, the target, or interactions of reaction products such as protons with the crystals. Entries with $t \gtrsim -160\,\text{ns}$ or $t \lesssim -200\,\text{ns}$ are mainly background. Since the time of each crystal is read out using a CFD, no walk effect for small energies is expected. To clean the γ-ray spectra from this background, a time cut of $-200\,\text{ns} < t < -160\,\text{ns}$ is applied to all experimental γ-ray spectra in this thesis.

Finally, after applying an addback algorithm and the Doppler correction, the resulting γ-ray spectra can be compared to simulated spectra to identify the contribution from the different excited states. The simulations done for this work are described in detail in Chapter 5. Since both the experimental and the simulated spectra include the XB efficiency to detect γ rays, I do not have to include it explicitly. However, the consistency of the γ-ray efficiencies is verified in Section 5.2. The results of the fits are shown and discussed in Chapter 6.

4.4.1 Doppler Correction

The particle emitting the γ ray travels with $v \approx 0.73\,\text{c}$. Therefore, the energy of the γ ray gets boosted according to the relativistic Doppler effect. The energy XB detects depends on the angle between the emitting particle and the detecting crystal and the energy of the emitted γ ray. The energy of the γ ray in the Center-of-Mass (c.m.) system of the nucleus E_{cm} can be deduced from the detected energy E_{lab} and the detection angle θ with the following equation

$$E_{\text{cm}} = E_{\text{lab}} \cdot \gamma \cdot (1 - \beta \cos\theta)\,. \tag{4.1}$$

This so-called Doppler correction is applied to all γ-ray spectra except source measurements in this thesis. It is in principle only valid for γ rays emitted by the outgoing nucleus. Thus, the use

on background γ-rays can lead to a slightly distorted background spectrum compared to a resting source. Additionally, the angle θ can only be determined with a precision of $\Delta\theta \approx \pm 7°$, the opening angle of a single XB crystal. The result is a broadening of the photopeak, which is called Doppler broadening and behaves like an additional resolution. Usually, the angle corresponding to the middle of the crystal is used for the correction. However, with the γ rays being boosted in forward direction, the distribution in a crystal is asymmetric. This leads to a slightly asymmetric shape of the photopeak with more entries having higher energies because more γ rays are corrected with too large angles. Since this systematic error exists for the experimental as well as for the simulated data, I do not need to correct for it.

Furthermore, I assume that the γ ray is emitted from a particle in the middle of the target moving in the z direction. Thus, the position of the incoming beam on the target and the direction of the fragment is neglected. Because of the relatively small beam spot with a radius of 0.5 cm compared to the inner radius of XB of 25 cm, the error of the angle due to the neglected position on the target is small. Again, the simulation includes the beam spot and its size on the target and, therefore, introduces the same uncertainties. The approximation of the fragment moving in the z direction is no problem either. The fragment displays a scattering angle of $< 0.8°$ in the experimental data, while the event generator for the simulation introduced in Section 5.3 generates fragments with a scattering angle of $< 0.5°$. Besides the small value of the scattering angle, this effect cancels out for a sufficient number of events due to the rotational symmetry around the z axis. In comparison with the resolution stemming from the opening angle of the crystals, both contributions are negligible.

4.4.2 XB Addback

Depending on their energy, the γ rays do not deposit the whole energy in a single crystal via the photoelectric effect but are Compton scattered to neighboring crystals. To correct for this effect and not lose these events, an addback routine is applied. The general idea is to sum up the energies which belong to one γ ray. The crystals which belong together are called a cluster. The difficulty is to determine which crystals belong to a cluster and to avoid adding energies from background. In this work, three different addback algorithms are tested.

- The Next-Neighbor (NN) algorithm looks for the highest energy deposition in XB. It adds the energy of all neighboring crystals but only if their energy is above a minimum energy threshold to reduce background contamination. In case of simulated data, an additional maximum energy threshold is introduced to avoid the mixing of energy depositions from protons and γ rays. This is not necessary for experimental data. The neighboring crystals are then marked as used and their energy is set to 0, respectively. After all neighbors are added, the cluster energy is saved and the routine starts from the beginning with the remaining energy entries.
- The Next-to-Next-Neighbor (NNN) algorithm works similar to the NN algorithm, but it additionally adds the energies of a second ring of crystals around the cluster center.
- The bunch algorithm uses a more flexible approach. Like the other two algorithms, it chooses the crystal with the highest energy deposition as the cluster center. It then checks all neighbors for a valid energy entry. An energy entry is valid if it lies within the crystal specific thresholds. In case of valid energy entries, it adds their energy to the cluster

energy and marks them as used. Additionally, the algorithm checks the neighbors of these crystals in the next step. It continues until the maximum number of steps is reached or no neighboring crystal has a valid energy entry.

An example of which crystals are added to a cluster for the different addback algorithms is depicted in Figure 4.7. It shows a cluster center with six neighbors. Some of the crystals in its vicinity have an energy entry above the threshold. Depending on which addback algorithm is used, different crystals are sorted to one cluster and the cluster energy changes.

In all three cases, I assume that the first interaction with the detector is the one with the highest energy deposition. The crystal with the highest energy entry is therefore used as cluster center and determines the angle θ used for the Doppler correction. Another similarity of all three algorithms is the use of thresholds below and above which the energy of a crystal is not taken into account. The thresholds used in this analysis were determined by Matthias Holl and used in his analysis [Hol14]. They are mainly relevant for simulated data for which all energy values are saved, while for experimental data thresholds in the electronic readout prohibits the recording of small energy entries. Because of the Doppler boost, different energies are expected in backward and forward directions. The range of each readout is chosen accordingly. Therefore, the lower thresholds of the single crystals lie between 0.08 MeV and 0.6 MeV. Their effect is visible in all γ-ray spectra, but due to the different cuts for different crystals and the Doppler correction, it is not visible as a hard cut at low energies but smears out. The second threshold is used to distinguish energy entries from γ rays and protons. For the experimental data, events with valid entries are treated as γ rays, while overflow (*inf*) entries are identified as protons. For the simulation, the crystal specific thresholds are needed to reproduce this. These thresholds vary between 3 MeV for the most backward crystals and 35.3 MeV for the most forward crystals.

The answer to the question which addback gives the best result depends on the physics case. On one hand, γ rays with higher energies are more likely to interact with the crystals via Compton scattering or pair production. Therefore, NN addback might not be able to collect the whole energy of a γ ray. On the other hand, for events with several γ rays at once, the bunch addback might sum up energies which originally belonged to different γ rays. To determine the best addback algorithm for the physics cases in this thesis, simulated spectra are examined in detail. The analysis is done with simulated instead of experimental data because of the low statistics of the experimental data set. Additionally, simulated data allow for cross checks with the properties of the event which are unknown for experimental data.

A similar comparison has been done by Simon Lindberg [Lin13]. In his thesis he simulates the response of XB to monoenergetic γ rays, protons, and neutrons. With a series of simulations of γ rays with energies between 1 MeV and 30 MeV and protons and neutrons with energies between 1 MeV and 300 MeV, he tests the general behavior of XB. In the following, I will shortly summarize his work and highlight his results for γ rays with an energy of 2 MeV. For each emitted γ ray on average 1.6 crystals have an energy signal. The number of events in which two hit crystals are separated by at least one crystal are 1.1 % for γ rays but up to 7.3 % for protons with an energy of 300 MeV. Furthermore, in only 81.8 % of the γ-ray events the whole energy is deposited in XB. Simon Lindberg also verifies whether the first interaction takes place in the crystal with the highest energy deposition: Depending on the position, this assumption is true for γ rays in 98.4 % of the events for hits in the middle of a crystal, down to 66.7 % for hits in the corners. In addition, he reviews the three addback algorithms introduced above. Simulations with two coincident γ rays emitted in random directions show that the NN and the

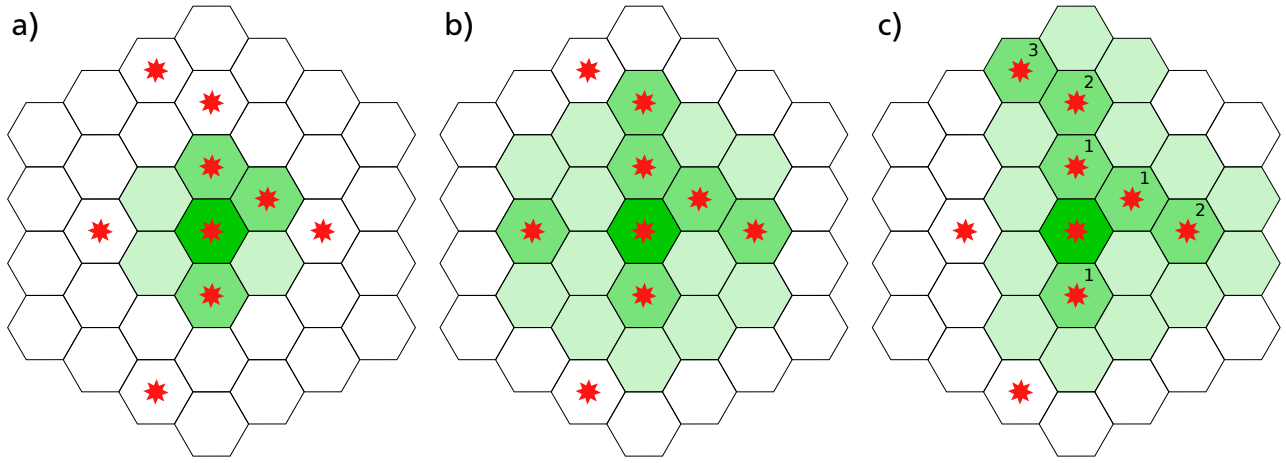

Figure 4.7: Example for the three different addback algorithms: The red stars mark crystals with an energy deposition above the minimum threshold. The dark green crystal in the middle is the center of the cluster. It belongs to the entry with the highest energy which has not yet been processed. The energy of the medium green crystals are added to the cluster energy. All light green crystals are checked during the addback but not added to the cluster energy due to the threshold. a) The NN addback sums only the direct neighbors of the cluster center. It might miss energy depositions from sequential Compton scattering. b) The NNN addback adds up the two rings around the cluster center. c) The bunch addback follows the line of connected crystals with an energy deposition. In this example the maximum number of steps is set to 3. The small numbers indicate in which step the crystals are included in the cluster.

bunch addback work similarly well over a wide range of energies, but the bunch addback is to be favored for energies above 10 MeV. The comparison of simulations with different angles between the two γ rays shows that the NN addback performs best for an angle up to 40°, while the NNN addback is better suited for angles between 60° and 90°. In the range between 40° and 60° the NN and the bunch addback give similar results. However, his simulations do neither include the detector resolution nor any background contribution.

The examined spectra stem from simulations of ^{17}N(p,2p)^{16}C reactions. The simulations include the ^{16}C fragment, the two protons from the QFS reaction, and γ rays from the excited states. The different excited states are simulated in separate simulations and analyzed separately. Details about the simulation can be found in Section 5.3.1. A cut on the number of detected protons (#p = 2) is applied and the spectra are Doppler corrected. Energy entries from clusters for which the center crystal was found to have a bad energy resolution are not used for the spectra.

Figure 4.8 a) illustrates the difference between the three addback algorithms. It shows the γ-ray spectrum of the 4^+ excited state, which decays via a cascade of two γ rays with an energy of $E_1 = 1.762\,\text{MeV}$ and $E_2 = 2.374\,\text{MeV}$. The third peak corresponds to the sum energy of $E = E_1 + E_2 = 4.136\,\text{MeV}$. For most of the bins in the histogram the number of entries is the highest for NN and the lowest for NNN addback with bunch addback in between. This effect is most pronounced for energies below the photopeaks, which come from Compton scattering or

Table 4.1: Number of events for which the two highest energy entries in XB are sorted to the same cluster. The estimation is done with a simulation of the ^{17}N(p,2p)^{16}C reaction including the ^{16}C fragment, two protons, and the γ ray from the deexcitation of the 4^+ excited state. Crystals identified as part of a proton cluster are excluded.

Addback	NN	Bunch, 2 step	Bunch, 3 step	Bunch, 5 step	Bunch, 10 step	NNN
% of events	0.185	0.216	0.224	0.231	0.232	0.284

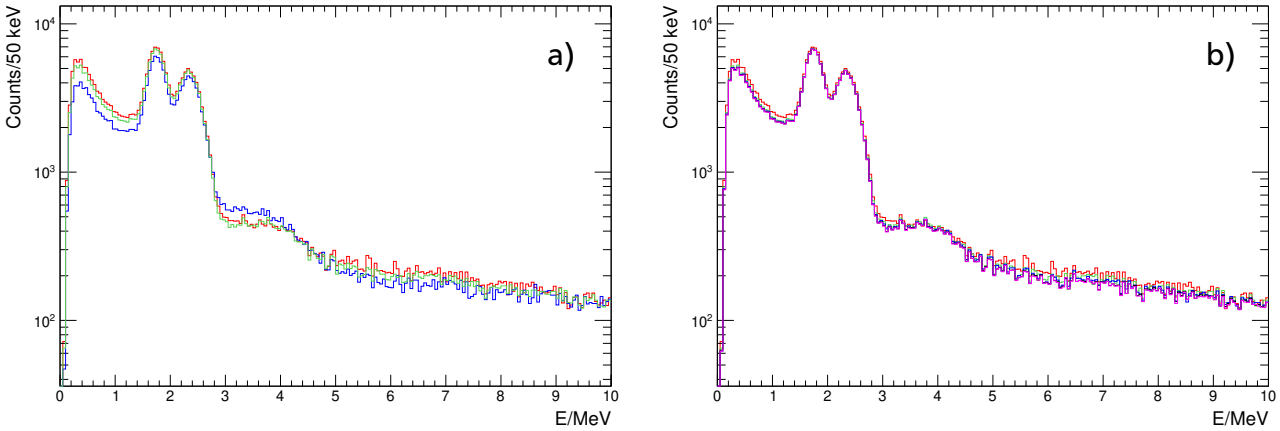

Figure 4.8: Comparison of addback algorithms for simulated data of ^{16}C: a) γ-ray spectrum of the 4^+ excited state for NN adbback (red), NNN addback (blue), and bunch addback (green) with a maximum number of 2 steps. b) γ-ray spectrum of the 4^+ excited state for bunch addback with a maximum number of steps of 1 (red), 2 (green), 3 (blue), 5 (black), and 10 (pink).

from background events. While the summation of all Compton scattered γ rays is the goal of the addback procedure, the summation of background needs to be avoided. On the other hand, the entries in the sum peak increase for NNN addback because the summation of two rings will form one cluster instead of two clusters for sequential γ rays when they are detected close to each other. Therefore, the photopeak to sum peak ratio decreases. The number of events in which the two highest energy depositions, which are interpreted as different γ rays, are sorted into one cluster can be found in Table 4.1.

For energies higher than 15 MeV, the picture changes and the number of entries per bin is smaller for NN addback than for NNN or bunch addback. This behavior is expected because the NNN and the bunch addback add up more crystals and, therefore, increase the cluster energy. The total number of clusters decreases for the same reason comparing NN to NNN addback with bunch addback in between. As a conclusion, the NNN addback should not be used in this case mainly because of the inefficient separation of two γ rays in close crystals.

Additionally, I compared the spectra for a different number of steps for the bunch addback. While the number of steps set to 1 is identical to NN addback, there is no equivalent to NNN addback. Figure 4.8 b) shows the energy spectrum for different numbers of maximum steps. Note that not all clusters are built with the maximum number of steps. Most of the clusters are completed in a 0 step (single crystal without any energy deposition in neighbors) or 1 step

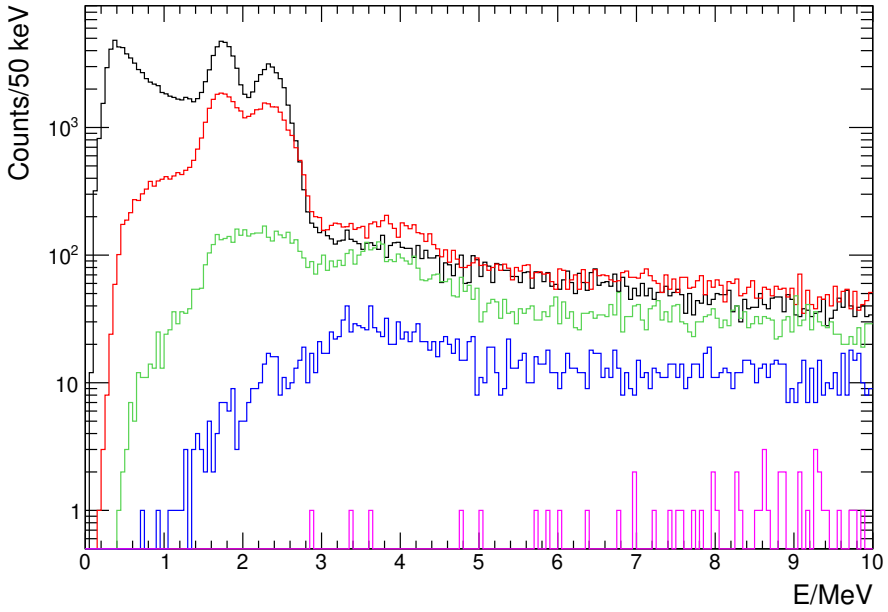

Figure 4.9: Comparison of the number of steps for the bunch addback for a simulation of the 4^+ state of ^{16}C. The maximum number of steps is set to 20. Events with the same number of steps are saved in the same spectrum. Spectra for events with 0 (black), 1 (red), 2 (green), 3 (blue), and 6 (pink) steps are shown.

process. While a significant change from 1 step to 2 steps is visible, especially for energies below 1.5 MeV, the differences between the spectra become more and more negligible for more steps.

A more detailed analysis of how many steps are actually needed is shown in Figure 4.9. For this plot, the bunch addback with a maximum number of 20 steps is applied to the simulation of the 4^+ state of ^{16}C. It is recorded how many steps are needed until the algorithm terminates and all connected crystals are included. Events with the same number of steps are sorted into the same spectrum. As one can see, single crystal events without any contribution from their neighbors (0 steps) give the cleanest spectrum. Already events with entries only in the neighbors of the central crystal (1 step) show a significant smearing of the photopeaks and an increase in the sum peak. For 2 steps, this effect gets stronger and the two photopeaks are no longer separable. Beginning with 3 steps the photopeaks are no longer visible. Those events are dominated by the background. Since more and more crystals get summed up, the energy of the cluster increases.

As a conclusion, including more than one step in the bunch addback is not necessary since the events with more steps do not contribute significantly to the photopeaks. Therefore, NN addback is applied in the following analysis if not stated otherwise.

As a last step, I checked the necessity for a time cut during the cluster formation. In addition to the minimum and maximum energy threshold, the times of the neighboring crystals need to be within a certain time relative to the cluster center. The idea behind this cut is that energy entries originating from Compton scattering of the same γ ray have similar times, while background events might happen significantly earlier or later. Examining the influence of the time cut is done with experimental data since the background in the simulation is stemming only from protons. The protons are produced at the same time as the γ rays by the event generator. Hence, their time signature is very close to those of the γ rays. As expected, only the low energy (below

1.5 MeV) part of the spectrum is influenced by a time cut. For higher energies the changes are within the uncertainties of each bin. Furthermore, no changes bigger than the uncertainties are visible for a change of the maximum time difference from 1000 ns – comparable to no time cut – to 30 ns. Therefore, no time cut is applied during the addback process for the following γ-ray spectra.

4.4.3 Background

In addition to the γ rays from the excited states of the outgoing isotopes, other particles contribute to the γ-ray spectrum of XB. Due to the low proton number of the target and in contrast to most γ-ray spectroscopy experiments, the background in this experiment does not stem from bremsstrahlung or X rays from the target but from interactions of the knocked-out particles with the experimental setup, mainly XB.

In case of QFS reactions, in which two high energy protons are emitted, their contribution can easily be simulated as explained in Section 5.3. The protons are included in the simulation for the individual excited states and, therefore, contribute to their γ-ray spectra. Additionally, a simulation of two emitted protons without any γ rays is done to estimate the background from the ground state.

However, for knockout reactions on a C target, the situation is more complicated. Therefore, the background contribution is not simulated in this case. Instead, the background is estimated with the sum of an exponential function and a constant offset fitted to the data. This description matches the data for energies over 0.3 MeV. The reason of this mismatch for smaller energies lies in the decreasing γ-ray efficiency of XB due to hardware and software energy thresholds.

Another possible source for background in the γ-ray spectra, which is cosmic radiation, can be excluded. Since on-spill *XB Sum* trigger is demanded for γ-ray spectra, it is very unlikely that XB triggered due to cosmic background, while both POS and the TFW detect the specific incoming and outgoing particles. As a comparison: During the cosmic background run used in this work the off-spill *XB Gamma* Tbit is set for $\approx 4 \cdot 10^5$ events. Taking into account the duration of the run of $t_{\text{run}} \approx 2\,\text{h}$, the time of $t_{\text{DAQ}} \approx 500\,\text{ns}$ the DAQ needs to record an event, and the downscaling factor of 128 for this trigger, only in 0.36 % of the time such background events are detected. Their influence on the discussed γ-ray spectra is therefore negligible.

4.5 Protons

To be able to gate on a certain reaction mechanism like QFS, it is necessary to detect the scattered protons. Due to the big scattering angles of around 40° for QFS reactions, the protons are not detected in the proton arm of the R^3B/LAND setup, which only covers forward angles, but in XB, which covers almost 4π around the target. Protons traversing XB will either deposit their energy directly in the detector or produce secondary particles in reactions with, e.g., the detector material. The secondary particles might deposit their energy in the same or one of the neighboring crystals, but they can also leave the crystal and interact with one on the opposite side of the detector or leave the detector without further interaction. The protons can only deposit their whole energy in XB up to a kinetic energy of $\approx 275\,\text{MeV}$. Protons with higher kinetic energies will deposit only part of their energy and leave the detector afterwards. This

effect is called punch-through. Its energy depends on the material and the thickness of the crystals.

One can apply an addback algorithm similar to those for γ rays to the proton events. Although I am not interested in the total energy deposited by the protons and, therefore, do not need to reconstruct the energy, the addback algorithm can help to identify the protons correctly and to clean the γ-ray spectrum. In cases in which secondary particles are scattered to neighboring crystals, without an addback algorithm the energy of the secondary particles is either identified as an independent proton itself or is wrongly attributed to the γ-ray spectrum. This error can be avoided if – similar to the NN addback for γ rays in Section 4.4.2 – the neighboring crystals are attributed to the proton event. In case of the proton addback, the center of a cluster is defined by a crystal with *inf* as energy entry for the experimental data and an energy deposition above the corresponding threshold for the simulation. It is then checked whether the neighboring crystals have valid energy entries. If this is the case, their energy is set to 0.

This way, if the energy entries in two (or more) neighboring crystals exceed the thresholds for protons, they are counted as only one proton. In addition, since the proton determination and addback is done before γ-ray addback and Doppler correction, the energies of all neighbors of a proton are blocked and will not be used in the addback algorithm for the γ rays. However, if the energy entry in a neighboring crystal was not produced by a secondary particle or the proton itself but by a γ ray emitted by the fragment the proton addback algorithm destroys a valid entry. Nevertheless, the possibility of cleaning the γ-ray spectrum from the contribution from protons overweights the possible loss of γ-ray information. Therefore, the NN addback is used for the identification of the protons. A more complex addback algorithm like NNN or bunch addback is not necessary for protons since the secondary particles usually do not leave the second crystal. Furthermore, the information loss in the γ-ray spectrum increases with these addback algorithms since more crystals are attributed to a proton event.

In contrast to the γ-ray efficiency, which can be determined with source measurements as explained in Section 5.2, no measurements are available to determine the efficiency of the proton detection. Therefore, a simulation of the XB response is used to determine it. The simulation is explained in detail in Section 5.3.

4.5.1 Angular Distribution

To distinguish QFS reactions with hydrogen atoms from knockout reactions with carbon atoms in the CH_2 target, the number of detected protons and their angular correlation needs to be examined. For pure QFS reactions two protons emitted in opposite directions with an angle of $\approx 80°$ between them are expected, while for knockout reactions the proton emitted from the projectile might be emitted in forward direction and not be detected with XB. On the other hand, reaction products stemming from the target might be detected in XB, additionally. In the CH_2 target both QFS and knockout reactions take place, while in the C target only knockout reactions happen. As one can see in Figure 4.10 a) the proton multiplicity for the CH_2 target shows a higher fraction of two proton events than the C target. Furthermore, multiplicities higher than 2, probably stemming from the misidentification of two protons, are more likely for the CH_2 target.

Analyzing the spacial distribution of all events with two protons, the angle between the two protons in Figure 4.10 b) shows significant differences for the two targets. The direction of each proton is randomized within the detecting crystal before the angle between them is calculated to have a smooth distribution instead of a set of discrete angles between the center points of the

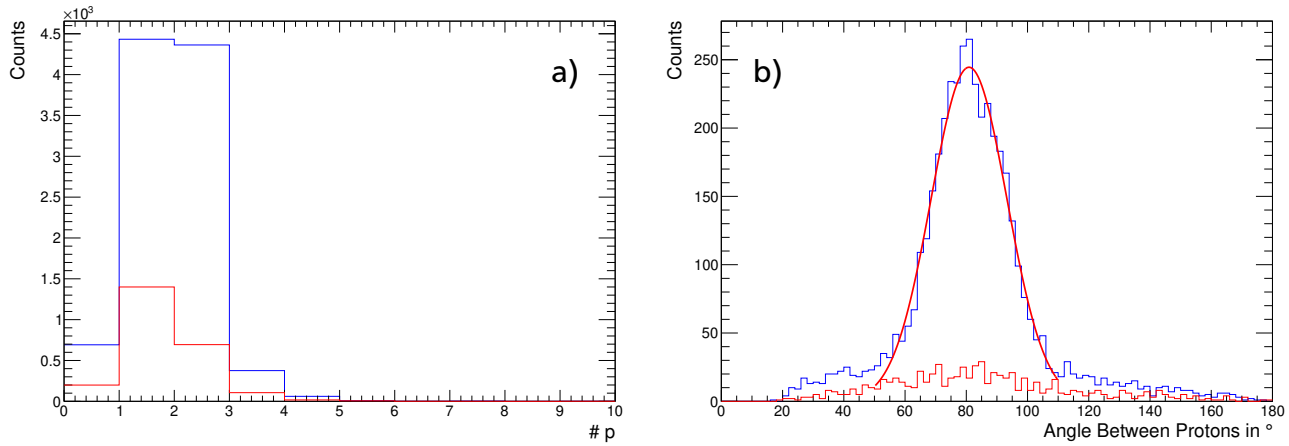

Figure 4.10: a) Proton multiplicity and b) angle between two protons for the CH_2 (blue) and C target (red). The plots are shown for setting 4 for the *XB Sum* Tbit and in case of the angle in b) with a cut on events with exactly two protons. The angles of the protons identified with XB are randomized over the whole area of the corresponding crystal. The average proton multiplicity is higher for the CH_2 than for the C target. In particular, it is more likely for two proton events to occur. Events with a multiplicity >2 are probably misidentified two proton events. The angle between the two protons for the CH_2 target (blue) shows a peak at 80.9° fitting to the expectation for QFS reactions. The one for the C target shows no such peak. Its contribution needs to be subtracted to obtain a pure H target.

crystals. For the CH_2 target, a broad but clear peak at 80.9° is visible, while for the C target no peak exists. The peak for the CH_2 target matches the expectation for QFS reactions. Both the proton multiplicity and the angle between the two protons are shown for setting 4 since this setting has the highest statistics. The corresponding plots for setting 3 and 6 can be found in Figure A.4 and A.11.

As a final check the polar and azimuthal angles of the two protons are plotted against each other in Figure 4.11. In this case the distributions are shown only for the CH_2 target. For one thing the number of events with two protons is too small for the C target to see any structure, for another thing no clear structure is expected for pure knockout reactions. Again, the angles are randomized within the crystal by which the proton is detected. The distribution of the azimuthal angle ϕ shows that most of the proton pairs are emitted back-to-back as expected for QFS reactions. The distribution of the polar angle θ shows the same angle between the two protons as seen before in Figure 4.10 b). As a conclusion, the signature of QFS reactions can clearly be identified for a CH_2 target. With a cut on events with two protons this reaction channel can be easily selected in the following.

4.6 Fit Procedure

To determine the number of reaction products in certain excited states, the experimental and simulated γ-ray spectra are compared. For each excited state and each known decay path – via a cascade or directly into the ground state – simulations are done, which are described in detail in Section 5.3.1. The NN addback algorithm, Doppler correction, and – in case of QFS

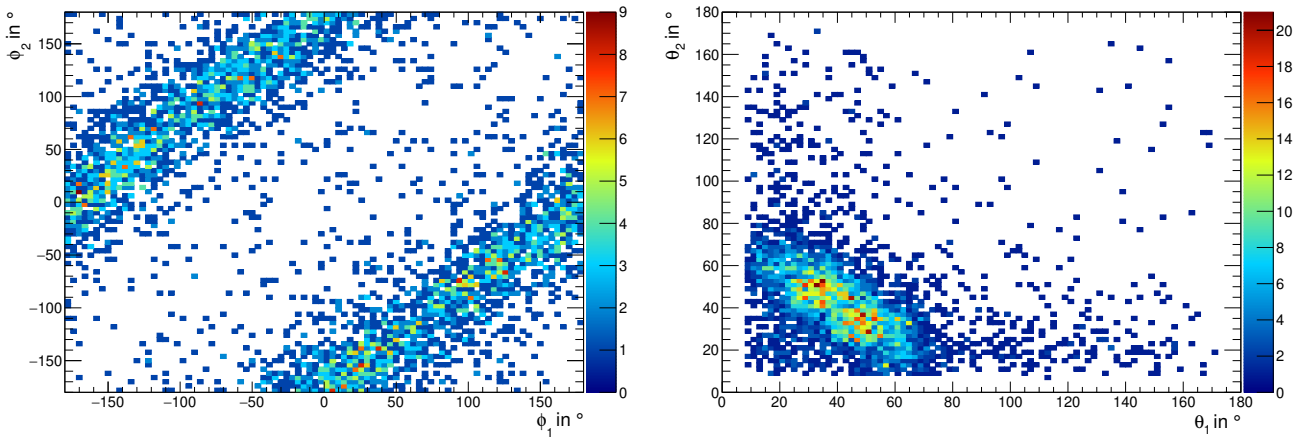

Figure 4.11: Angular correlation of the two protons from QFS reactions on the CH_2 target. The plots are shown for setting 4 for the *XB Sum* Tbit and a cut on events with exactly two protons. The angles of the protons identified with XB are randomized over the whole area of the corresponding crystal. The azimuthal angles ϕ of both protons (left) plotted against each other show the expected back-to-back scattering. The polar angles θ of the two protons (right) show an angle of $\approx 80°$ between them as expected for QFS reactions.

reactions – similar cuts on the proton multiplicity as explained above for the experimental data are applied to the output of the simulation. A sum of all simulated γ-ray spectra is then fit to the experimental γ-ray spectrum for the single and sum spectrum simultaneously.

For the fit, several methods are available which are introduced and compared in the following. Using the naming scheme of Baker and Cousins [BC84], the experimental data n_i are compared for each bin i with the prediction from the simulation y_i. The prediction y_i consists of the sum over all available simulations, each weighted with a factor that is determined by the fit. In case of knockout reactions, an exponential plus constant background is included in the prediction y_i. In general fitting contains three steps: The first step, called point estimation, is the determination of the best fit parameters matching the prediction to the experimental data. In addition, the uncertainty of the result needs to be determined. This step is called confidence interval estimation. Finally, the goodness-of-fit testing checks how good the prediction describes the data. The fit procedure might come to a result in step 1, but this last step will show if the model is suited to describe the data. The most common method to do all three steps is the usage of χ^2 statistics, but there are also methods available that only do the point and confidence interval estimation or the goodness-of-fit testing.

In this work, I compare different χ^2 estimators. In all cases, the point estimation is done by minimizing the χ^2 value. The result corresponds to a value χ^2_{best}. Problems can occur when the fit routine stops in a local minimum and does not find the global one. The uncertainties of the fit parameters are estimated by the values for which $\chi^2 = \chi^2_{\text{best}} + 1$ [PoPDG16, p. 525]. The goodness-of-fit is tested calculating the reduced χ^2

$$\chi^2_{\text{red}} = \frac{\chi^2_{\text{best}}}{\text{ndf}} \tag{4.2}$$

with ndf being the number of degrees of freedom of the fit. In the case of this work, in which histograms are compared bin by bin, the degrees of freedom can be estimated as the number of

bins used for the fit minus the number of parameters in the fit. The reduced $\chi^2_{\text{red}} \approx 1$ if the model is a good description of the experimental data [PoPDG16, p. 528], while values much larger indicate big discrepancies of model and experimental data. Values much smaller than 1 can happen for several reasons. For example, the experimental uncertainties might be overestimated or the model might be to flexible, i.e., it fits even statistical fluctuations. In addition, the underlying assumption like the statistical distribution might be wrong.

Baker and Cousins [BC84] summarize two versions of χ^2 estimators which are commonly used and based on a normal distribution of the data points. Pearson's χ^2_{P} uses the model prediction y_i to determine the best fit and its goodness

$$\chi^2_{\text{P}} = \sum_i \frac{(n_i - y_i)^2}{y_i}. \tag{4.3}$$

In my case, in which I can increase the number of simulated events and with this decrease the uncertainties of the model almost indefinitely, Pearson's χ^2_{P} is not a good choice. Additionally, due to the model y_i being a combination of several single simulations, the uncertainty of the model is recalculated for every set of fit parameters and depends on the result of the fit. On the contrary, Neyman's χ^2_{N} uses the experimental data n_i and their uncertainty Δn_i, respectively,

$$\chi^2_{\text{N}} = \sum_i \frac{(n_i - y_i)^2}{n_i} \tag{4.4}$$

$$= \sum_i \frac{(n_i - y_i)^2}{(\Delta n_i)^2}. \tag{4.5}$$

In both cases, the assumption is that the uncertainty of either the model or the experimental data follows a Poisson distribution with a sufficient sample size such that it follows a normal distribution. Therefore, the relationships $(\Delta n_i)^2 = n_i$ and $(\Delta y_i)^2 = y_i$ hold true. The majority of the γ-ray spectra in this thesis fulfills this requirement. However, the reconstructed γ-ray spectra for the H target are a combination of the corresponding C, CH_2, and empty target spectra as explained in Section 6.1. Therefore, the uncertainty of each bin is calculated with error propagation assuming a normal distribution. The relation $(\Delta n_i)^2 = n_i$ is no longer true, but the uncertainties are still normally distributed and Equation 4.5 can be used. Additionally, this version of Neyman's χ^2_{N} can handle negative bin entries, which might occur because of the subtraction of, e.g., the C target contribution, as long as they are still normally distributed. Therefore, this χ^2 estimator is the optimal choice for this work and will be used to determine the results.

Nevertheless, assuming a continuous normal distribution might not be the best idea for experimental data which are discrete and can have a small number of events in each bin. Better suited for such data is the Poisson statistic. In this case, one usually uses the principle of maximum likelihood for fitting. For histograms following the Poisson distribution, the likelihood function [BC84]

$$L_{\text{p}}(y, n) = \prod_i \left(\frac{(y_i)^{n_i}}{n_i!} e^{-y_i} \right) \tag{4.6}$$

needs to be maximized with respect to the parameters of the model y_i. Unfortunately, the likelihood function can only be used for point and confidence interval estimation but not for

goodness-of-fit testing. Bevington and Robinson describe in their textbook about statistics in data analysis [BR03] how one can combine the maximum likelihood function with the χ^2 approach. In this case, the χ^2_{B} estimator is given by

$$\chi^2_{\mathrm{B}} = -2 \cdot \ln\left(L_{\mathrm{p}}\right) + \text{const.} \tag{4.7}$$

Combining Equation 4.6 and 4.7, the χ^2 using the maximum likelihood method for the Poisson statistic is given by

$$\chi^2_{\mathrm{B}} = 2 \sum_i y_i - n_i \cdot \ln(y_i) + \text{const.} \tag{4.8}$$

In this case, minimizing χ^2_{B} is equivalent to maximizing L_{p}. However, with Bevington's χ^2_{B} goodness-of-fit testing is still not possible due to the unknown constant in the equation. Baker and Cousins [BC84] on the other hand introduce a χ^2 estimator which can be used for point and confidence interval estimation as well as for goodness-of-fit testing. Using the likelihood ratio test theorem they define

$$\lambda = \frac{L_{\mathrm{p}}(y, n)}{L_{\mathrm{p}}(m, n)} \tag{4.9}$$

with m_i being the true value of n_i within a perfect measurement without any uncertainty. With λ instead of L_{p} in Equation 4.7 and $m_i \approx n_i$ in Equation 4.9, they deduce

$$\chi^2_{\mathrm{BC}} = 2 \sum_i y_i - n_i + n_i \cdot \ln\left(\frac{n_i}{y_i}\right) \tag{4.10}$$

as the χ^2 estimator for the Poisson statistic. Unfortunately, the Poisson statistic does not allow negative bin entries, which leads to a non-defined behavior of Equation 4.10 for negative experimental bin entries n_i. Therefore, it can only be used for γ-ray spectra for C or CH_2 targets but not for reconstructed targets, for which negative bin entries might occur.

For the fits in this thesis I will compare Neyman's, Bevington's, and – if applicable – Baker and Cousins' χ^2 estimator to check the validity of the fit process. But due to the missing goodness-of-fit test for Bevington's χ^2_{B} and the general incompatibility of Poisson statistic and negative bin entries, I will use Neyman's χ^2_{N} for the final results.

5 Simulation

Simulations are a key component to understand and verify the results of nuclear physics experiments. In this work, I used the R3BRoot framework for the simulation of the behavior and response of the γ ray and particle detector XB. I will explain the concept of R3BRoot and my simulation in general, before I describe the two main simulations I did for this thesis. The first one is the simulation of a ^{60}Co source to check the behavior of the simulation framework and determine the γ-ray efficiency of the detector system, which can be cross checked with experimental data. The results of the second set of simulations are fit to the γ-ray spectra to determine the fraction of the different excited states. With this the proton amplitudes and the cross sections are calculated. Furthermore, the efficiency to detect protons with XB is determined from these simulations.

5.1 R3BRoot Framework

The simulation and analysis framework R3BRoot [r3b18] is used for all simulations in this thesis. It is supposed to combine all calibration and analysis steps and the simulation of detector responses for the future R^{3}B setup. The goal is a similar treatment of experimental and simulated data from an early analysis step on. At the moment, the simulation part is already running under stable conditions, while the data analysis part is still under development. Therefore, I use R3BRoot only for the simulations and *land02* for unpacking and calibration as described in Chapter 4.

R3BRoot is a C++ based, modular software package. It inherits its major functionality from the FairRoot framework [fai18] but adds setup specific geometries, detector behaviors, and calibration procedures. Both frameworks are based on ROOT [BR97] for data storage and analysis, while for simulations, GEANT3 or GEANT4 transport engines are utilized. For all simulations in this work I use GEANT4. In the used R3BRoot version this corresponds to GEANT4 version 10.2.1. A general overview of GEANT4 and its improvement in recent years is given in [AAA$^+$03, AAA$^+$06, AAA$^+$16]. Detailed information and tutorials can be found on the webpage [gea18]. For an easier installation, all necessary software packages in their compatible versions are combined in Fairsoft.

The first step in all simulations is the definition of the detector geometry. As mentioned before, this task is simplified by the R3BRoot framework since all detectors used in the R^{3}B/LAND setup are already implemented. I placed two detector systems in the world volume of my simulations. The first one is the detector of interest XB. Its geometry includes the aluminum housing of the crystals and the target chamber. Additionally, the SSDs surrounding the target were placed inside the chamber. All eight detectors together are called TRACKER in R3BRoot. Their geometry includes the target wheel as well as the holding structure for the SSDs and their electronics. Although the information from the active element TRACKER is not used in the analysis of the simulations, the material inside the target chamber is important for the correct

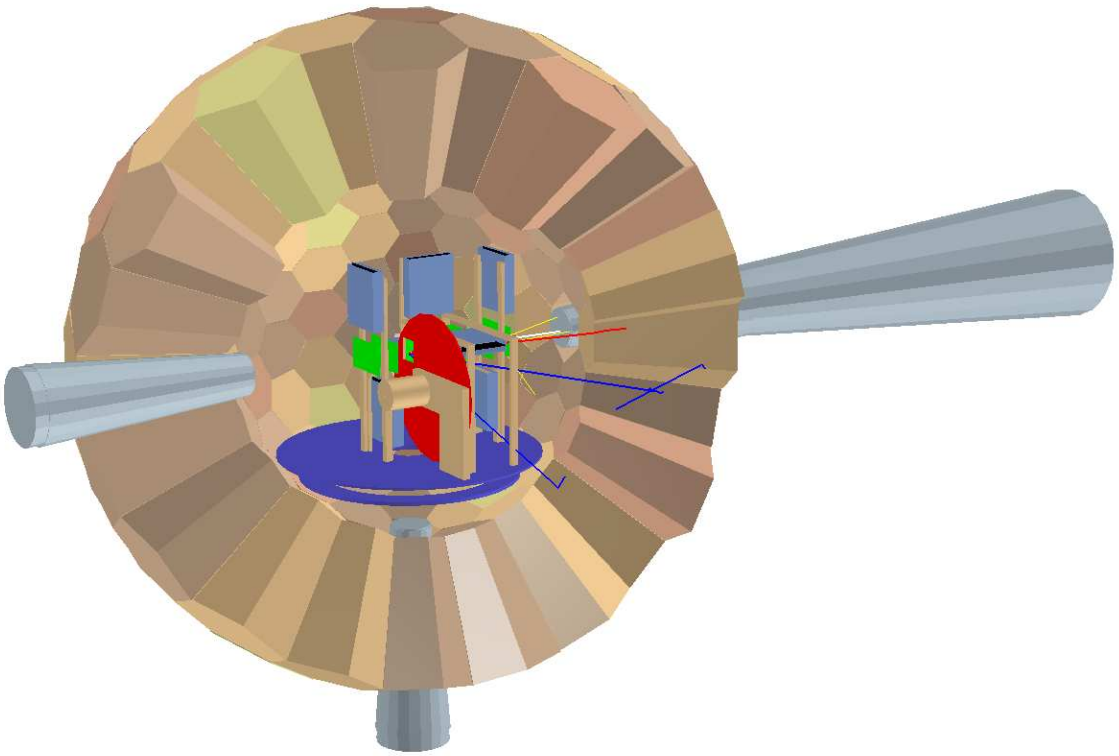

Figure 5.1: Setup for the R3BRoot Simulations: XB and TRACKER are placed around the target position. The TRACKER consists of the eight SSDs (green slides) together with their readout electronics (grey blue boxes), the target wheel (red) without a dedicated target, and the holding structure (brown and blue). Around it, half of all XB crystals are depicted in different shades of brown. The second half of the crystals and the vacuum chamber are not shown to enable the view on the target position. In addition to the geometry, one event of the ^{17}N(p,2p)^{16}C reactions is depicted. Only one of the two protons (red) is visible, while the two γ rays (blue) from the cascade $2_2^+ \rightarrow 2_1^+ \rightarrow 0^+$ and their interaction with XB is shown. The outgoing ^{16}C (white) and secondary electrons (yellow) from its interaction with the SSDs are visible as well.

simulation of the straggling of the protons and γ rays. The final setup is depicted in Figure 5.1, while the TRACKER itself is depicted in Figure 3.5 a).

After the geometry of the simulation is defined, the particles of interest – in my case protons and γ rays – need to be generated. GEANT4 as well as R3BRoot provide the functionality to produce such particles, but they are usually quite limited. Therefore, external scripts, called event generators, were used to define the point of origin, momentum, and energy of the particle to simulate. This information is then fed into the simulation and used as the starting point. The details of the used event generators are described in the corresponding sections.

In GEANT4 the propagation of the particles and their interactions with the environment is managed with so-called physics lists. Each physics list defines the behavior of certain particles described by a model. Depending on the application different physics lists offer the best – time and accuracy wise – implementation of the processes of interest. In the case of this work, the Penelope physics list (`G4EMPenelopePhysics`) is used for electromagnetic processes. It focuses on the implementation of low energy γ rays with energies up to 1 GeV. For hadronic processes several

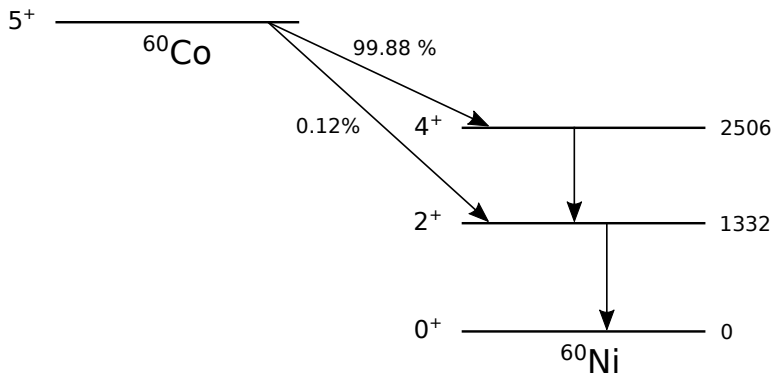

Figure 5.2: Level scheme for the β decay of ^{60}Co to ^{60}Ni. The energies of the levels are given in keV and taken from [BT13].

physics lists were used. Elastic scattering processes (`G4HadronElasticPhysics`) and interactions of hadrons with γ rays, electrons, and muons (`G4EmExtraPhysics`) are described separately from the inelastic scattering of hadrons in the QGSP_INCLXX model (`G4HadronPhysicsINCLXX`). A detailed overview of most available physics lists and the implemented processes is given in [Col17].

Finally, the result of the simulation consists, among others, of energy, position, and time measurements for every detector subsystem. Since I am only interested in the behavior of XB, the SSDs were only included to simulate energy and angular straggling correctly and their data are, therefore, not analyzed. Unfortunately, the simulation includes only straggling but not the behavior of, e.g., PMTs and the electronic readout. Therefore, an external script is used to apply a realistic detector resolution to the simulated data. The energy resolution of each crystal is determined from γ-ray source measurements for energies below 2 MeV. The simulated energy is folded with a normal distribution to reproduce the detector resolution. Its standard deviation is given by $\sigma_E = m \cdot \sqrt{E} + t$ with the slope m and the offset t determined from the source data. Additionally, the simulated time is folded with a normal distribution with a fixed standard deviation of $\sigma_t = 3.8\,\text{ns}$ to achieve a realistic time distribution.

5.2 Source Simulation for γ-ray Efficiency

The first simulation is done to check the reliability of the simulation framework concerning the efficiency of γ-ray detection. The γ-ray spectra of the second set of simulations is later used to determine the total number of fragments in excited states. Therefore, the efficiency of XB in the simulation and the experiment need to agree. Otherwise, a correction needs to be applied.

To determine the absolute photopeak efficiency either a source with a well known activity or one with two successive γ rays is used. If a source with a single γ ray is used, its activity and the measurement time needs to be known very precisely. This is not the case for the source runs during the experimental campaign S393. Therefore, I use a ^{60}Co source. Since it mainly decays into the 4^+ state of ^{60}Ni, which decays via a cascade of two successive γ rays with the energies $E_1 = 1.173\,\text{MeV}$ and $E_2 = 1.332\,\text{MeV}$, a gate on one of the two energies allows for the determination of the absolute photopeak efficiency for the other γ-ray energy. The simplified level scheme of the decay is depicted in Figure 5.2.

Several methods can be used to determine the absolute photopeak efficiency with a source of two successive γ rays. Ronja Thies introduces three of these methods and their application to XB data in [Thi11]. I will shortly summarize two of them – the sum-peak method and the counting method – before I reason why I decided to use the counting method despite its shortcomings.

The sum-peak method compares the number of events in the sum peak with the number of events in the single peaks in the spectrum of each crystal. The sum peak contains events in which both γ rays are detected in the same crystal, while the single peaks contain those in which only one is detected. Taking into account the angular correlation of the γ rays and the segmentation of XB with the correction factor c the absolute photopeak efficiency can be determined by the ratio of the sum-peak events n_{sum} to the single-peak events n_{single}

$$\epsilon_{\text{sum-peak}} = c \cdot \frac{n_{\text{sum}}}{n_{\text{single}}}. \tag{5.1}$$

This method is widely used for γ-ray detectors as, e.g., Euroball [HCGR98] or GRETINA [PLM+13] and described in detail in the literature [HMM73, VKL03, OMI+15]. Unfortunately, for the chosen source run in most of the spectra, the sum peak is not clearly distinguishable from the background to be fit. The statistics in the single crystal spectra and the detector resolution are not good enough to use this method.

The counting method on the other hand compares the events in a single peak of one crystal to the number of events in the second single peak in the whole detector array. The number of events in the photopeak at E_1 in the whole detector is called $N_{1,\text{total}}$ and used as a trigger. In all these cases, one expects the detection of the second γ ray in one of the other crystals. Counting all events $N_{2\text{ if }1}$ in which the energy loss E_2 is detected in a certain crystal under this condition, the absolute photopeak efficiency for the γ ray energy E_2 for this crystal can be calculated as

$$\epsilon_{\text{counting},2} = \frac{162 \cdot N_{2\text{ if }1}}{N_{1,\text{total}}}. \tag{5.2}$$

The factor 162 takes the granularity of the detector into account. Furthermore, a cut on the photopeak at E_2 in the whole detector array, counting all events $N_{1\text{ if }2}$ with energy E_1 in the single crystals, gives the corresponding efficiencies for the γ-ray energy E_1.

This method has several disadvantages: Since the detection in a single crystal is determined relative to the detection in the other crystals, the efficiency varies with material placed inside XB, like the target wheel and the SSDs. The material leads to a decrease in triggering γ rays and, therefore, to an artificial increase in measured efficiency. Furthermore, the uncertainty estimation for the absolute photopeak efficiency is not trivial. The mean and standard deviation of the two normal distributions fit to the spectrum of each crystal are correlated. They define the energy range of the single peaks in which events are counted. Therefore, their influence on the efficiency is non trivial and cannot be described in an easy way. Nevertheless, this method is suitable to compare simulation and source measurement since the material is present in both cases and the same ranges are used.

The event generator for this simulation produces one or two γ ray(s) according to the decay of ^{60}Co summarized in Figure 5.2. In almost all cases (99.88 %) ^{60}Co decays to the 4^+ excited state of ^{60}Ni, which in turn decays via the 2^+ excited state emitting two successive γ rays. Due to the angular momenta of the involved states, the angle θ between the two γ rays show an

Table 5.1: Angular correlation coefficients a_2 and a_4 for the γ-ray cascades used in this work. The coefficients are taken from [Kam14].

$I_A(l_1)I_B(l_2)I_C$	a_2	a_4
2(2)2(2)0	-15/13	+16/13
3(1)2(2)0	-3/29	0
4(2)2(2)0	+1/8	+1/24

angular dependency. The angular correlation function $W_{2D}(\theta)$ describes the abundance of the angle θ for a two-dimensional setup. As described in [Kam14], the correlation function is usually normalized to $W_{2D}(90°) = 1$ and cut after the fourth order. It is given by

$$W_{2D}(\theta) = 1 + a_2 \cdot \cos^2\theta + a_4 \cdot \cos^4\theta \tag{5.3}$$

with the coefficients a_2 and a_4 depending on the angular momenta of the involved levels. The coefficients used in this work for the simulation of the ^{60}Co source as well as the excited ^{16}C and ^{18}C fragments are listed in Table 5.1. They are given for each sequence $I_A \rightarrow I_B \rightarrow I_C$ with l_1 and l_2 being the angular momenta of the emitted γ rays. To take the 4π coverage of XB into account Equation 5.3 needs to be slightly modified to

$$W_{3D}(\theta) = (1 + a_2 \cdot \cos^2\theta + a_4 \cdot \cos^4\theta) \cdot \sin\theta. \tag{5.4}$$

The additional $\sin\theta$ takes into account that the crystals cover a three-dimensional sphere and that each solid angle is weighted equally. Generating two successive γ rays, the event generator choses the direction of the first γ ray randomly but equally distributed on a sphere. For the second γ ray, the angle θ is then chosen according to Equation 5.4 which defines the direction together with a randomly chosen rotational angle ϕ. In the few cases (0.12 %) in which ^{60}Co decays into the 2^+ excited state of ^{60}Ni only one γ ray is emitted. Although those events cannot be used for efficiency determination, the event generator generates them according to the given branching ratio and they are simulated for the sake of completeness.

After the simulation is done, the first step is the conversion from an R3BRoot specific to a *land02* specific data format. Furthermore, the detector resolution is applied as described in the previous section. Since an addback algorithm is applied to the XB data for the γ-ray spectra of ^{16}C, ^{18}C, and ^{20}C, the same is done for the source spectrum. For both simulated and experimental data the NN addback algorithm described in Section 4.4.2 is used.

As a first check, the simulated and measured spectra are compared. One problem is that the measured source spectrum includes not only γ rays from the ^{60}Co source but also some from cosmic background. As soon as their energy entries are above the energy threshold they trigger the DAQ and their energy loss is recorded. However, dedicated cosmic runs are recorded in which neither a source nor beam is present. This data – again with NN addback applied – can be used to either subtract the background contribution from the measured source spectrum or to add the background to the simulated spectrum. I decided for the second option and fit the sum of the simulated and the background spectrum to the measurement. The resulting spectrum for a single crystal is shown in Figure 5.3. In principle one would expect that the scaling for the

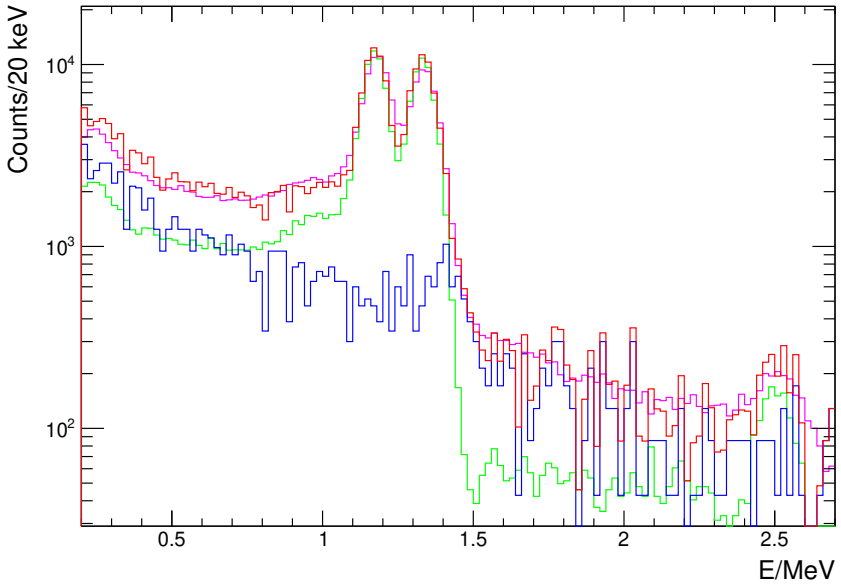

Figure 5.3: Simulated and measured γ-ray spectrum of a ^{60}Co source after NN addback for crystal #133. The simulation (green) plus background from cosmic radiation (blue) is fit to the source measurement (pink). The result of the fit is plotted in red.

background relative to the source measurement is known. Unfortunately, taking into account the duration of the cosmic and source run, the dead time of the DAQ, and the different downscaling factors, the background contribution is strongly underestimated. The reason for this discrepancy could not be found. Therefore, the scaling of the simulation as well as the background are determined by the fit.

To determine the absolute photopeak efficiency using the counting method presented above, the events corresponding to the photopeaks need to be selected. For this, a combination of two normal distributions and a linear function is fit to the spectrum of each crystal. Since the energies of ^{60}Co are close to each other and the NaI crystals have a bad energy resolution, events within only one standard deviation around the mean value of each peak are counted. Although usually at least two standard deviations are preferred, this is not possible since otherwise some events would count for both energies.

The resulting gated spectra for the source measurement contain again events from the cosmic background. In particular the number of triggering γ rays $N_{1,\text{total}}$ and $N_{2,\text{total}}$ is overestimated, whereas the background contribution to the coincidence spectra corresponding to $N_{1\text{ if }2}$ and $N_{2\text{ if }1}$ is negligible. To estimate the amount of background contamination, the gated spectra are fit. For the determination of the number of triggering γ rays $N_{1,\text{total}}$ ($N_{2,\text{total}}$), the simulated spectrum together with the spectrum from the cosmic background is fit to the source measurement in the given energy range, while in the coincidence window of the second γ ray only the simulation is fit to the spectrum of the source run to determine $N_{2\text{ if }1}$ ($N_{1\text{ if }2}$). With this, the background contribution can be estimated and subtracted to clean the source measurement. This inclusion of the background contribution was first done by Valerii Panin [Pan16] in his analysis.

Finally, the absolute efficiencies are calculated using Equation 5.2. Figure 5.4 shows the efficiency for each crystal for both available energies and for the source measurement and the simulation. As one can see, the simulation nicely reproduces the general structure, which is

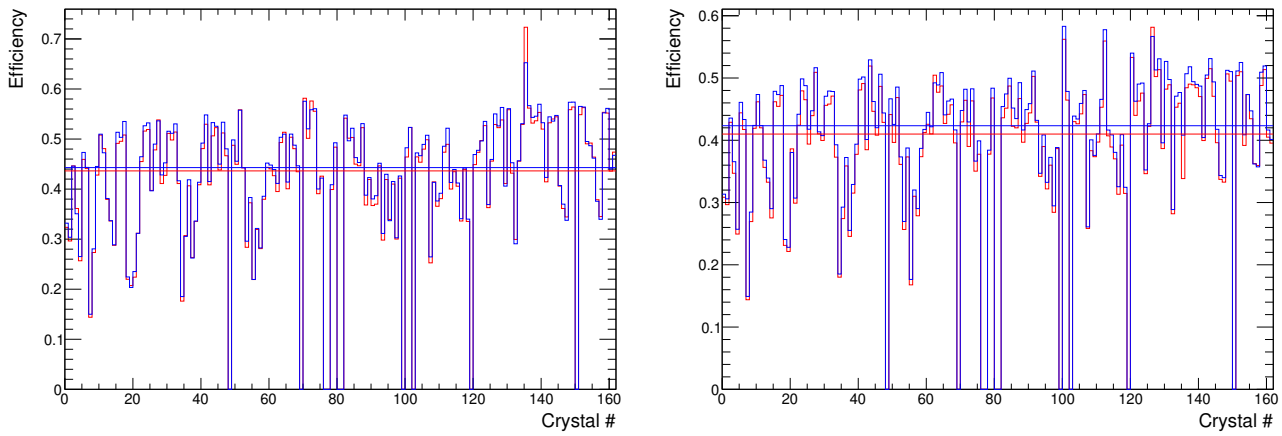

Figure 5.4: Absolute photopeak efficiency after NN addback for γ rays with an energy of $E_1 = 1.173\,\text{MeV}$ (left) and $E_2 = 1.332\,\text{MeV}$ (right). The efficiency from the simulation is plotted in blue, while the one from the source measurement is plotted in red. The horizontal lines show the mean value over all crystals listed in Table 5.2.

Table 5.2: Absolute photopeak efficiency for an experimental and simulated source measurement after NN addback.

	$E_1 = 1.173\,\text{MeV}$	$E_2 = 1.332\,\text{MeV}$
source measurement	43.6 %	41.0 %
simulation	44.3 %	42.3 %

caused by the inhomogeneous material inside the vacuum chamber. However, the plots as well as the mean value over all crystals in Table 5.2 indicate that the simulated efficiencies are slightly higher than the measured ones. Since the differences are small and the overall picture is correct, I trust the simulation but correct for the crystal specific and overall discrepancies by applying correction factors to the simulated spectra in the following.

5.3 QFS Simulation

The second set of simulations focuses on the actual physics cases. It simulates the detection of two protons emitted according to the kinematics of QFS reactions and potential γ rays emitted by the excited fragment during this process and the response of XB. For this purpose, an event generator is needed which provides both the protons from the QFS reaction and the successive γ rays. The QFS event generator was developed by Leonid Chulkov and Valerii Panin. It is described in detail by Chulkov et al. [CAB+05] and by Valerii Panin [Pan12]. As a general idea, it uses the Feynman diagram technique to describe the scattering of a nucleus with four-momentum $\mathbf{P}$ with a proton from the target $\mathbf{p_0}$. The reaction is split into two vertices. The first vertex describes the dissociation of the nucleus into the remaining fragment $\mathbf{Q}$ and a virtual intermediate proton with the four-momentum $\mathbf{p_e}$. The second vertex then represents the actual elastic scattering process of the target proton with the virtual intermediate proton. After the reaction, the scattered protons have the four-momenta $\mathbf{q_0}$ and $\mathbf{q_1}$, while the remaining fragment has the four-momentum $\mathbf{Q}$. The Feynman diagram of the reaction is shown in Figure 5.5.

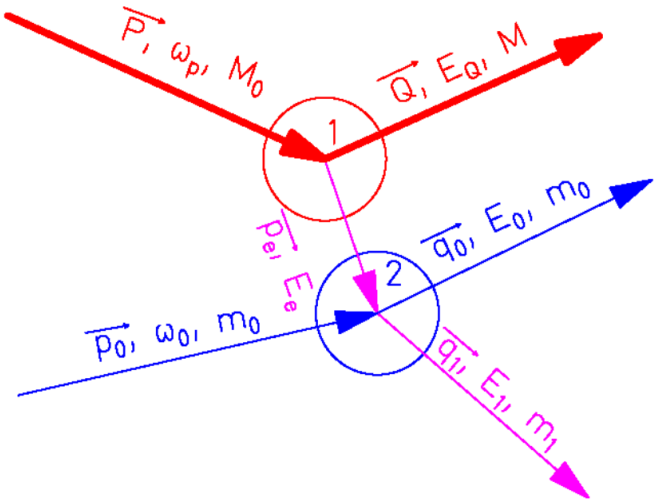

Figure 5.5: Feynman diagram for a QFS reaction using the impulse approximation. The notation is explained in the text. The figure is taken from [CAB+05].

In a second, completely independent step, γ rays are added. Depending on the state of interest, one or two monoenergetic γ rays are produced. In case of a single γ ray, its direction in the c.m. system is chosen randomly but equally distributed on a sphere. In case of a cascade from a higher lying state, the direction of the first γ ray is picked randomly, but the direction of the second one is chosen according to the angular momentum of the involved states as explained before for the ^{60}Co source. Equation 5.4, together with the angular correlation coefficients in Table 5.1, gives the angle θ between the two γ rays in the c.m. system. After the production of each γ ray, its energy and its polar angle θ are Doppler boosted from the c.m. frame to the laboratory frame.

Finally, all information is combined to the output of the event generator. For each particle its momentum, the point of origin in the target, and its mass are stored together with the particle's PDG code.

The whole event generator needs several input parameters. The QFS event generator needs the mass and charge of all involved particles as well as the energy of the incoming isotope and the internal momentum spread of the outgoing fragment. The energy of the incoming beam is provided by *land02* and listed in Table 5.3. The internal momentum spread is set to 100.5 MeV/c for all three isotopes. For the production of the emitted γ rays, their energy and – for the case of two γ rays – their angular correlation need to be specified. In the case of this work, the energies and angular momenta given in Figure 2.5 are used together with the angular correlation coefficients from the literature [Kam14] listed in Table 5.1. Additionally, the position and spread of the beam on the target is needed to simulate a realistic distribution of the points of origin. This information is again extracted from *land02*.

For the analysis of the knockout reactions from the C target, only the second part of the event generator is used. In this case, neither the fragment nor any protons emitted by the isotope of interest or the target are simulated but only the γ rays.

The simulation of the response of XB to QFS events is used in two ways in the analysis. First of all, the simulated γ-ray spectra are fit to the experimental spectra to determine how many events

Table 5.3: Energy of the incoming beam for the three different settings given by *land02* and used in the simulation.

	E_{inc}/AMeV	β_{inc}
Setting 3: $^{17}\mathrm{N} \rightarrow {}^{16}\mathrm{C}$	438	0.733
Setting 4: $^{19}\mathrm{N} \rightarrow {}^{18}\mathrm{C}$	430	0.729
Setting 6: $^{21}\mathrm{N} \rightarrow {}^{20}\mathrm{C}$	422	0.725

belong to each excited state. Using this approach, the absolute γ-ray efficiency of XB is taken into account without explicitly correcting for it. Secondly, the simulation is used to determine the proton efficiency of XB. Both aspects are described in the following.

5.3.1 γ-ray Spectrum

As before, a conversion from an R3BRoot specific to a *land02* specific data format needs to be performed after the simulation is done. Furthermore, an energy and time resolution is applied to the output of the simulation as explained in the previous section.

Afterwards the simulated and the experimental data are treated the same way. As for the in-beam data and the simulation of the source measurement, the NN addback algorithm is applied. The algorithm and its effect on the data are discussed in Section 4.4.2. Since the simulation includes Doppler boosted γ rays, the same Doppler correction as for the measured data is used to reconstruct the γ-ray energies in the c.m. system. The Doppler correction was introduced in Section 4.4.1. Furthermore, cuts similar to the ones for the experimental data are applied to the simulations. In case of the analysis of QFS reactions, this includes a cut on the number of detected protons. Additionally, a time cut with $-20\,\mathrm{ns} < t < 20\,\mathrm{ns}$ is used. The width of the cut $\Delta t = 40\,\mathrm{ns}$ matches the one for the experimental spectra and is chosen almost symmetrically around the most probable time of $t = 1.8\,\mathrm{ns}$. However, these restrictions decrease the number of entries in the spectrum only slightly but do not influence the overall shape.

To describe the experimental spectra, several simulations are necessary. The decay of each excited state is simulated separately. In case of ^{18}C and its higher lying state, both the direct decay to the ground state and the decay via the first excited 2_1^+ state are simulated separately. For the higher lying 2_2^+, 3^+, and 4^+ state of ^{16}C, only the decay via the cascade is simulated since the direct decay was not measured in a previous measurement [PPC$^+$12]. Furthermore, a simulation without any γ ray but with only two protons and the fragment is done to account for the contribution from the ground state. Although no γ ray is emitted, small amounts of energy can be deposited in the crystals due to the scattering and secondary reactions of the protons. These energies can then be seen in the γ-ray spectrum.

As an example, the output of the QFS simulations for ^{18}C are depicted in Figure 5.6. The left picture shows the single spectra in which the energy of each cluster is plotted. It displays the direct decay from the first excited state and the higher lying state each with a single photopeak, whereas the cascading decay from the higher lying state shows two photopeaks corresponding to the two successive γ rays. Additionally, the contribution from the two protons from the QFS reaction is shown for a simulation without any γ rays. It is also included in the spectra for the excited states. The energy resolution increases with higher energies. Therefore, the direct decay

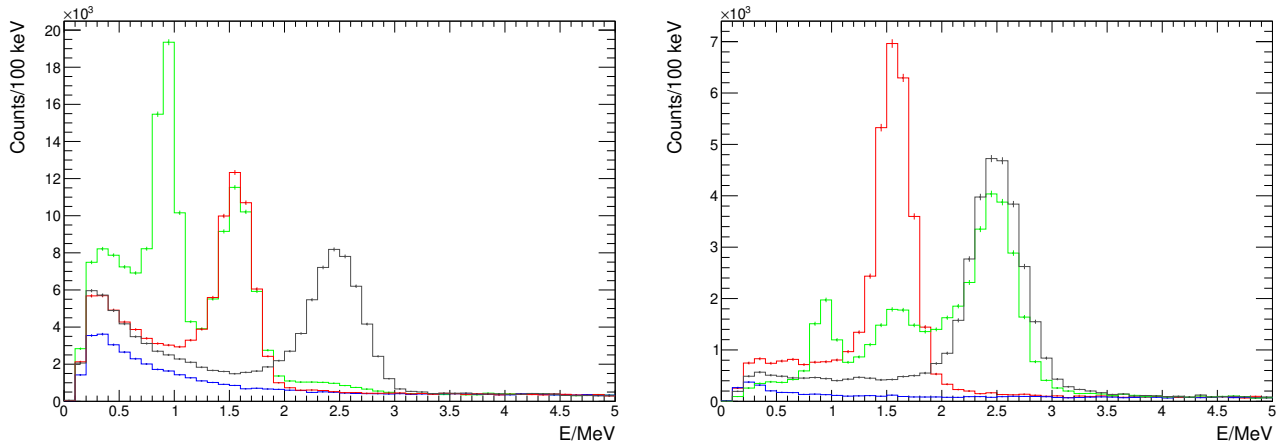

Figure 5.6: Simulated single (left) and sum (right) γ-ray spectra. The two excited states of ^{18}C are simulated: the first excited 2^+_1 state (red) and the higher lying (2^+_2) state decaying via the first excited state (green) or directly into the ground state (black). The background spectra (blue) show the contribution from the detection of the protons. All spectra include proton and γ-ray NN addback. The time cut and a cut on proton multiplicity 2 are applied.

of the higher lying state with an energy of $E = 2.517\,\text{MeV}$ is broader than, e.g., the peak at $E = 0.932\,\text{MeV}$ from the cascade. Due to the relatively large crystals, the bad energy resolution, and the background from the protons no escape peaks can be identified.

For the sum spectra on the right, the energies of all clusters are summed up. This leads to a reduction of the Compton background for all spectra, which is most visible for the cases of single photopeaks due to the direct decay. The spectrum for the decay of the higher lying state via the first excited state displays three peaks. The two lower lying peaks correspond to events in which only one of the two γ rays of the cascade is detected in XB. This happens if the other one either escapes the detector or deposits its energy in crystals next to a proton hit, which are blocked by the proton NN addback. The third peak at $E = 2.517\,\text{MeV}$ belongs to the events in which both γ rays, and with this the whole excitation energy of the higher lying state, are detected. In all cases, the background contribution from the protons decreased significantly as one can see from the dedicated spectrum.

The results of the simulations for the knockout reactions on a C target look very similar. As explained before, no protons are simulated in this case and no proton cut can be applied to the data. Everything else, including the artificial time and energy resolution, the γ-ray NN-addback and Doppler correction, and the time cut, is exactly the same as for the QFS simulations. However, the simulated spectra do not include any background. Hence, the fit of the simulated spectra to the experimental spectra includes an exponential plus constant background to correct for this.

Finally, a combination of the resulting spectra is fit to the experimental spectrum with the scaling of each simulated spectrum as a fit parameter. One can then calculate the number of events for each state from the scaling factor multiplied with the number of simulated events. Since the different decay channels are simulated separately, one can identify contributions from higher lying states to the strength of the first excited state. Therefore, no correction needs to be done to account for sidefeeding of the channel of interest. The results of the fits are presented in Chapter 6.

5.3.2 Proton Efficiency

To calculate the cross sections for QFS reactions, the total number of reaction products needs to be known. However, only for a fraction of the actual QFS reactions both protons are detected and the reaction channel is identified correctly. Therefore, the number of events is corrected with the efficiency ϵ_{2p} to detect exactly two protons. The proton efficiency of XB is calculated as

$$\epsilon_{2p} = \frac{N_{2p}}{N_{\text{total}}} \tag{5.5}$$

with N_{2p} the number of events with proton multiplicity 2 and N_{total} the total number of events with two protons from QFS reactions. Since the total number of events with two protons emitted is not known for the experimental data, the simulation of the detector system is used to determine the proton efficiency.

Again the simulation is treated like the experimental data wherever possible. For the experimental data, a proton is identified by an overflow in the γ-ray branch of a crystal. The threshold above which an energy is stored as *inf* depends on the crystal. Since the γ-ray energies in the laboratory frame are boosted to higher energies in forward direction and to lower energies in backward direction, the amplification is set for each crystal separately to cover the energy range of interest. Therefore, crystal dependent thresholds are applied to the simulations to identify the protons in a way which matches the experiment the best. I use the thresholds which Matthias Holl determined and used in his analysis presented in [Hol14]. During the identification of the protons, the NN addback is applied with the result that high energy entries located next to each other are counted as one proton. The procedure is explained in Section 4.5 for the experimental data.

In Table 5.4 the proton efficiencies for all three settings are listed. With a total number of simulated events of $N_{\text{total}} = 100\,000$, the uncertainties due to statistics are in the order of a few per mille. The decrease in efficiency for higher mass number can be explained by the different energies of the protons. The thresholds to identify a proton are the same for all simulations. Hence, more protons deposit energies above the thresholds if their energies are higher. Due to the slightly higher energy of the lighter incoming isotopes, the proton efficiency is then higher for setting 3 than for setting 4 and 6.

As a last cross check for the event generator, the simulation, and its ability to reproduce the detector behavior for protons, the multiplicity and the angular distribution of the protons are analyzed. The proton multiplicity is depicted in Figure 5.7 a). In contrast to the experimental data for the CH_2 target in Section 4.5.1, for which both knockout and QFS reactions take place, only QFS reactions are simulated. Therefore, the most probable events are those with multiplicity

Table 5.4: Simulated efficiency to detect exactly two protons with XB for the different settings.

	$\epsilon_{2p}/\%$
Setting 3: $^{17}\text{N} \rightarrow {}^{16}\text{C}$	57.4(3)
Setting 4: $^{19}\text{N} \rightarrow {}^{18}\text{C}$	56.2(3)
Setting 6: $^{21}\text{N} \rightarrow {}^{20}\text{C}$	55.4(3)

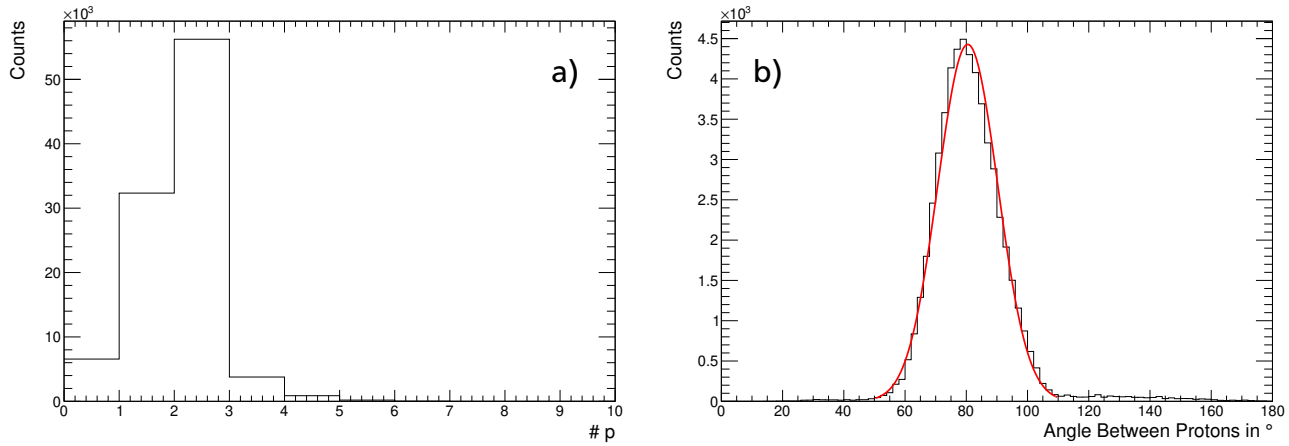

Figure 5.7: a) Proton multiplicity and b) angle between two protons for simulations of QFS reactions. The plots are shown for the ^{19}N(p,2p)^{18}C reaction and in case of the angle in b) with a cut on events with exactly two protons. The angles of the protons identified with XB are randomized over the whole area of the corresponding crystal. The angle in b) shows a peak at 80.5° fitting to the experimental value in Figure 4.10.

2, whereas – because of the contribution from the carbon – multiplicity 1 and 2 events are equally likely for the experimental CH_2 target. Note that in the simulation, as well as in the experimental data, for a significant amount of events no proton is detected. This is the case for $\approx 6.5\,\%$ of the events in the simulation.

The angle between the two protons in Figure 5.7 b), as well as the distribution of their azimuthal and polar angle in Figure 5.8, show the characteristics of the QFS reaction. With 80.5°, the angle between the protons is close to the experimental value and the expected value in general. The azimuthal angles ϕ illustrate the back-to-back scattering, while the distribution of the polar angles θ again illustrates the angle of $\approx 80°$ between the protons. The accumulation at $\theta \approx 40°$ is expected, since the energy is usually equally distributed among the two protons involved in the scattering process.

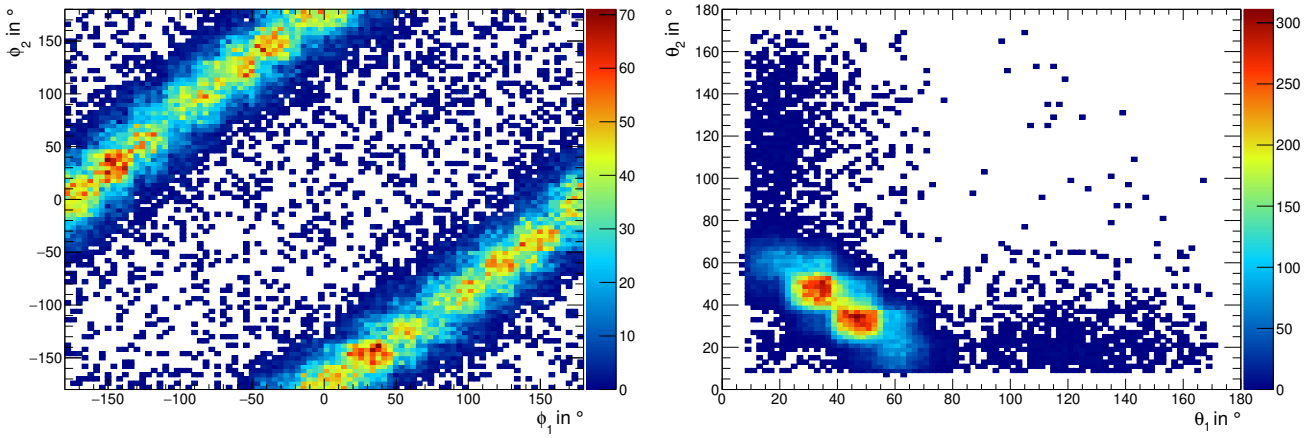

Figure 5.8: Angular correlation of the two protons from simulations of QFS reactions. The plots are shown for the ^{19}N(p,2p)^{18}C reaction with a cut on events with exactly two protons. The angles of the protons identified with XB are randomized over the whole area of the corresponding crystal. The azimuthal angles ϕ of both protons (left) plotted against each other show the expected back-to-back scattering. The polar angles θ of the two protons (right) show an angle of $\approx 80°$ between them as expected for QFS reactions.

6 Results

In this chapter I present the results of my analysis. First of all, I introduce the general idea of the reconstruction of a pure H target, before I summarize the way the data are processed. Details of this procedure can be found for the experimental and simulated data in Chapter 4 and 5, respectively. As the next step, the fit is explained. The resulting spectra for all reactions of interest are shown. Finally, the proton amplitudes as well as inclusive and exclusive cross sections are calculated. The results are discussed in comparison to previous measurements and the expectations from eikonal calculations.

In principle, a pure proton target is needed for the measurement of QFS reactions. Since no such target was available, two measurements with a CH_2 and a C target were performed separately. To reconstruct the contribution from the protons in the CH_2 target, the C target contribution is subtracted afterwards as described by

$$H_{\mathrm{H_2}} = H_{\mathrm{CH_2,corr}} - \frac{I_{\mathrm{CH_2}}}{I_{\mathrm{C}}} \cdot \frac{\tau_{\mathrm{CH_2}}}{\tau_{\mathrm{C}}} \cdot H_{\mathrm{C,corr}} \tag{6.1}$$

$$= H_{\mathrm{CH_2}} - \frac{I_{\mathrm{CH_2}}}{I_C} \cdot \frac{\tau_{\mathrm{CH_2}}}{\tau_{\mathrm{C}}} \cdot H_{\mathrm{C}} - \left(1 - \frac{\tau_{\mathrm{CH_2}}}{\tau_{\mathrm{C}}}\right) \frac{I_{\mathrm{CH_2}}}{I_{\mathrm{MT}}} \cdot H_{\mathrm{MT}} \tag{6.2}$$

with the number of incoming events I_t for a certain target t and the area density τ_t, i.e., the number of scattering centers per area of the target. H_t describes the entries in the histogram of the γ-ray spectrum, and as such, the number of events for a certain fragment. The number of events for a pure proton target is then given by half the reconstructed H_2 target

$$H_{\mathrm{H}} = \frac{1}{2} H_{\mathrm{H_2}}. \tag{6.3}$$

Additionally, $H_{\mathrm{CH_2}}$ and H_{C} include reactions which did not take place in the target but in one of the detectors placed in the beam. If these events produce the same outgoing fragment, they are included in the cuts and contaminate the spectrum. To measure this contamination, dedicated runs with an empty (MT) target frame are recorded. The detected fragments in these runs cannot be produced in the target but stem from the setup itself. The reaction products for a target t can then be determined by subtracting the contribution from the empty target run

$$H_{t,\mathrm{corr}} = H_t - \frac{I_t}{I_{\mathrm{MT}}} \cdot H_{\mathrm{MT}}. \tag{6.4}$$

Unfortunately, only for setting 3 an empty target run with sufficient statistics is available. No empty target run is available for setting 4 and the one for setting 6 is too short to have enough events in the reaction channel of interest. Nevertheless, for setting 4 and 6 the targets were chosen in a way that their area density τ is almost equal, as one can see in Table A.2. This way the contributions of the empty target cancel each other in Equation 6.2. For knockout reactions

on a C target, however, this approach does not work and the empty target background needs to be estimated otherwise.

To calculate the exclusive cross sections for the excited states of the fragments, the fraction of the excited states of the overall number of the respective fragments needs to be determined. For this, the γ-ray spectra of the XB detector are compared to simulations for all expected states. The simulations and the experimental data are treated similarly to be able to compare them. In both cases, a proton and γ-ray NN addback and the Doppler correction are applied to the data. In case of QFS reactions on the reconstructed H target, a cut on events with exactly two reconstructed protons is performed. For the knockout reactions on the C target, no such cut on protons is done. Additionally, a time cut with a width of $\Delta t = 40\,\text{ns}$ is applied to remove background, mainly from the experimental data. The details of the applied algorithms and cuts are described in Section 4.4 and 4.5 for the experimental data and in Section 5.3 for the simulation.

In the next step, a sum of the simulated spectra of all possible states are fitted to the corresponding experimental spectrum. The fit is done simultaneously for the single and sum spectra for each reaction channel of interest. Single spectra are filled with the energy entries of all clusters separately. For the sum spectra, the energies of all clusters for a given event are summed. The features of the sum and single specta for both a direct decay and a higher lying state decaying via a cascade are discussed in Section 5.3.1 and shown in Figure 5.6. Since the two types of spectra are sensitive to the different decays in different ways, the ratio of the excited states can be determined more accurately by fitting both spectra simultaneously.

Furthermore, different fit algorithms are tested. The algorithms and their advantages and disadvantages are described in Section 4.6. Despite the different underlying statistical assumptions and distributions, the results of the presented algorithms agree with each other. To emphasis this, the proton amplitudes in Table 6.6 are determined using Neyman's, Baker and Cousins', and Bevington's χ^2 estimator. The values agree within their uncertainties. As mentioned before, only Neyman's χ^2_N estimator is able to cope with negative bin entries and, therefore, allows for goodness-of-fit testing. Hence, it is used for the fits shown in Figure 6.1 and 6.2 and used to determine the proton amplitudes and the cross sections. Nevertheless, the cross check with Baker and Cousins' and Bevington's χ^2 estimator supports the validity of the fit using Neyman's χ^2_N estimator.

The results of the fits for QFS reactions are illustrated in Figure 6.1. It shows the single and sum spectra for all three reactions of interest ^{17}N(p,2p)^{16}C, ^{19}N(p,2p)^{18}C, and ^{21}N(p,2p)^{20}C. Negative bin entries in the experimental spectra are caused by the subtraction of the C target contribution from the CH_2 target spectra. Especially for the reaction ^{21}N(p,2p)^{20}C, for which the number of events is small, it happens frequently that the reconstructed value is below 0. However, Baker and Cousins' and Bevington's χ^2 estimator cannot work with negative bin entries, which is why the negative entries were set to 0 to be able to still use these χ^2 estimators.

Uncertainties are given only for the experimental spectra. The simulated spectra are assumed to be precise since the number of simulated events is chosen accordingly. The simulations of the different states are depicted in different colors as described in the figure caption. The sum of all simulations is shown as well and can be compared with the experimental spectrum. As can be seen, the simulations describe the experimental data well. This is also reflected in the reduced $\chi^2_{\text{N,red}}$ values for Neyman's χ^2_N estimators given in Table 6.6.

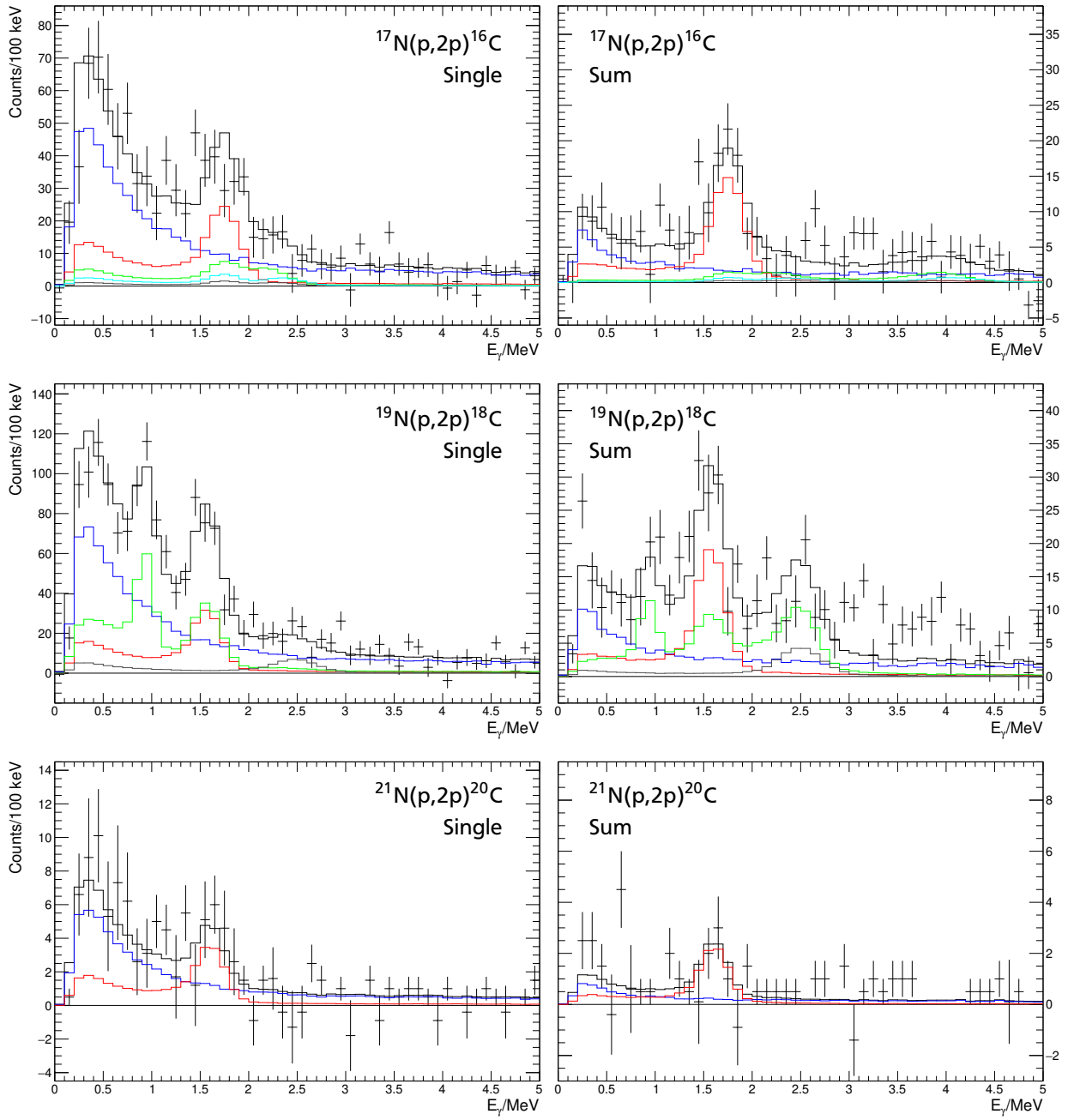

Figure 6.1: Simulated γ-ray single (left) and sum (right) spectra are fitted to the experimental data for the reconstructed H target with the *XB Sum* Tbit. The fits are shown for the reactions ^{17}N(p,2p)^{16}C (first row), ^{19}N(p,2p)^{18}C (second row), and ^{21}N(p,2p)^{20}C (third row). The experimental spectra are shown with black crosses. In all cases, the simulation of the background from the protons from the QFS reaction is depicted in blue, while the simulation of the first 2^+_1 state is shown in red. For the ^{17}N(p,2p)^{16}C reaction the simulation of the higher lying 2^+_2, 3^+, and 4^+ state are shown in green, turquoise, and grey. The higher lying state for the ^{19}N(p,2p)^{18}C reaction is simulated twice: The direct decay is depicted in grey, while the cascade is shown in green. The sum of all simulations is depicted in black. A cut on the proton multiplicity (#p=2) and a time gate is applied to the experimental and simulated data.

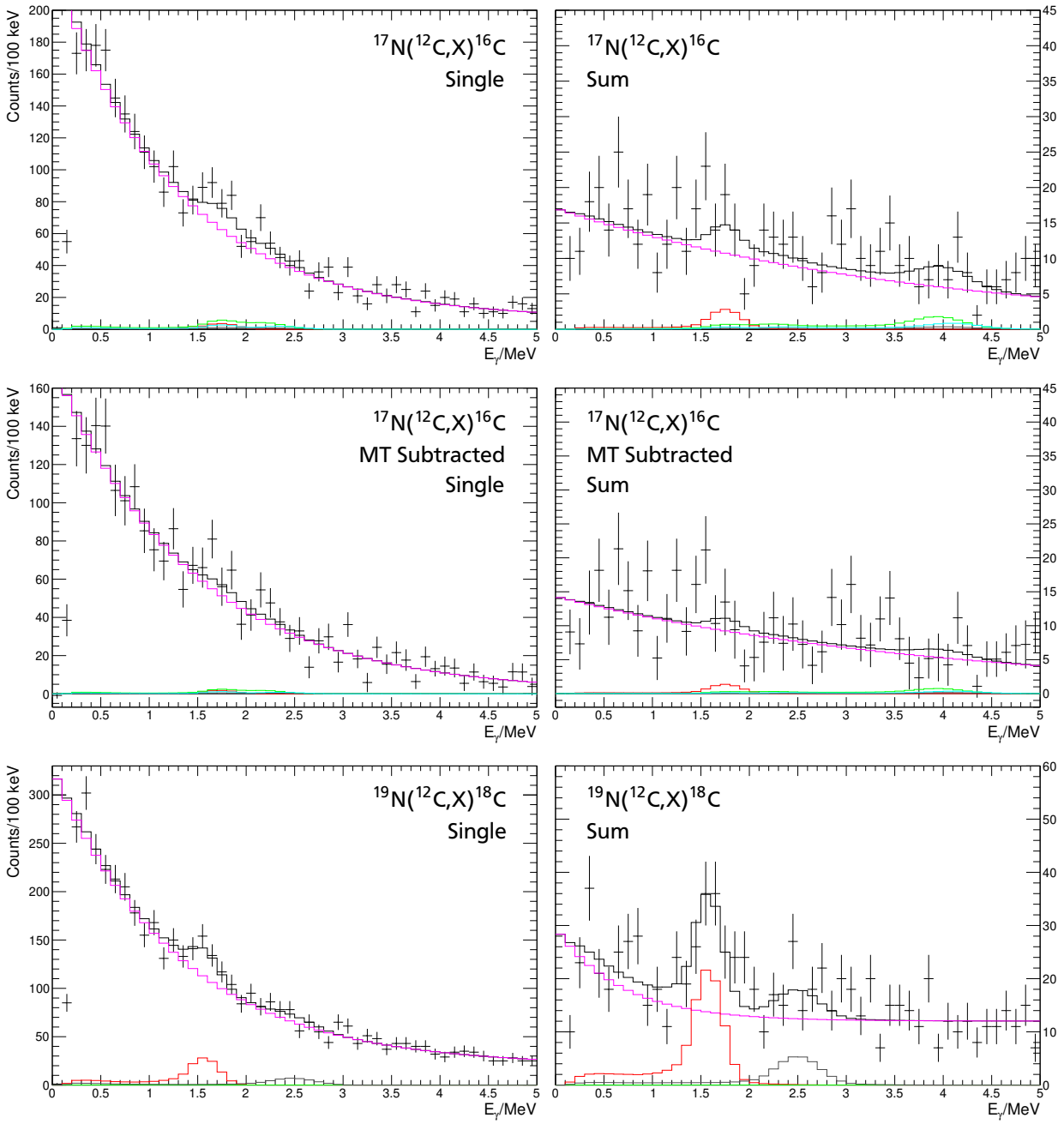

Figure 6.2: Simulated γ-ray single (left) and sum (right) spectra are fitted to the experimental data with the *XB Sum* Tbit. The fits are shown for the reactions ^{17}N(^{12}C,X)^{16}C for the C target (first row), the corrected C target (second row), and for ^{19}N(^{12}C,X)^{18}C for the C target (third row). The experimental spectra are shown with black crosses. In all cases, the simulation of the first 2^+_1 state is shown in red. For ^{17}N(^{12}C,X)^{16}C the simulation of the higher lying 2^+_2, 3^+, and 4^+ states are shown in green, turquoise, and grey. The higher lying state for the ^{19}N(^{12}C,X)^{18}C reaction is simulated twice: The direct decay is depicted in grey, while the cascade is shown in green. For knockout reactions the background (pink) is not simulated but estimated with an exponential function and a constant offset. The sum of the simulations and the background is depicted in black. A time gate is applied to the experimental and simulated data.

The low number of events for incoming ^{21}N leads to large uncertainties in the γ-ray spectra for the reconstructed H target. They translate into uncertainties of the fit, and as a consequence, into large uncertainties of the proton amplitude and cross sections. The low number of events is already visible in the incoming and outgoing ID plots in Figure A.8, A.9, and A.10. This is even more severe for the C target. In this case, it is no longer possible to extract γ-ray spectra, let alone fit simulations or calculate cross sections for knockout reactions.

Hence, the outcome of the fits for knockout reactions in Figure 6.2 shows only spectra for ^{17}N(^{12}C,X)^{16}C and ^{19}N(^{12}C,X)^{18}C but not for ^{21}N(^{12}C,X)^{20}C. For the ^{17}N(^{12}C,X)^{16}C reaction, two versions of the γ-ray spectra are shown. The first one shows the single and sum spectrum from the C target runs without any further corrections. The second set includes the subtraction of the background introduced by the in-beam detectors as described in Equation 6.4. The later spectra and the corresponding cross sections are labeled with C,corr. As one can see, the overall number of events in the spectra decreases due to this subtraction. However, no significant change in the peak height is visible. As mentioned before, the background subtraction can only be performed for incoming ^{17}N isotopes since only for this setting an empty target run is available. A way to reconstruct the background contribution for the remaining setting is discussed in Section 6.1 together with the results for the cross sections.

Furthermore, the C target spectra contain much more background in comparison to the reconstructed H target spectra. One reason is that the knockout reaction misses a clear proton signature. Thus, all events without any condition on the number of identified protons are taken into account. Because of that, the background is not simulated as for the QFS case, but an exponential function together with a constant offset is fitted to the data. Due to the large background and the bad energy resolution of the NaI crystals of XB, the peaks corresponding to the excited states are hardly visible. This is reflected in the large uncertainties of the exclusive knockout cross sections for the excited states in Section 6.1.

In addition to the cross sections and the proton amplitudes in the following sections, the branching ratio of the higher lying state in ^{18}C can be determined. Using the QFS data, a branching ratio of 22(8) % for the direct decay and 78(8) % for the decay via the first 2^+_1 state is measured. The lower statistics for the C target lead to large uncertainties, which prevent using the knockout data for a cross check. The values are in good agreement with 14(12) % for the direct decay and 86(12) % for the decay via the first 2^+_1 state determined from one-proton knockout reactions by Voss et al. [VBB$^+$12]. For the higher lying states in ^{16}C, the determination of the branching ratios is not possible. On one hand, no sum peaks at $E \approx 4$ MeV can be recognized in the single spectrum. However, a small contribution from the direct decays can remain undetected due to the bad energy resolution of XB resulting in very broad peaks. On the other hand, the three states lie very close to each other and cannot be distinguished with XB. Though, since Petri et al. [PPC$^+$12] did not observe direct decays with a higher sensitivity, the induced error by omitting them is negligible.

Finally, the number of simulated events is multiplied with the scaling factor from the fit to calculate the number of events in a given excited state. These values are the basis of the exclusive cross sections and the proton amplitudes in the following sections.

6.1 Cross Section

In general, the experimental cross section is given by the ratio of the number of outgoing and incoming particles taking into account the number of scattering centers in the target. For

incoming $^{A+1}$N isotopes impinging on a target t, the probability to produce a bound state of the corresponding ^{A}C isotope is given by the inclusive cross section

$$\sigma_{\mathrm{incl},t} = \frac{1}{\tau_t} \cdot \frac{O_t(^{A}\mathrm{C})}{I_t(^{A+1}\mathrm{N})} \tag{6.5}$$

with $A = 16$, $A = 18$, and $A = 20$ the mass number of the isotopes of interest. In this case, τ_t is the area density of the target t, describing the number of scattering centers per area. The values for the different targets and settings are listed in Table A.2. $O_t(^{A}\mathrm{C})$ describes the total number of outgoing ^{A}C, while $I_t(^{A+1}\mathrm{N})$ gives the number of incoming $^{A+1}$N. As described in Section 4.3.1, the number of incoming $^{A+1}$N nuclei can be approximated by the number of unreacted $^{A+1}$N particles behind the target. In case of QFS reactions, the number of the analyzed ^{A}C fragments includes a gate on two protons. Therefore, it needs to be corrected with the simulated efficiency to detect two protons, c.f. Section 5.3.2, to get the total number of events $O_t(^{A}\mathrm{C})$.

For the exclusive cross sections, the number of outgoing ^{A}C particles is determined with the help of the simulation described in Section 5.3.1. It is given by the number of simulated events multiplied with the scaling factor from the fit of the simulated to the experimental γ-ray spectra. As an example, the cross section of the 2^+_1 state is given by

$$\sigma_{2^+_1,t} = \frac{1}{\tau_t} \cdot \frac{O_{\mathrm{sim}}(^{A}\mathrm{C}, 2^+_1)}{I_t(^{A+1}\mathrm{N})} \tag{6.6}$$

with $O_{\mathrm{sim}}(^{A}\mathrm{C}, 2^+_1)$ the number of particles in the first excited 2^+_1 state extracted from the simulation. Since the simulations already include the XB efficiencies, they are not included explicitly. The cross sections for the higher lying excited states can be calculated accordingly, whereas the cross section of the ground state is calculated from the inclusive cross section subtracting all observed bound excited states

$$\sigma_{0^+_{\mathrm{g.s.}},t} = \sigma_{\mathrm{incl},t} - \sigma_{2^+_1,t} - \sigma_{\mathrm{higher\ states},t}. \tag{6.7}$$

The inclusive and exclusive cross sections for QFS reactions on the reconstructed H target are listed in Table 6.1. As mentioned before, a cut on exactly two protons identified in XB is applied. The corresponding γ-ray spectra shown in Figure 6.1 are fitted using Neyman's χ^2_{N} estimator. The uncertainties come from the target thickness, the number of recorded events, and the fit procedure.

The inclusive cross section for the ^{21}N(p,2p)^{20}C reaction can be compared with the cross section determined by Díaz Fernández et al. [FAPC$^+$18]. The authors analyzed the same experimental data set as me. They used two different reaction models for the description of the QFS reaction as input of their simulation. Hence, they extracted two different efficiencies for the proton detection, and with this, two different inclusive cross sections. My result agrees within its uncertainty with their cross section of $\sigma_{\mathrm{kin}} = 2.27(38)$ mb for the kinematical event generator, which corresponds to the event generator by Leonid Chulkov and Valerii Panin used in this thesis and introduced in Section 5.3. The difference between our results can mainly be explained by their larger proton detection efficiency, caused by a different energy threshold applied to identify the protons and slightly different parameters for the event generator as well as the simulation. For their second cross section of $\sigma_{\mathrm{F/A}} = 2.05(34)$ mb, they took an event generator which makes

Table 6.1: Cross sections in mb for QFS reactions on the reconstructed H target. Neyman's χ^2_N estimator is used for the determination of the exclusive cross sections.

	inclusive	0^+	2^+_1	higher-lying
^{17}N(p,2p)^{16}C	3.82(19)	2.83(20)	0.68(9)	0.32(8)
^{19}N(p,2p)^{18}C	3.66(14)	2.53(15)	0.45(7)	0.67(7)
^{21}N(p,2p)^{20}C	2.65(34)	1.87(38)	0.78(17)	-

Table 6.2: Cross sections in mb for knockout reactions on the C and the corrected C target. For the ^{19}N(^{12}C,X)^{18}C reaction no empty target run is available. The values marked with * are estimated as explained in the text using the empty target cross section for the ^{17}N(^{12}C,X)^{16}C reaction. For the ^{21}N(^{12}C,X)^{20}C reaction not enough statistics are available. Neyman's χ^2_N estimator is used for the determination of the exclusive cross sections.

	target	inclusive	0^+	2^+_1	higher-lying
^{17}N(^{12}C,X)^{16}C	C	9.8(18)	9.4(18)	0.11(9)	0.28(13)
	C,corr	7.7(20)	7.5(20)	0.05(10)	0.12(14)
^{19}N(^{12}C,X)^{18}C	C	9.4(14)	8.8(15)	0.45(8)	0.17(54)
	C,corr	7.4(14)*	6.8(15)*	0.45(8)*	0.17(54)*

use of the Faddeev/AGS reaction framework. With this event generator, the proton detection efficiency is even larger and, therefore, the cross section smaller. The question of which event generator is more reliable is at the moment unsolved.

The results for knockout reactions on the C target are shown in Table 6.2. Again, Neyman's χ^2_N estimator is used for fitting the spectra in Figure 6.2. The uncertainties stem from the uncertainty in the target thickness, the number of recorded events, and the fit procedure. As mentioned before, the reaction channel ^{21}N(^{12}C,X)^{20}C does not have enough events to fit the γ-ray spectra reliably. Additionally, no clean trigger condition is connected to knockout reactions. As explained in Section 3.4, the reactions of interest are usually connected to a certain Tbit. Unfortunately, this is not the case for knockout reactions. In contrast to QFS reactions, for which two protons are expected, for knockout reactions it is not guaranteed that a high-energy charged particle, which can be detected by XB, is emitted together with the fragment. Therefore, the reaction channels to the ground state and to the excited states are connected to different trigger conditions. On one hand, the excited states emit γ rays with an energy of at least 900 keV, which will be detected by XB. In combination with the detection of the outgoing ^{A}C fragment, the *XB Sum* Tbit is set for these events. On the other hand, particles in the ground state do not emit any γ rays. For these events either the downscaled *Fragment* Tbit or – in case that a background event triggers XB – the *XB Sum* Tbit is set. Thus only the *Fragment* Tbit gives a reliable number for the ground state of the reaction product. Due to the downscaling of this Tbit and the consequential small number of events, the inclusive cross section as well as the cross section for the ground state exhibit large uncertainties.

To reconstruct the cross section of the reactions on the C target, the contribution from the detectors in the beam line to the reaction channel needs to be determined. For setting 3, for which an empty target run with sufficient statistics is available, this is done using Equation 6.4. The results for both the uncorrected and corrected cross sections are listed in Table 6.2. As one can see in Figure 6.2, the spectrum is dominated by the background and the excited states are hardly visible. Thus, the cross sections for the excited states display large uncertainties. Comparing the exclusive cross sections, one recognizes that the corrected cross sections are smaller than the uncorrected ones. However, the corrected results agree within their uncertainties with 0 and with the uncorrected values.

For the ^{19}N(^{12}C,X)^{18}C reaction the situation is different. No empty target run is available for setting 4. Therefore, the contribution from the in-beam detectors needs to be estimated otherwise. This is done for the inclusive cross section as follows. In general, the corrected cross section $\sigma_{\mathrm{C,corr}}$ is calculated by subtracting the empty target cross section σ_{MT} from the C target cross section σ_{C}

$$\sigma_{\mathrm{C,corr}}(^{A}\mathrm{C}) = \sigma_{\mathrm{C}}(^{A}\mathrm{C}) - \sigma_{\mathrm{MT}}(^{A}\mathrm{C}). \tag{6.8}$$

As a next step, I assume that the inclusive cross section in the detectors, which are built either from plastic or silicon, scales with the same factor as the one for the C target. This can be expressed in the relation

$$\frac{\sigma_{\mathrm{C,corr}}(^{18}\mathrm{C})}{\sigma_{\mathrm{C,corr}}(^{16}\mathrm{C})} = \frac{\sigma_{\mathrm{MT}}(^{18}\mathrm{C})}{\sigma_{\mathrm{MT}}(^{16}\mathrm{C})}. \tag{6.9}$$

Combining Equation 6.8 and 6.9, the inclusive cross section for ^{18}C can be cleaned from the influence of the in-beam detectors. The corrected cross section is given by

$$\sigma_{\mathrm{C,corr}}(^{18}\mathrm{C}) = \sigma_{\mathrm{C}}(^{18}\mathrm{C})\left(1 - \frac{\sigma_{\mathrm{MT}}(^{16}\mathrm{C})}{\sigma_{\mathrm{C}}(^{16}\mathrm{C})}\right) \tag{6.10}$$

with the cross section for the empty target run of ^{16}C given by $\sigma_{\mathrm{MT}}(^{16}\mathrm{C}) = 2.1(8)\,\mathrm{mb}$. The result is listed in Table 6.2.

However, this method is not applicable to the exclusive cross sections of the excited states. First of all, the level schemes of ^{16}C and ^{18}C are different. Therefore, the γ-ray spectrum of ^{16}C cannot be used to estimate the empty target contribution for the excited states of ^{18}C. Furthermore, the influence of the empty target run on the excited states of ^{16}C is inconclusive, as described above. Thus, as a very rough estimation, the uncorrected exclusive cross sections for the excited states are taken as an upper limit. Afterwards, the exclusive cross section for the ground state is calculated by subtracting the exclusive cross sections of the excited states from the inclusive cross section. Since the excited states are estimated with their maximum value, the corrected ground state cross section corresponds to the minimum value.

6.1.1 Comparison with Theoretical Cross Section

Carlos Bertulani [Ber17] calculated the exclusive cross sections for both QFS and knockout reactions using the Glauber theory approach introduced in Section 2.1. The calculations for the

Table 6.3: Theoretical cross sections in mb for QFS reactions calculated by Carlos Bertulani [Ber17].

	$p_{1/2}$	$p_{3/2}$	
occupation number	1	4	1
^{17}N(p,2p)^{16}C	6.171	23.716	5.929
^{19}N(p,2p)^{18}C	5.267	20.773	5.193
^{21}N(p,2p)^{20}C	4.554	17.832	4.458

Table 6.4: Theoretical cross sections in mb for knockout reactions calculated by Carlos Bertulani [Ber17].

	$p_{1/2}$	$p_{3/2}$	
occupation number	1	4	1
^{17}N(^{12}C,X)^{16}C	19.19	69.40	17.35
^{19}N(^{12}C,X)^{18}C	16.00	60.04	15.01
^{21}N(^{12}C,X)^{20}C	13.58	50.44	12.61

QFS reaction cross sections are explained in detail in Section 2.1.2. The densities of the nuclei in Equation 2.28 are determined with HF calculations using the SLy5 interaction [CBH$^+$98] and isovector surface pairing. The wave function of the proton in Equation 2.29 is calculated using a phenomenological potential consisting of a Woods-Saxon central potential, a spin-orbit term, and the Coulomb potential. The potential is adjusted to the binding energy of the removed particle. For the $1p_{1/2}$ orbit the binding energy is equivalent to the proton separation energy S_p assuming that the separated proton comes from the $1p_{1/2}$ orbit. The experimental values are 13.11 MeV for ^{17}N, 16.35 MeV for ^{19}N, and 19.6 MeV for ^{21}N [WAW$^+$12]. The binding energies of the $1p_{3/2}$ protons are estimated with a simple shell model calculation. The energy difference of the $1p_{3/2}$ and $1p_{1/2}$ proton orbits from the calculation together with the binding energy of the $1p_{1/2}$ orbit gives the energy required to remove a proton from the $1p_{3/2}$ orbit. The resulting cross sections are listed in Table 6.3. The calculations were originally done with an occupation number of 1 for the $1p_{1/2}$ and 4 for the $1p_{3/2}$ orbit. For comparison, the cross sections for an occupation number of 1 for the $1p_{3/2}$ orbit are shown as well.

The calculations for the knockout reaction cross sections are explained in detail in Section 2.1.1. As for QFS reactions, the densities in Equation 2.16 are taken from HF calculations. The same is true for the wave function $\psi_{lm}(\mathbf{r})$, which is calculated with the phenomenological potential given in Equation 2.19 adjusted to the binding energy of the removed particle. In this case, the occupation number for both the $1p_{1/2}$ and the $1p_{3/2}$ orbit is 1 in the calculation. For comparison, the cross sections are given for an occupation number of 4 for the $1p_{3/2}$ orbit as well.

These eikonal cross sections are now compared to the experimental ones in Table 6.1 and 6.2. For this, I assume that the removal of the proton from the $1p_{1/2}$ orbit leads to the 0^+ ground state in the ^{A}C fragment. The removal of one of the protons in the $1p_{3/2}$ orbit leads in a simple shell model picture either to a 2^+ or a 1^+ excited state. Since until now no 1^+ bound state was measured in neutron-rich, even-even carbon isotopes, the theoretical cross section for the

Table 6.5: Spectroscopic factors for QFS and knockout reactions. The experimental QFS cross sections are taken from Table 6.1. For knockout reactions the corrected cross sections are taken from Table 6.2. The values marked with * are estimates as explained in the previous section. The theoretical cross sections were calculated by Carlos Bertulani [Ber17] and are taken from Table 6.3 and 6.4 for an occupation number of 1 for both the $1p_{1/2}$ and the $1p_{3/2}$ orbit.

	state		σ_{exp}/mb	σ_{theo}/mb	S_{exp}	C^2S
^{17}N(p,2p)^{16}C	0^+	$1p_{1/2}$	2.83(20)	6.171	0.459(32)	1
	2^+	$1p_{3/2}$	0.68(9)	5.929	0.115(15)	0.25(4)
^{19}N(p,2p)^{18}C	0^+	$1p_{1/2}$	2.53(15)	5.267	0.480(28)	1
	2^+	$1p_{3/2}$	0.45(7)	5.193	0.087(13)	0.18(3)
^{21}N(p,2p)^{20}C	0^+	$1p_{1/2}$	1.87(38)	4.554	0.411(83)	1
	2^+	$1p_{3/2}$	0.78(17)	4.458	0.175(38)	0.43(16)
^{17}N(^{12}C,X)^{16}C	0^+	$1p_{1/2}$	7.5(20)	19.19	0.39(10)	1
	2^+	$1p_{3/2}$	0.05(10)	17.35	0.003(6)	0.25(4)
^{19}N(^{12}C,X)^{18}C	0^+	$1p_{1/2}$	6.8(15)*	16.00	0.43(9)*	1
	2^+	$1p_{3/2}$	0.45(8)*	15.01	0.030(5)*	0.18(3)

removal of a proton from the $1p_{3/2}$ orbit is compared to the cross section of the first excited 2^+_1 state. The removal of one of the two protons in the $1s_{1/2}$ orbit is not covered in this thesis. Since they are deeply bound, it is expected that their removal leads to an unbound state in the ^{A}C fragment.

In Table 6.5 the experimental and theoretical cross sections are summarized. In addition, the experimental spectroscopic factors introduced in Equation 2.3 are calculated. From the occupation of the involved orbits depicted in Figure 1.1, one expects a spectroscopic factor of 1 for the proton removal from the $1p_{1/2}$ orbit. For the removal from the $1p_{3/2}$ orbit, the spectroscopic factor depends on the model that is used. I assume that the first excited 2^+_1 state is a mixed state of a pure proton and a pure neutron excitation as described in Section 2.2.2. Furthermore, a proton in the $1p_{1/2}$ orbit and a proton in the $1p_{3/2}$ orbit couple in only five out of eight cases to the total momentum 2. Since four protons populate the $1p_{3/2}$ orbit, one expects a spectroscopic factor of $\beta^2 \times 4 \times \frac{5}{8} = \beta^2 \times \frac{5}{2}$. The proton amplitude is known from the analysis presented in Section 6.2 and given in Table 6.6. The expected spectroscopic factor is denoted C^2S.

As one can observe, the experimental spectroscopic factors differ systematically from the expected ones for all investigated reactions. For the QFS reactions, the ratio of the expected and the experimental spectroscopic factor is the same for the 0^+ ground state and the first excited 2^+_1 state. This is expected since $C^2S(2^+_1)$ includes the proton amplitude which itself includes the theoretical cross sections. The discrepancy of the spectroscopic factors shows that correlations are missing in the simple two-state mixing model. However, even more sophisticated theoretical calculations with realistic interactions usually do not describe the spectroscopic factors correctly. The correlations that are missing in these calculations can be sorted into two groups: Due to the truncation of the model space in shell model calculations, multi particle-hole excitations as

well as coupling to collective excitations are not included. If such long-range correlations are included in the calculations, experimental spectroscopic factors can be reproduced as shown, e.g., by Carlo Barbieri [Bar09]. In addition, realistic interactions are usually based on a one-pion exchange model and thus include only low to medium momentum transfer. The high-momentum, short-range repulsive core of the nuclear interaction is then added either as heavy meson exchange terms or as a contact term [ME11]. Furthermore, since the inclusion of the high-momentum part is computationally challenging, interactions with a soft core are often used, which have difficulties describing short-range pairs. However, in cases in which the soft potential is determined by a unitary transformation, as, e.g., the Unitary Correlation Operator Method (UCOM) and the Similarity Renormalization Group (SRG) approach [RNF10], short-range correlations can be recovered by transforming the operators as well [NFH15]. Electron scattering measurements show that such short-range correlated pairs account for $\approx 20\,\%$ of the nucleons in ^{12}C and that the correlation is dominated by the tensor force [SSM$^+$08]. Since the two-state mixing model is a simple model that does not take all these correlations into account, the discrepancy of the experimental and the expected spectroscopic factors is expected.

For the knockout reactions the picture looks different. While the ratios of the experimental and the expected spectroscopic factors for the 0^+ ground state agree with the ones from (p,2p) reactions within their uncertainties, the ratios for the first excited 2^+_1 states match neither those for the QFS reactions nor those for the 0^+ states. However, the comparison is hardly possible due to several reasons mentioned earlier. First of all, because of the missing reaction trigger, the exclusive cross section of the first excited 2^+_1 state is calculated with a different trigger than the one for the 0^+ ground state. In addition, the missing reaction trigger leads to a large background in the γ-ray spectra. The peaks corresponding to the 2^+_1 states are hardly visible in the spectra and the fits have large uncertainties. Furthermore, for the ^{19}N(^{12}C,X)^{18}C reaction no empty target run is available. The reconstructed cross sections, especially for the excited states, are only an estimation. Their uncertainties include those from error propagation but none from systematic uncertainties, e.g., those introduced by the assumption in Equation 6.9. With this in mind, the results for the knockout reactions, and especially those of the 2^+_1 states, should be discussed with care.

6.2 Proton Amplitude

As described in Section 2.2.2, the proton amplitude can be calculated with Equation 2.48 as long as the theoretical cross sections for the two states $\sigma_{\text{theo}}(1p_{3/2})$ and $\sigma_{\text{theo}}(1p_{1/2})$ are known. These cross sections for the $1p_{1/2}$ and the $1p_{3/2}$ orbit were calculated by Carlos Bertulani [Ber17] as presented in the previous section. Since the area density of the target τ_t as well as the number of incoming $^{A+1}$N particles is the same for the cross section to the ground state and the excited states, the proton amplitude can then be calculated by

$$\beta^2 = \frac{2}{5} \times \frac{O_t(^A\text{C}, 2^+_1)}{O_t(^A\text{C}, 0^+_{\text{g.s.}})} \times \frac{\sigma_{\text{theo}}(1p_{3/2})}{\sigma_{\text{theo}}(1p_{1/2})}. \tag{6.11}$$

As described before, the number of ^{A}C fragments in the 2^+_1 state is extracted from the simulations, while the number of particles in the 0^+ ground state can be calculated by the number of particles in excited states subtracted from the total number of ^{A}C isotopes

$$O_t(^A\text{C}, 0^+_{\text{g.s.}}) = O_t(^A\text{C}) - O_t(^A\text{C}, 2^+_1) - O_t(^A\text{C}, \text{higher states}). \tag{6.12}$$

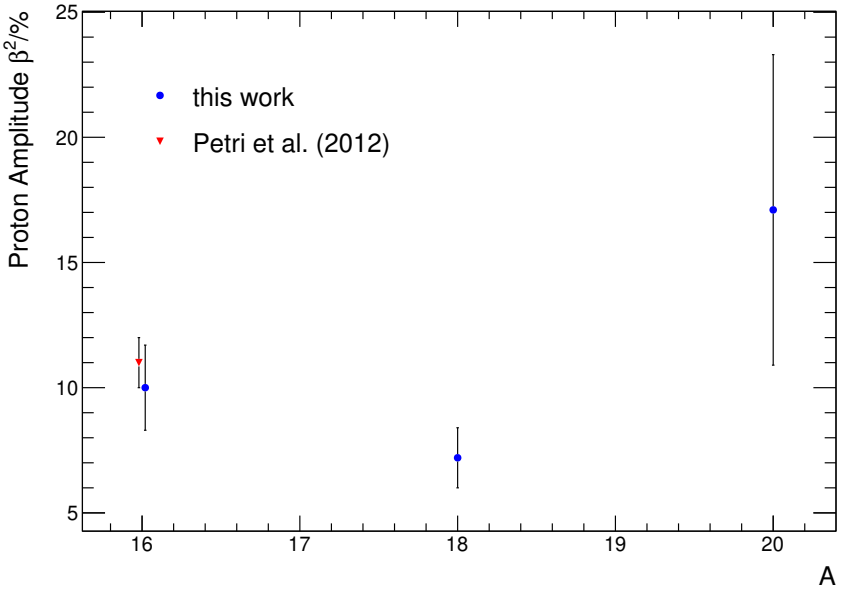

Figure 6.3: Proton amplitude for the reconstructed H target. Neyman's χ^2_N estimator is used for fitting. The value for ^{16}C was already measures by Petri et al. [PPC$^+$12].

The resulting proton amplitudes are listed in Table 6.6 for ^{16}C, ^{18}C, and ^{20}C. The theoretical cross sections σ_{theo} for an occupation number of 1 are listed in Table 6.3. The number of particles in the different excited states are extracted from the fit of the simulated to the experimental spectra shown in Figure 6.1. The fit is performed using different χ^2 estimators described in Section 4.6. The results from all three estimators agree with each other within their uncertainties. However, due to the negative bin entries originating from the subtraction of the C target contribution, only Neyman's χ^2_N estimator can be used for the goodness-of-fit testing. Therefore, these results are taken as the final ones and are depicted in Figure 6.3. The proton amplitude of $\beta^2(^{16}\text{C}) = 11(1)\,\%$ by Petri et al. [PPC$^+$12] introduced in Section 2.3 is depicted as well. My result for ^{16}C agrees with this value within its uncertainty.

In addition, a trend to a larger proton amplitude for the more neutron-rich ^{20}C is observed. It matches the expectation based on the increasing $B(E2; 2^+_1 \rightarrow 0^+_{\text{g.s.}})$ strength in Figure 1.2, which can be explained by an increase in the proton contribution. With $\beta^2(^{20}\text{C}) = 16.8(61)\,\%$ the proton amplitude is not as large as expected by Macchiavelli et al. [MPF$^+$14] from the calculation of the $B(E2)$ in the seniority scheme, but it is in agreement with the overall trend. Petri et al. [PFM$^+$11], e.g., reproduced the increase in $B(E2)$ strength for ^{20}C with a shell model

Table 6.6: Proton amplitude for the reconstructed H target for different χ^2 estimators. Due to the negative bin entries originating from the subtraction of the C target contribution, no $\chi^2_{\text{BC,red}}$ for goodness-of-fit testing can be given for Baker and Cousins' estimator.

	Neyman's	$\chi^2_{\text{N,red}}$	Baker & Cousins'	$\chi^2_{\text{BC,red}}$	Bevington's
^{17}N(p,2p)^{16}C	10.0(17)	1.32	10.6(13)	-	10.9(13)
^{19}N(p,2p)^{18}C	7.2(12)	2.48	7.2(9)	-	7.2(9)
^{21}N(p,2p)^{20}C	17.1(62)	0.80	16.3(56)	-	17.9(61)

calculation in the $p-sd$ shell model space using harmonic oscillator wave functions and the WBT interaction [WB92] observing an increase in the proton matrix element. This increase is clearly visible in my data. It fits to the expectation that the gap between the $1p_{3/2}$ and the $1p_{1/2}$ proton orbit decreases for a larger number of neutrons in the $1d_{5/2}$ orbit as explained in detail in Section 2.3. The decreasing gap leads to a higher probability for proton excitations and with this to a higher proton amplitude as shown in Figure 6.3 by my analysis. However, due to the large uncertainties caused by the low number of events, the proton amplitude for ^{20}C is almost compatible with the one for ^{16}C. Therefore, a more precise measurement needs to be performed to validate the measured increase.

7 Detector Characterization

In the experimental campaign S393 two different detectors were used to measure the energy loss and the position of the incoming and outgoing beam simultaneously: the PSP in the beginning of the setup and the four SSDs around the target area. Both detectors have several disadvantages like, e.g., the expensive calibration procedure with dedicated pixel runs for the PSP or a large number of channels in case of the SSDs. Therefore, a different detector design is tested for the future R^3B setup.

In this chapter, I want to summarize the tests done and the results achieved. First of all, the detector and its working principle is introduced, before I outline the setup which was used to test the detectors. Afterwards, the calibration procedure is described in detail. The result of an α-source measurement, as well as the ones from an in-beam experiment at KVI-CART, are presented. The dependency of the position and energy resolution on the filter settings of the electronic readout is investigated. The results are interpreted in terms of ballistic deficit and pulse shape analysis. Finally, the energy and position resolution is compared with a previous measurement at GSI.

7.1 Detector Design

Like the PSP and SSDs, the new detector is a semiconductor detector made out of silicon. An overview over semiconductors, their working principle, and their applications can be found in [Leo94, Kno00]. Semiconductor materials have a relatively small gap between their valence and conduction band. Thus, electrons can be excited easily, e.g., thermally or by ionizing radiation. The excited electrons, as well as the holes produced in the valence band, can move freely in the material and contribute to the conduction.

If impurities are added, the conduction via holes or electrons can be prioritized. This process is called doping. In case of impurities with one valence electron more than the semiconducting material, energy levels close to the conduction band filled with electrons are added. These electrons can then be excited easily, but the produced holes are not able to move due to the localization of the impurities. Therefore, the majority of the charge carriers are electrons and the material is called n-type. Impurities with one electron less, on the other hand, add empty energy levels close to the valence band. The electrons which are excited into these levels are trapped due to their localization and the majority charge carriers are the holes in the valence band. This type of semiconductor is called p-type.

If a p-type and a n-type semiconductor are put together, a depletion zone is formed, in which the holes from the p-type material and the electrons from the n-type material combine. Due to this shift in electrons and holes in the material, an electric field is formed, which stops the diffusion process eventually. In the depletion volume no free charge carriers are left. Therefore, this region is ideal for the detection of ionizing radiation. The produced electron-hole pairs are separated by the electric field and can be measured afterwards. The small natural depletion zone, and with that the active volume of the detector, can be enlarged by applying an external reverse bias. Since the number of electron-hole pairs is proportional to the energy loss of the

traversing particle, semiconductors are used to determine the charge of the particle as explained before in Section 3.2.

Additionally, semiconductors can be used for position measurement. One way to do this is the segmentation of the surface into very thin strips as it is done for the SSDs introduced in Section 3.3. A second way is to add a resistive layer on the surface and to use the resistive charge division to determine the position of the hit. The detectors tested in this chapter are based on this principle. They are segmented into strips with each strip read out on both ends. In Figure 7.1 a) the lateral view of such a strip is sketched. The charge carriers are split up due to the resistance of the surface. Depending on the distance x between the hit and the anode and the length L of the strip, a charge Q_{anode} is collected

$$Q_{\text{anode}} = E\frac{x}{L} \tag{7.1}$$

with E the total energy deposited in the detector. The position can then be calculated using the charge collected at both ends of a strip Q_1 and Q_2

$$x = \frac{L}{2} \cdot \frac{Q_2 - Q_1}{Q_1 + Q_2} \tag{7.2}$$

with the point of origin in the middle of the detector, the position within the range $[-L/2, L/2]$ and the total energy loss in the strip being

$$E = Q_1 + Q_2. \tag{7.3}$$

Using the resistive charge division makes a position resolution of $\approx 100\,\mu$m possible with a relatively small number of electronic channels. Additionally, the position in the second dimension can be determined by the strip that was hit. The resolution of this measurement is given by the width of the strip w as $w/\sqrt{12}$.

However, a good position measurement not only in one but in two dimensions is needed for the future R^3B setup. Therefore, a detector was designed by Micron Semiconductor Ltd which has strips on both sides with the strips on the back perpendicular to the strips on the front. The Micron X5 detector has an active area of $(9.57 \times 9.57)\,\text{cm}^2$ and is available in three thicknesses: $100\,\mu$m, $200\,\mu$m, and $300\,\mu$m. The detectors tested in this thesis are $210\,\mu$m and $211\,\mu$m thick. Both are p-type detectors, i.e., the p-type material in the depletion zone is much thicker than the n-type material which, on the other hand, is more strongly doped. The detector has 32 strips on each side, which have a width of 2.99 mm and are read out on both ends. The front as well as the back has a resistive surface and can therefore be used to determine the position according to Equation 7.2. The technical drawing of the detector is depicted in Figure 7.1 b).

7.2 Setup

The Micron X5 detectors were tested at KVI-CART in March 2018 during the beam time 17M02 dedicated to the "Characterization of heavy-ion tracking detectors for R^3B". The beam time was used to test several prototype detectors with an ion beam. The tested detectors include the LOS detector – a new version of the POS detector –, several fiber detectors of different sizes with

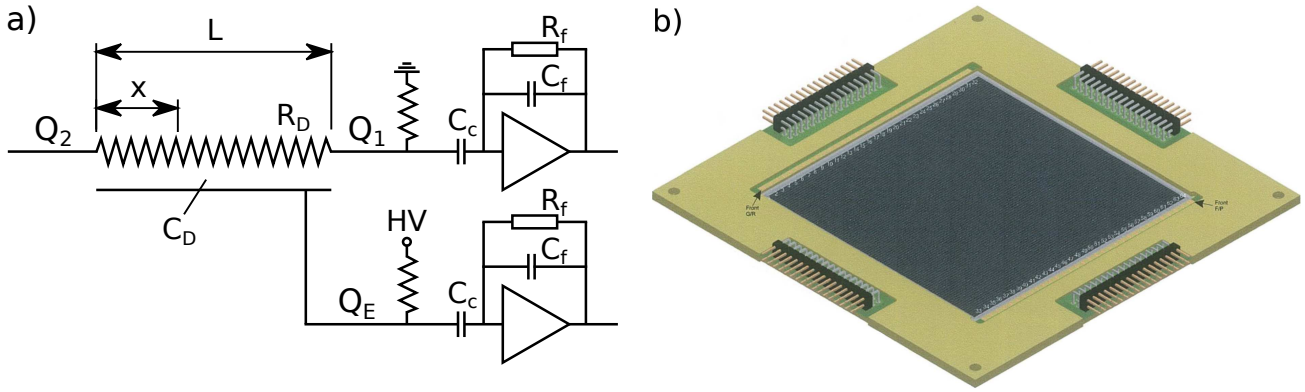

Figure 7.1: a) Sketch of a 1-dimensional position sensitive semiconductor detector deploying the resistive charge division. The lateral view shows a detector with a resistive layer on one side of the strip and a normal contact on the opposite side. The collected charge at the anodes depends on the position *x* at which the strip is hit, while the signal at the non-resistive side is proportional to the energy loss *E*. Additionally, the AC coupling to a charge sensitive preamplifier is depicted. The sketch is adapted from [Læg79]. b) The technical drawing of the Micron X5 detector shows the 32 strips on the front of the detector which are read out on both ends. The 128 channels in total, together with the connections to the field plates and guard rings, are combined in four 34 pin connectors. The drawing is taken from [Mic15].

different types of fibers and with different readout systems, a prototype for a new TOF wall for the proton arm of the future R^3B setup, and the Micron X5 detectors.

All detectors were placed after each other in the beam line and were tested simultaneously. Their arrangement is shown in Figure 7.2. The beam entered the setup from the left. In the beginning, a collimator was placed to limit the beam spot to the size of the smallest detector. In some of the runs, an additional sieve slit reduced the beam to a few small spots. Those runs are not used in the presented analysis. Therefore, the orientation of the holes in the sieve slit is not shown. The first detectors in the setup were the start detector LOS and a small fiber detector. They were placed together in a light tight black box. The next detector was a Micron X5 detector placed inside a vacuum chamber. Afterwards, a small fiber detector was read out using Multi-Pixel Photon Counters (sMPPCs) instead of the usual PSPMs. The brass collimator placed behind the MPPC fiber detector belongs to the original setup at KVI-CART. It had no purpose in our setup but did not interfere with our measurement. After the collimator, three large fiber prototypes and the proton TOF wall were placed. They could be moved in the x direction to be able to test and calibrate a wide range of the large sensitive area. Fiber5 and Fiber4 as well as Fiber6 and the proton TOF wall were placed on a x table each and could be moved together. All detectors except the Micron X5 detector were placed in air.

The detectors were tested with a ^{12}C beam with an energy of 90 AMeV. A second beam of protons with an energy of 190 MeV was mainly used to test the TOF wall. The energy loss in the Micron X5 detector was too small to reliably differentiate the proton signals from the noise. Hence, the number of recorded events is too small to, e.g., systematically analyze different filter settings. Therefore, results from the proton beam will not be presented in this thesis.

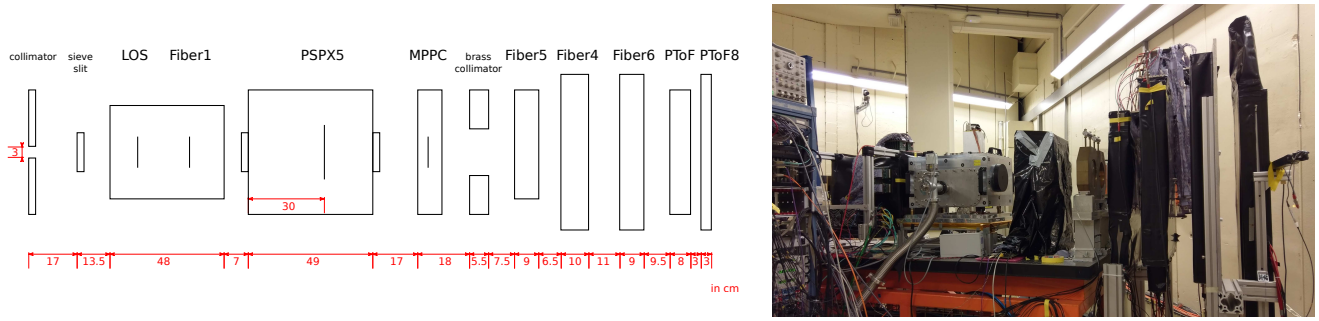

Figure 7.2: Setup for the detector test at KVI-CART. The sketch (left) and the photo (right) of the setup show all involved detector systems. The beam entered the experimental area from the left. A Micron X5 detector was placed in the vacuum chamber in the first half of the setup. Photo courtesy of Kathrin Göbel.

As mentioned before, the Micron X5 detector was mounted inside a vacuum chamber. The strips on the front of the detector were oriented in the y direction, while the strips on the back were oriented in the x direction. The 64 channels of the front and the back were each guided via a feed-through to two mesytec MPR-32 preamplifiers with an energy range of 25 MeV placed on the outside. With the feed-through, the channels of the detector were mapped to the channels of the preamplifier. The differential output of the preamplifiers were connected to the Front-End Board with optical link EXtension 3b (FEBEX3b) ADC, which was read out using the MBS DAQ. The front of the detector was biased via the preamplifiers using a mesytec MHV-4 High Voltage (HV) module. A sketch of the readout chain and a photo of the detector inside the vacuum chamber can be found in Figure 7.3. Information about and manuals of the mesytec preamplifier and high voltage module can be found on the mesytec webpage [mGCK18b, mGCK18a]. General information about the FEBEX3b system and the MBS DAQ can be found on the webpage of the experiment electronics department at GSI [feb18, mbs18]. Usually, the measurements were done with a vacuum pressure of $\approx 5 \times 10^{-4}$ mbar. Only for the comparison of the detector performance, the vacuum chamber was vented once during the beam time at KVI-CART and data were taken within air.

The charge collected at an anode was converted by the charge sensitive preamplifier to a signal whose height is proportional to the original charge. Then the FEBEX3b ADC determined the pulse height. To do so, it applies a moving-average filter to the incoming pulses. For this filter the pulse height of the signal is summed up over two time intervals with the length $w \cdot \Delta t$. The time intervals start at two different times t_1 and $t_2 = t_1 + (w + g) \cdot \Delta t$ with $g \cdot \Delta t$ the time span between them. Δt is the time between two samples of the pulse shape. In case of the FEBEX3b ADC, which has a sampling rate of 50 MHz, it is $\Delta t = 20$ ns. For given values of the interval (*window*) length w and the time span (*gap*) g between them, the difference of the second and the first sum is then the height of the filter signal as a function of the time t_1. Figure 7.4 shows an original pulse shape of the preamplifier together with the filter signals for four different settings. The signal of the moving-average filter has the shape of a trapeze with a flat top with a length corresponding to the gap g, while the rise and decay time of the signal corresponds to the window length w. Due to the noisy original pulse shape, the baseline of the filter signal fluctuates. This effect can be reduced with longer integration times w. Longer integration times are not shown since the recorded pulse shape only allowed for filter settings with $2 \cdot w + g < 70$. The intrinsic filter of the FEBEX3b ADC, however, can handle filter settings up to $2 \cdot w + g < 1000$.

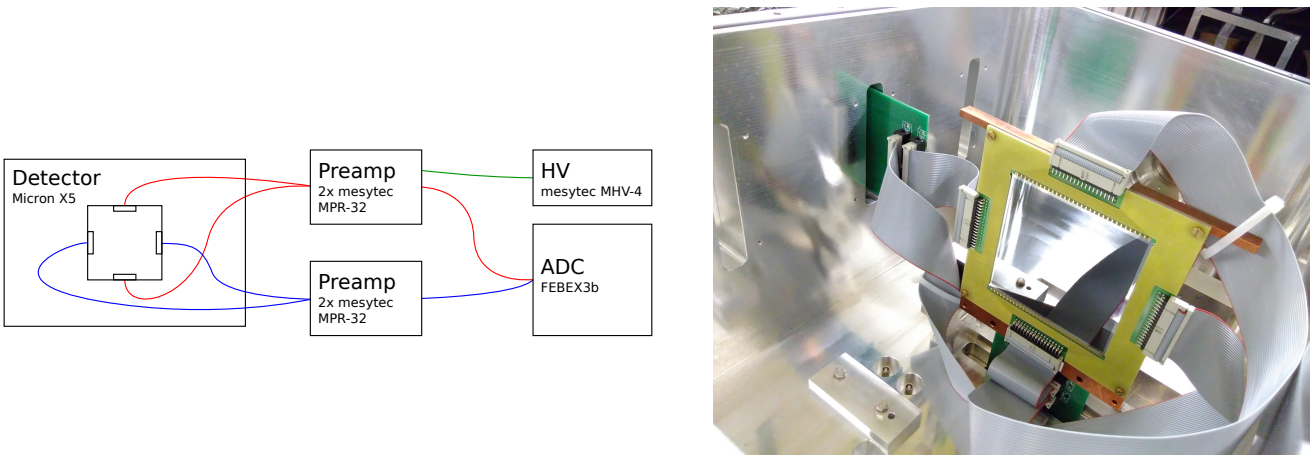

Figure 7.3: Sketch (left) of the Micron X5 setup during the detector tests at KVI-CART and GSI, and photo (right) of the Micron X5 detector in the vacuum chamber. The detector signals were amplified with four mesytec MPR-32 preamplifiers. The amplified signals were then digitized using the FEBEX3b ADC. The detector was biased via two preamplifier modules using a mesytec MHV-4 HV module.

After all, the height of the filter signal is determined to obtain the collected charge. Since the FEBEX3b ADC simply takes the highest point of the filter signal, a flat top without any spikes is necessary for a good resolution.

Additionally, the FEBEX3b ADC provides a trigger signal for the DAQ. A second moving-average filter with dedicated settings – $w = 4$ and $g = 8$ for the measurements at KVI-CART and $w = 8$ and $g = 8$ for the α-source measurements at GSI – determines the pulse height. If this value is above a channel specific threshold, the trigger signal is released and the data of the corresponding channel are recorded. Although a trigger signal from the start detector LOS was provided during the beam time at KVI-CART, the data presented in this thesis were taken with the trigger from the FEBEX3b ADC. This way, the data taking was independent of the tests done with the other detector systems. However, during runs in which the fiber detectors and the proton TOF wall were moved, the noise induced by the drive of the x table resulted in constant triggering of all channels. As a result, a lot of useless data were written to disk. Since it was possible to eliminate these additional entries in the analysis, this did not pose a problem. Only for the proton beam the use of the FEBEX3b ADC trigger was not possible and the trigger provided by the main DAQ was used. In this case, due to the small energy of only $\approx 0.2\,\mathrm{MeV}$ deposited by the protons, the actual signals were hardly distinguishable from noise even in the analysis.

The recorded data were analyzed either with *ucesb* or R3BRoot. *ucesb* [Joh18] is used to unpack the data from lmd to ROOT format and its output can be used for a first check of the data. Additionally, the output provides the possibility to plot the pulse shapes for runs in which they were recorded. On the other hand, R3BRoot [r3b18] is used for the advanced analysis and the calibration of the detector as explained in the following section. It was already introduced in Section 5.1 since it is used for the simulations done in this work as well.

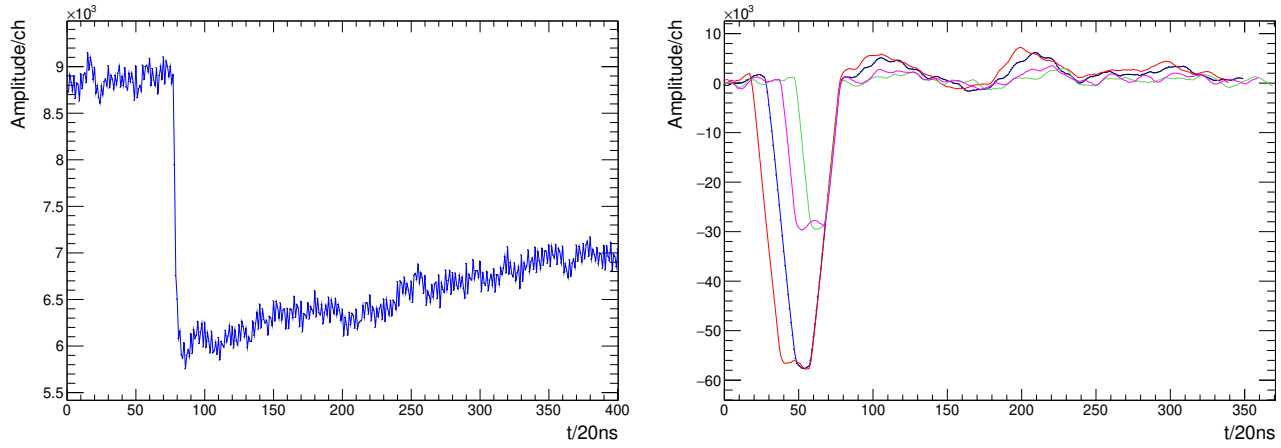

Figure 7.4: Pulse shape after the preamplifier (left) and after the moving-average filter (right). The shape from the filter is depicted for four different filter filter settings: $w=10$ and $g=10$ (green), $w=20$ and $g=10$ (blue), $w=10$ and $g=20$ (pink), and $w=20$ and $g=20$ (red). The gap g defines the width of the flat top of the trapeze, while the decay and rise time of the filter signal corresponds to the integration time w. The noisy signal of the preamplifier leads to a fluctuating baseline of the filter signal. This effect can be reduced with a larger integration time w. Since the filter intervals have to fit in front of the pulse and the pulse starts at ≈ 70, a longer integration time than $w=20$ could not be depicted but can be used during the experiment.

7.3 Calibration

The Micron X5 detectors need to be calibrated before their performance and the influence of the filter settings can be compared. The data are unpacked and analyzed with the R3BRoot framework using *ucesb* for the conversion from lmd to ROOT files. R3BRoot provides several levels similar to the one described in Section 4.1 for *land02*. The Micron X5 detectors and the similar Micron X1 detectors are handled with the same unpacking routines and the same level structure. For the so-called PSPX detectors the following levels are provided.

MAPPED The lowest data level takes the data provided by *ucesb*. The available information is detector number, channel number, and the energy loss measured by the corresponding channel. The energies are given in ADC channels. They can be either positive or negative depending on the polarity of the signal and the side of the detector, respectively. The mapping of the electronic channel number to a meaningful physical channel number is already done by *ucesb*. Error messages from the FEBEX3b ADC are contained in the energy-loss entries.

PRECAL On this level, the channel number is converted to the strip number. Each strip has two energy entries corresponding to its two ends. The energies at both ends are matched the way that the calculated hit position 0 is in the middle of each strip. Additionally, a threshold can be applied to suppress noise if necessary. For the Micron X1 detector with strips on only one side and a cathode for the energy-loss measurement on the back, the back is treated as a strip with only one energy entry.

CAL Within this level the energy calibration is finished. A gain is applied to each strip to match the sum energy of all strips. Energies are now given in keV.

HIT The final detector level provides the hit position in detector specific coordinates uv given in arb.u. and in a general coordinate system xy given in cm. The energy loss of the event is calculated for one-strip or two-strips events and is given in MeV. Additional information, like the quality of the positions and the multiplicity on both sides of the detectors, is given as well.

The calibration consists of three steps and is done with external scripts making use of the ROOT framework. The calibration parameters are then used by R3BRoot to extract the data on the specified levels.

The first step of the calibration, from MAPPED to PRECAL level, is matching the two channels belonging to one strip. Material properties, as well as slightly different gains in the electronic chain, can lead to different amplification of the collected charges at both ends of a strip. If this is the case, the position calculated using Equation 7.2 is not 0 for hits in the middle of the detector. This effect can be compensated with a gain factor applied to the measured energy at one end of the strip. To determine the gain, I make use of so-called interstrip events. An interstrip event is an event in which the ion hits the detector in the area between two strips. The deposited energy is then shared between four anodes instead of two. Since this area is thin, the position of these events is well known in one direction. Therefore, they can be used for the calibration of the perpendicular strips. To select these interstrip events, I gate on events with two neighboring strips hit on one side for which the ion passed through only one strip on the other side. For the determination of the center of the detector, I gate on the interstrip area between strip 16 and 17 on each side. A cut to guarantee that the total energy measured with the strips on the front and the back of the detector is the same cleans the spectrum further. An example of the calculated position can be seen in Figure 7.5. On the left plot, the calculated positions are shown for uncalibrated, i.e., MAPPED level, data. The events corresponding to the interstrip area peak at a position slightly off. This offset is corrected by applying a gain to the measured energy at one end of the strip. The calculated gain parameters are applied to the data using the `R3BPspxMapped2Precal` routine. After this calibration step, the calculated positions for PRECAL data are centered at 0 as can be seen on the right plot.

Additionally, a threshold has to be defined for each channel. Energy entries below this threshold are discarded. These software thresholds are necessary in cases in which the hardware threshold of the FEBEX3b ADC does not prevent the recording of pure noise. During the KVI-CART beam time, this was the case when the drive of the x table was switched on to move the fiber detectors and the proton TOF wall. The drive induced spikes in the signal that triggered the DAQ although the hardware threshold was already set to its maximum. With the software threshold it is possible to remove such events triggered only by noise completely from the data. However, since the energy-loss values change with the choice of the integration time, it is not possible to provide a general threshold for all filter settings. Nevertheless, this is only a problem for the data from the test beam time with varying filter settings but not for an upcoming physics beam time, for which the filter settings will not change during the data taking.

The second step of the calibration takes place between the PRECAL and CAL level. As in the previous step, it matches the gains of the readout channels, but this time the matching is not within a strip but over all strips. For the calibration, events with an ion passing exactly one strip on the front and one on the back are selected. The sum of the energy entries from both anodes

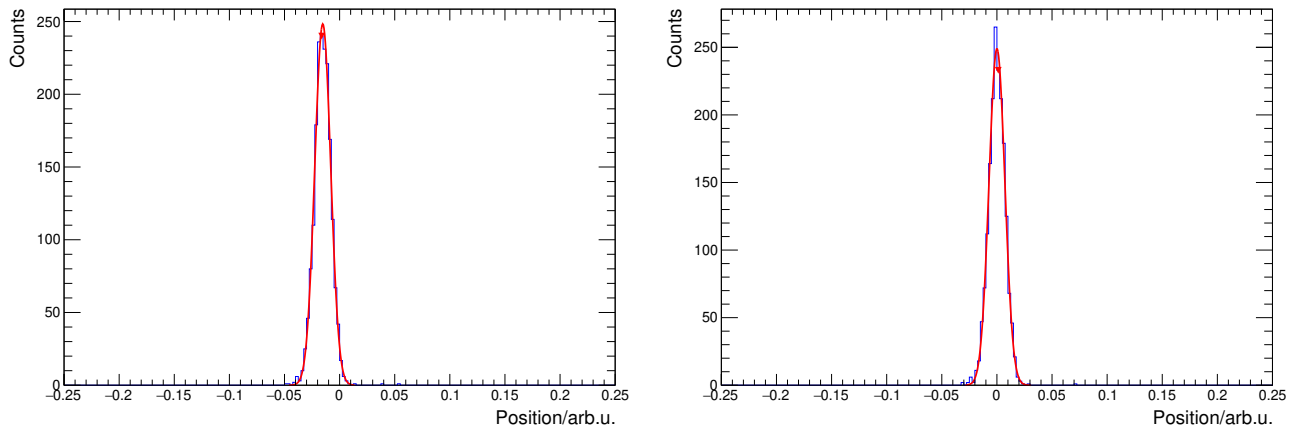

Figure 7.5: First step of the PSPX calibration: Before the calibration, on MAPPED level (left), the interstrip events belonging to the center of the detector have a calculated position different from 0. After the calibration, on PRECAL level (right) the center is shifted to 0 by applying a gain to the energy information of one end of the strip. The plots show the calibration of strip 18 on the front of detector No. 3126-9. It is done with the following filter settings: $w = 10$ and $g = 10$.

of each strip are plotted for the front of detector No. 3126-9 in Figure 7.6. Due to the mismatch of the intrinsic gains, several peaks belonging to different strips are visible in the spectrum on the left. Applying a strip specific gain to all energy entries, the mean value of those peaks is shifted to the same value as can be seen in the right plot. The calculated gain parameters are applied to the data using the `R3BPspxPrecal2Cal` routine. In case that the gain factor is chosen appropriately, this step includes the conversion from ADC channels to keV.

Finally, the last step of the calibration converts the detector intrinsic coordinate u and v into x and y in a general coordinate system. The detector intrinsic coordinates are calculated using

$$u = \frac{Q_2 - Q_1}{Q_1 + Q_2} \tag{7.4}$$

similar to Equation 7.2. They are given in arbitrary units in the range of [-1,1]. However, in reality the position lies in the range $[-L/2, L/2]$ with the length L of the strip. For the conversion from u to x, a strip specific offset and slope is applied

$$x = \text{offset} + \text{slope} \cdot u. \tag{7.5}$$

Again, interstrip events are used to determine these calibration parameters. The calculated positions of multiple interstrip areas are compared to their corresponding positions on the detector. Fitting a straight line to these data points results in the strip specific offset and slope parameters, which are applied to the data using the `R3BPspxCal2Hit` routine. Depending on the radiation damage induced during an experiment, it might be necessary to introduce higher order corrections in the future since small inhomogeneities of the detector material can lead to a non-linear distribution of the positions.

In this work, two detectors, namely Micron X5 detector No. 3126-9 and No. 3126-7, were evaluated. They were calibrated separately using data from the KVI-CART beam time with the ^{12}C beam for which the detectors were operated in vacuum. However, due to the bad

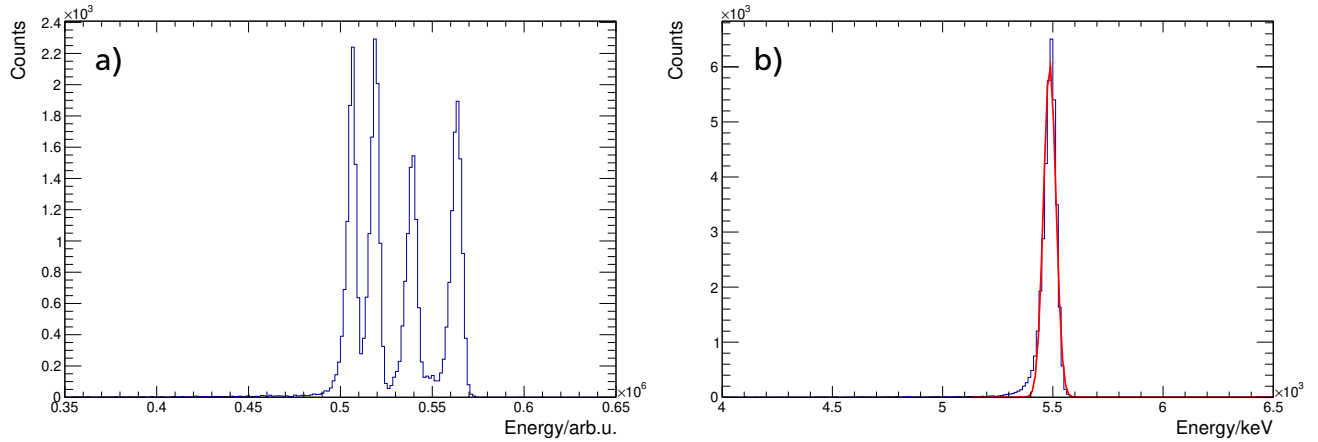

Figure 7.6: Second step of the PSPX calibration: a) Before the calibration, on PRECAL level the sum energy from events with exactly one strip hit shows several peaks corresponding to the different strips. b) After the calibration, on CAL level all peaks are shifted to the same mean value corresponding to the energy of E = 5486 keV deposited by the α particle. The plots are shown for the front of detector No. 3126-9 for the α-source measurement since the effect of this calibration step is more visible with a better energy resolution. The calibration is done with the following filter settings: $w = 200$ and $g = 32$.

energy resolution of the ^{12}C beam, this calibration was not accurate enough for the α-source measurement. Therefore, the second step of the calibration was redone based on the α-source measurement to achieve the best energy resolution. Since during this measurement only a small area of the detector was illuminated, the calibration is only valid for this area and only used for the α-source measurements. Furthermore, the last calibration step was not completed since the beam time at KVI-CART was only used for the characterization of the detectors and no correlations between different detector systems were analyzed. Nevertheless, the calibration scripts and R3BRoot conversion routines for this step are available. They were used in previous analyses and can be used in the upcoming experiments.

7.4 α-source Measurement

A first test of one of the detectors and its performance was conducted at GSI in Cave C with an α source. The detector No. 3126-9 was mounted inside the vacuum chamber and connected to the electronic readout as described in Section 7.2. An ^{241}Am α-source with an activity of ≈ 6 kBq was placed 16 cm away from the detector facing its back. An additional collimator between the detector and the α source reduced the irradiated area to the inner $(1 \times 1)\,\mathrm{cm}^2$.

Due to the low activity of the source and the resulting long measurement time, only a small number of different filter settings were tested. Furthermore, the investigation of the position resolution requires a much higher number of hits than the one of the energy resolution. Therefore, only the energy resolution was measured with the α source, while the investigation of the position resolution is done with the ^{12}C beam at KVI-CART and described in Section 7.5.2.

The energy resolution is determined using only events with multiplicity 2 for both sides of the detector, i.e., exactly one strip on the back and one on the front collects the deposited energy. The

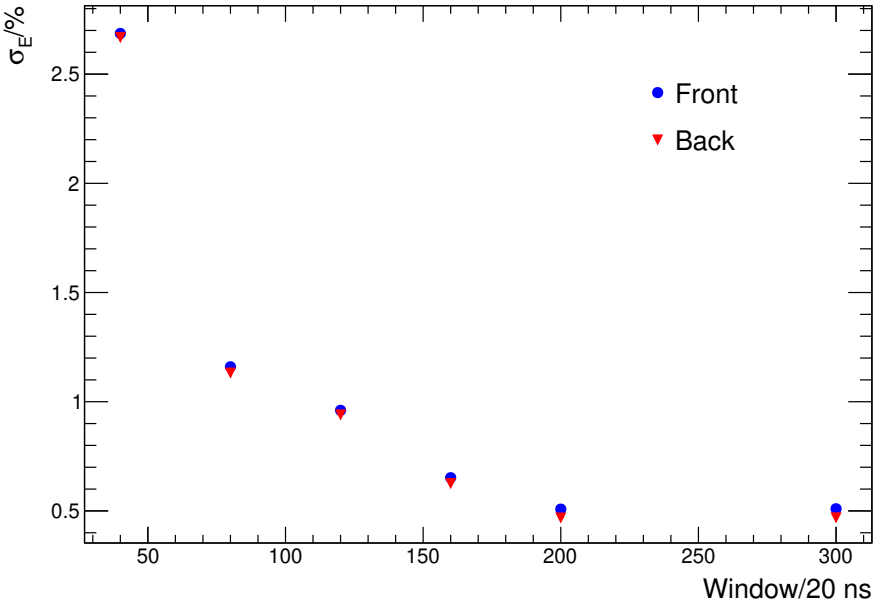

Figure 7.7: Energy resolution of detector No. 3126-9 for an ^{241}Am α-source depending on the filter settings. The window length is varied between w=40 and w=300 for a gap of g=32.

resulting energy spectrum, as shown in Figure 7.6 b), displays one single peak. Its resolution is determined by fitting a normal distribution to the spectrum. The ratio of the standard deviation and the mean of the fit gives the energy resolution in %. The results for different window length w – from 40 to 300 – with a gap g of 32 are shown in Figure 7.7. Later measurements with the ^{12}C beam show that this large gap was not the best choice. Unfortunately, a second measurement with an optimized gap was not yet possible. Nevertheless, the measurements show that the design goal of $\sigma_E/E < 1\,\%$ is achievable for a window length larger than 120 corresponding to 2.4 μs.

7.5 ^{12}C Measurement at KVI-CART

The main test of the two Micron X5 detectors was conducted at KVI-CART using the setup introduced in Section 7.2. The ^{12}C beam at KVI-CART had a relatively small beam energy of 90 AMeV with a large energy resolution of 0.4 %. Therefore, the energy resolution is limited by the beam parameters. Aleksandra Kelic-Heil [KH17] used a MOCADI [Wei18b] simulation to calculate the expected energy loss in the various detectors for a setup very close to the real one. For the Micron X5 detector an energy loss of $E_{X5} = (11.63 \pm 0.399)$ MeV was expected, which corresponds to an energy resolution of 3.43 %.

During the beam time, the filter settings were varied. For each combination of window length w and gap g, a similar amount of events were recorded. A first analysis during the beam time showed the most promising candidates for the optimal energy and position resolution. Those settings were then chosen for additional measurements with increased statistics. The additional runs were needed, on one hand, for the first calibration step (`R3BPspxMapped2Precal`) and, on the other hand, for the comparison of the performance of the two detectors. However, since the first analysis was done with uncalibrated data, the chosen settings are not the ones with the

Table 7.1: Energy and position resolution of detector No. 3126-9 and No. 3126-7 for ^{12}C with E=90 AMeV in air and vacuum. The energy resolution was achieved with w=250 and g=10 (air, vacuum for detector No. 3126-7) or g=12 (vacuum for detector No. 3126-9). Only events with exactly one strip hit on the according side are taken into account. The position resolution was achieved using interstrip events with w=10 and g=10, taking into account the four strips with the most statistics (strip 15-18 for the front, strip 16-19 for the back).

detector	3126-9		3126-7
	vacuum	air	vacuum
E, front	3.700(1) %	3.753(1) %	3.739(1) %
E, back	3.792(1) %	3.823(1) %	3.849(1) %
y, front	(330-405) μm	(365-425) μm	(365-415) μm
x, back	(335-410) μm	(340-415) μm	(360-435) μm

best energy and position resolution. Nevertheless, the achieved performance is comparable to the one of the best settings. Therefore, they are used for the comparison of the two detectors in Table 7.1.

Although both detectors show only a moderate performance, the following conclusions are valuable. First of all, the difference between the detector No. 3126-9 operated in air or in vacuum is similar to the difference between the two detectors. Therefore, whether to place the detector in a light-tight chamber or a vacuum chamber can be decided depending on the availability of an adequate chamber, the placement within the setup, and the surrounding detector systems. An operation in air simplifies the exchange of the detector after radiation damage, while the placement inside a combination of vacuum chambers avoids light-tight entrance and exit windows. In both cases, the energy and position resolution is comparable.

The two detectors, which are both p-type detectors with the same thickness, show a similar performance. Both the energy and the position resolution of detector No. 3126-9 are slightly better than those for detector No. 3126-7, but the improvement is only $\approx 0.06\,\%$ for the energy and 35 μm for the position resolution. One reason for the worse performance might be that the bonding of four anodes of detector No. 3126-7 were broken. Therefore, the voltage was not applied homogeneously to the detector and small distortions of the electric field could occur.

7.5.1 Energy Resolution

The energy resolution is calculated for the detector No. 3126-9 for different combinations of window length w and gap g for the moving-average filter. Again, only events with multiplicity 2 on both sides are used for the analysis. As done before for the α-source measurement, a normal distribution is fitted to the energy spectrum. The ratio of the standard deviation and the mean of the fit defines the resolution. The results can be seen in Figure 7.8. At first, the integration time w is increased from 10 up to 250 with a constant gap g of 12. As one can see with increasing window length the energy resolution improves up to its optimum at $w = 200$. The general trend of a better resolution for larger integration times is only broken by the data point for $w = 175$ for which the resolution is slightly worse than for the two neighboring points. However, during

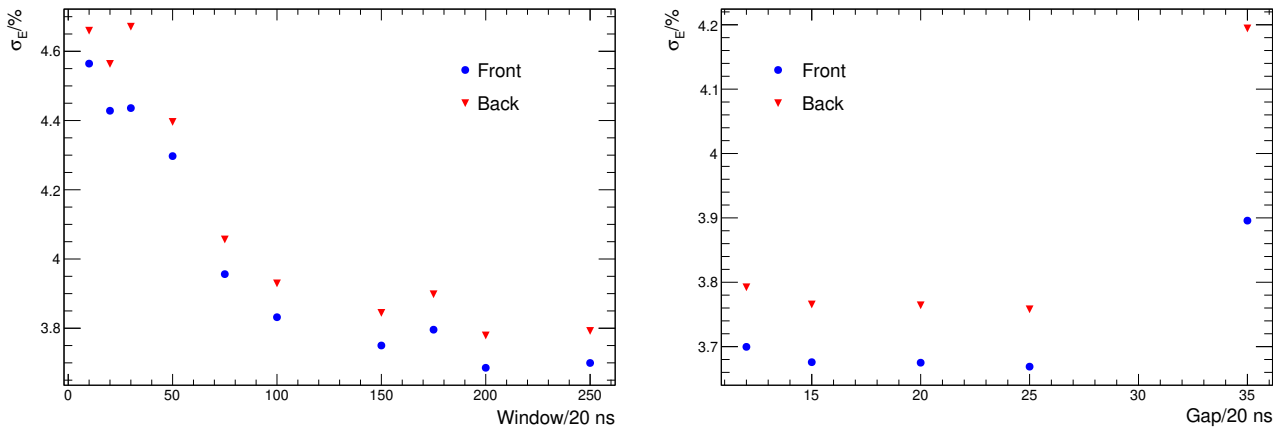

Figure 7.8: Energy resolution of detector No. 3126-9 for ^{12}C with E=90 AMeV depending on the filter settings. On the left, the window length is varied between w=10 and w=250 for a gap of g=12, while on the right the gap is varied between g=12 and g=35 for a window of w=250. The data points at w=175 (left figure) were taken with the drive of the x table switched on. The data points for g=35 (right picture) were taken with the drive of the x table switched on as well and with a higher rate than all other data points. In both cases the introduced noise worsens the energy resolution.

this run the drive to move the fiber detectors Fiber4 - Fiber6 and the proton TOF was switched on. As mentioned before, the control of the drive induces large spikes in the Micron X5 detector signals. This does not only influence the ability to trigger but also worsens the resolution. To be able to estimate the effect of such a source of noise, the run was analyzed and the data are presented in this thesis. Additionally, during the beam time, a first analysis of the uncalibrated data showed the best energy resolution for $w = 250$. Therefore, the resolution depending on the gap is studied using $w = 250$ instead of $w = 200$.

The energy resolution is almost the same for all tested values of the gap g from 12 up to 25. Only for $g = 35$, it is (5 – 10) % higher, but for this run again the drive was active and, additionally, the rate of the impinging ions was around a factor of 5 higher than for all other runs analyzed. The noise and the overlapping pulse shapes lead to a worse energy resolution. Nevertheless, since the measurement with the α source is done with a gap of 32, this value can – with limitations – be used for comparison. Anyhow, choosing the right value for the gap has a much smaller influence on the energy resolution than the window length. Finally, for the comparison of the two different detectors and the influence of air around the detector, a value of 12 was chosen since this value showed the best resolution during the analysis at KVI-CART.

An additional effect that usually influences the energy resolution is the ballistic deficit. Due to the dependency of the rise time on the position of the hit, only a certain amount of the collected charge can be measured depending on the integration time. As a result, the measured energy depends on the position. However, when plotting the total deposited energy of a hit over its position for each strip separately, no dependency could be found independent of the integration time of the moving-average filter. The reason for this effect and why it does not play a role in my data is explained in Section 7.6.

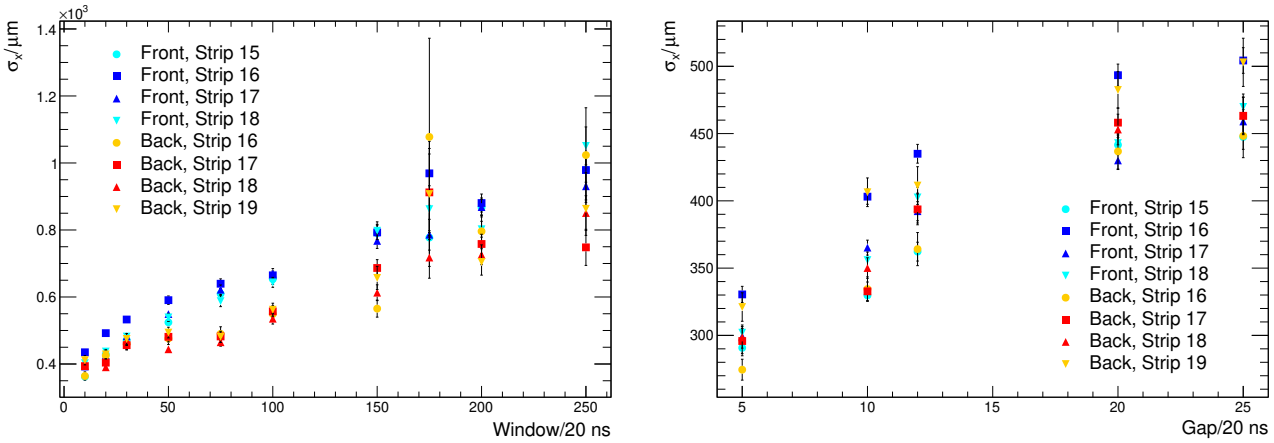

Figure 7.9: Position resolution of detector No. 3126-9 for ^{12}C with E=90 AMeV depending on the filter settings for the four most radiated strips of each side. On the left, the window length is varied between w=10 and w=250 for a gap of g=12, while on the right the gap is varied between g=5 and g=25 for a window of w=10. The data points at w=175 (left figure) were taken with the drive of the x table switched on. The introduced noise worsens the position resolution.

7.5.2 Position Resolution

To be able to benchmark new detectors and to monitor the position resolution during the experiment without placing additional detectors in the beam, so-called interstrip events are used. Their definition, as well as their use for calibration, are already explained in Section 7.3. Since an interstrip area is – by design – very thin, the position of the particle in the corresponding direction is well known, which in the following is used to check the position resolution of the detector No. 3126-9 as a function of the window length and the gap of the moving-average filter.

The position resolution can vary between different strips of one detector. Hence, it is calculated for the four most radiated strips on both sides of the detector. For the front these are the four innermost strips, while for the back the beam spot was slightly shifted and therefore strip 16 - 19 are analyzed. For all eight strips a gate on the center interstrip area, as well as a neighboring interstrip area, are applied. A normal distribution is fit to the interstrip events – comparable to the one in Figure 7.5 – and its standard deviation is used as a measure for the resolution. Additionally, the distance between the two interstrip areas, which is a multiple of the strip thickness, is used to translate the resolution from arb.u. into μm. In Figure 7.9 one can see the results for different filter settings.

In general, the different strips show a wide spread in position resolution. Nevertheless, the position resolution decreases with a smaller window length for all strips. The best resolution is achieved with an integration time of $w = 10$, albeit no data were taken for even smaller window lengths. Again, the data for 175 were taken during a run in which the drive for the fiber detectors was switched on and induced spikes in the signals of the Micron X5 detector.

A similar behavior could be observed for the gap. The smaller the gap between the two windows, the better the position resolution. However, the effect of the gap is not as significant as the one of the window length. A large gap of 25 worsens the position resolution to $\approx 470\,\mu$m, which is less than a factor of 2 more than the best resolution of $\approx 310\,\mu$m for a gap of 5.

In all cases, the measurement suffers from the limited number of events within the multiplicity cuts. Since runs for two detectors and a wide range of filter setting were needed, it was only possible to record short runs for each settings. This does not pose a problem for the energy resolution, for which almost all events can be used but is a problem for the determination of the position resolution, for which a gate on interstrip events is necessary. The large uncertainty of the position resolution in comparison to the negligible one for the energy resolution illustrates this problem.

7.6 Discussion

One factor that restricts the choice of the integration time is the ballistic deficit. The resistive surface R_D of the strip together with the capacitance C_D of the depletion zone introduces an additional time constant τ_D. Since the active resistance depends on the position of the hit, the rise time of the signal is position dependent as well. Erik Lægsgaard [Læg79] describes the signal shape without any influence of the preamplifier as follows. The collected charge at one end of the strip in Figure 7.1 with a particle depositing energy at position x is

$$Q_1(t,x) = Q_0\left[\frac{x}{L} - \frac{2}{\pi}\sum_{n=1}^{\infty}\frac{\sin n\pi(1-\frac{x}{L})}{n}\cdot\exp\left(-n^2\pi^2\frac{t}{t_D}\right)\right]. \tag{7.6}$$

To determine the energy loss, the collected charge at both ends of the strip is summed up. As a consequence, it can be described as

$$Q_E(t) = Q_1(t,x) + Q_2(t,L-x) \tag{7.7}$$

$$= Q_0\left[1 - \frac{2}{\pi}\sum_{n=1}^{\infty}\frac{\left(\sin n\pi(1-\frac{x}{L}) + \sin n\pi\frac{x}{L}\right)}{n}\cdot\exp\left(-n^2\pi^2\frac{t}{t_D}\right)\right]. \tag{7.8}$$

In both cases, the time constant is given by $\tau_D = R_D \cdot C_D$ with $C_D = \epsilon_0\epsilon_{Si}\cdot A/d$. In Figure 7.10 one can see the dependency of the signal rise time on the position. For hits directly next to the anode, the signal is a step function, while for hits further away from the anode, the rise time of the signal becomes larger. The energy signal shows the same behavior as the signal of a single anode, but the pulse shapes are symmetric around the middle of the detector $x = L/2$. To reconstruct the position without any influence of the position specific rise time, an integration time of at least $t > 0.35\tau_D$ is necessary. For the energy-loss reconstruction an integration time of $t > 0.45\tau_D$ is needed to get rid of the ballistic deficit. The surface resistance of the Micron X5 detector is $R_D \approx 1\,\mathrm{k\Omega}$. Together with the thickness of $d = 210\,\mu\mathrm{m}$, the permittivity for Si $\epsilon_{Si} = 11.7$, the vacuum permittivity $\epsilon_0 = 8.854\,187\,8 \times 10^{-12}\,\mathrm{F/m}$, and an active area of $(9.57 \times 9.57)\,\mathrm{cm}^2$, the capacitance of a single strip is $C_{D,Strip} \approx 150\,\mathrm{pF}$ and, therefore, the time constant is $\tau_D \approx 150\,\mathrm{ns}$. Thus, a window length of $w > 4$ – corresponding to an integration time of 80 ns – is needed to avoid the ballistic deficit introduced by the resistive surface of the detector.

Additional position dependent time constants introduced by the AC coupling of the charge sensitive preamplifier are reduced by choosing a large coupling capacitor of $C_C = 94\,\mathrm{nF}$. with a Micron X1 detector – a detector similar to the Micron X5 detector but with only strips on one side and in one direction – I investigated the effect of this rise time on the pulse shape and the position determination. The results are presented in [Syn14].

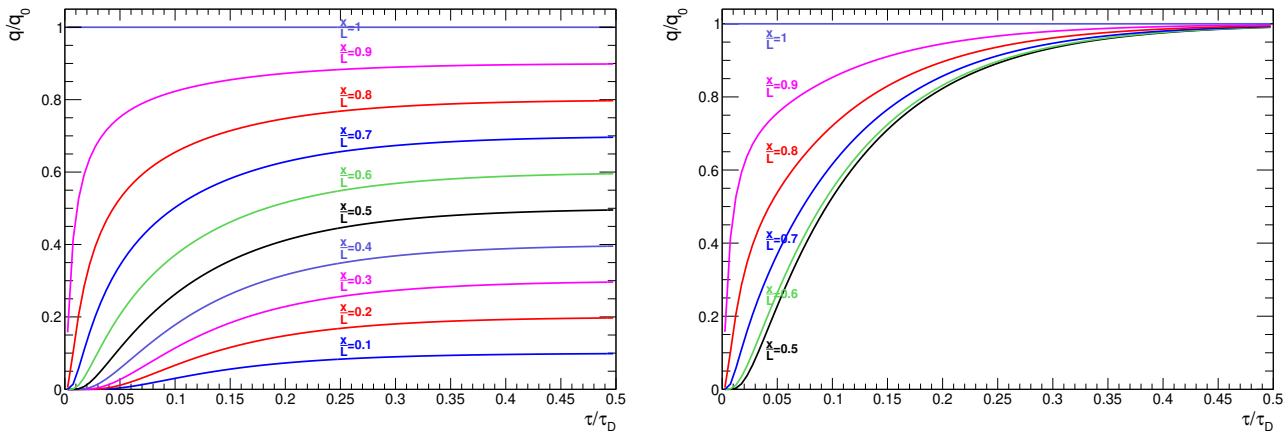

Figure 7.10: Behavior of the charge collection process for the position (left) and energy (right) determination. Depending on the position x of the hit an integration time of up to $t > 0.45\ \tau_D$ is needed to reconstruct the position and the energy loss.

However, the main reason why different filter settings are necessary to achieve the best energy and position resolution lies in the decay characteristic of the pulse shape. To examine this behavior, average pulses are built from hits close to each other. As an example, the pulse shapes of a single strip are analyzed. They are grouped depending on which perpendicular strip on the other side of the detector was hit at the same time. Therefore, the hits in one group belong to similar positions. The pulse shapes of the hits in each group are then averaged and Equation 7.2 and 7.3 are applied to these average pulses. The results are depicted in Figure 7.11.

The pulse shapes for the energy determination show no dependency on the position of the hit. Hence, a large integration time which helps to average out noise contributions is favorable. Especially the pulse shapes for the energy determination display systematic variations of the peak height. Since the pulse shapes are already averages of a large number of single pulses, this variation stems not from random noise but is a contribution probably from the preamplifier. For the pulse shapes for the position determination, this effect is visible as well but much smaller. Furthermore, these pulse shapes have significantly different decay times depending on their position on the strip. Since for a long integration time the decay time influences the result significantly, only short integration times can be used for a precise position determination. However, the integration time needs to be large enough to avoid the ballistic deficit mentioned before and to average the noise of the pulse shape visible in Figure 7.4.

As a conclusion, long integration times are favorable to improve the energy resolution, while short integration times are necessary to achieve a reasonable position resolution. Therefore, the use of two different filter settings at the same time is needed for these detectors in future experiments.

7.7 Comparison with Previous Measurements

One Micron X5 prototype detector was already tested during a beam time dedicated to the test of the active target and various other detector systems at GSI in June 2016. The detector was irradiated with a ^{124}Xe beam with a nominal energy of $E = 600\,\text{AMeV}$. Some of the other detectors tested at the same time were placed in front of the Micron X5 detector. They introduced position and energy straggling and caused a slightly smaller beam energy. Since – in addition to

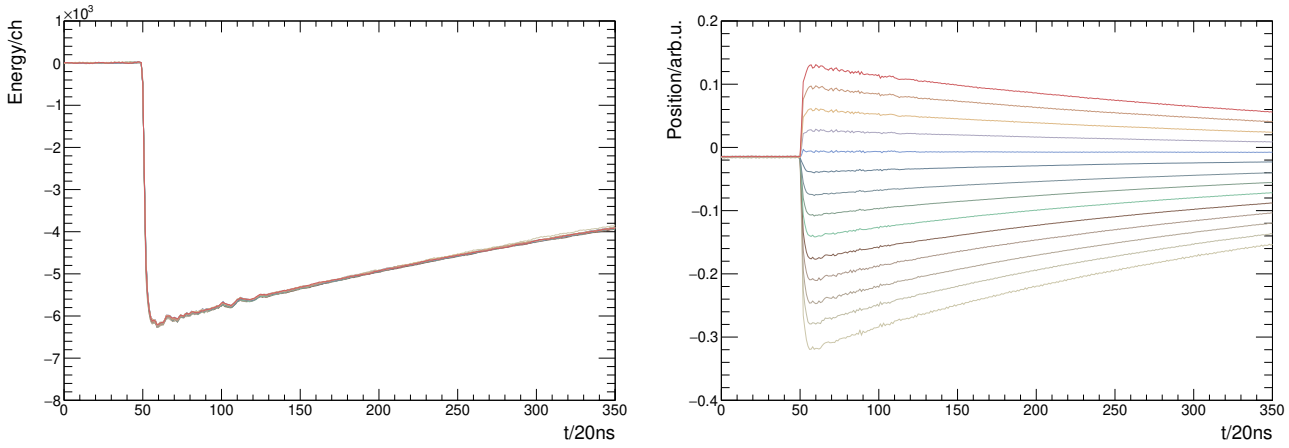

Figure 7.11: Averaged pulse shapes for energy (left) and position (right) determination. Pulse shapes for different positions *x* within a strip are shown in different colors. The pulse shapes for the energy determination are the same for all positions, while the decay time of the pulse shapes for the position determination depends on the position of the hit.

a prototype LOS detector and four Micron X1 detectors – varying detector systems were placed in the beam line, the expected energy deposition and energy resolution are unknown.

The tested detector No. 3126-10 is a p-type detector with a thickness of 209 μm. It is identical to the detectors used at KVI-CART. It was placed inside a light-tight chamber. To avoid additional straggling from the vacuum windows, the entrance and exit windows were sealed with a thin, black foil. Hence, the chamber could not be evacuated and the detector was operated in air. However, as one can see from the results from the KVI-CART beam time in Table 7.1, whether the detector is operated in air or in vacuum makes almost no difference. The setup looked very similar to the one at KVI-CART depicted in Figure 7.3. The detector signals were led through a feed-through to mesytec MPR-32 preamplifiers with an energy range of 3 GeV. The amplified signals were then guided to the FEBEX3b ADC, where the signals were digitized and recorded. The detector was reverse biased via the preamplifiers using the mesytec MHV-4 HV. In contrast to the setup explained above, the trigger was provided from the Main DAQ, i.e., the LOS trigger was used. In this case, the internal trigger – with $w = 8$ and $g = 4$ as settings for the trigger filter – was only used to select the channels for which the deposited energy was recorded but not to start the data taking.

The analysis of the data was performed by Sonja Storck [Sto17]. Her results are summarized in Table 7.2 to be able to compare them with the results obtained for the ^{12}C isotopes and the α-source measurements. In addition to the resolution, the efficiency with which the energy and the position can be reconstructed was determined to be 82.8 % and 73.0 %, respectively. For this, the number of events with a valid energy and position on HIT level were compared with the total number of events recorded. Since the start detector LOS, which was used to trigger the DAQ, is expected to have an efficiency of 100 %, the number of recorded events is the same as the number of passing particles. Due to cuts applied during unpacking from CAL to HIT level, only events with multiplicity 2 or 4 on at least one side of the detector were taken into account. However, no additional checks – like, e.g., that the energies measured with the front and the back of the detector are the same within their uncertainties – were performed to guarantee the validity of the events. One one hand, more stringent conditions might decrease

Table 7.2: Energy and position resolution of detector No. 3126-10 for ^{124}Xe with E=600 AMeV in air. The resolution was achieved with $w=12$ and $g=12$.

detector	3126-10
	air
E	1.3 %
y, front	(335-765) μm
x, back	(125-165) μm

the efficiency even further but, on the other hand, one might be able to reconstruct more events with more sophisticated algorithms. The efficiency cannot be given for the ^{12}C beam at KVI-CART or the α-source measurement since the data were taken in standalone mode and, therefore, no comparison to the total amount of passing particles can be made.

The results for the ^{124}Xe beam in Table 7.2 show a significant difference between the front and the back of the detector. The front displays a worse position resolution than the back. In addition, a double peak structure is visible when a gate on the interstrip events is applied. One problem that explains this was identified during the beam time but could not be solved immediately. When biasing the detector with the depletion voltage, the leakage current increased slowly up to 20 μA. At this point, the current limit of the HV module stepped in and the voltage dropped, while the leakage current stayed at 20 μA. The reason for this was a shortcut in the feed-through. As a consequence, the voltage applied to the detector was only a fraction of the depletion voltage and the detector, therefore, not completely depleted. Since in this case only a part of the detectors is an active volume and the electric field between the strips is distorted, the charge collection is disturbed. This explains the bad position resolution of one side and the low efficiency of the detector. With new feed-throughs, no problem with the leakage current and the applied voltage has been observed during the KVI-CART beam time.

Finally, the data were taken with $w = 12$ and $g = 12$ as settings for the moving-average filter. Due to the problem with the leakage current, the overall measurement time was only a few hours. Therefore, no study of the dependency on the filter settings was made. In the meantime we know that the window length and gap is a good choice for the position but not for the energy determination. With optimized filter setting a much better energy resolution should be achievable, with the result that even isotopes in the region of tin can be separated without any problem.

8 Conclusion and Outlook

In this thesis, I presented the analysis of proton knockout reactions on the neutron-rich nitrogen isotopes ^{17}N, ^{19}N, and ^{21}N. These reactions populate the neutron-rich, even-even carbon isotopes ^{16}C, ^{18}C, and ^{20}C.

I employed the model of two-state mixing to describe the first excited 2^+_1 state of the carbon isotopes. In this picture, two states describing a pure proton and a pure neutron excitation mix. From the QFS reaction data I could extract the proton amplitude by comparing the number of events corresponding to the first excited 2^+_1 state and the 0^+ ground state on the reconstructed H target. The behavior of the proton amplitude for more neutron-rich nuclei matches the expectation [MPF$^+$14]. With an increasing number of neutrons, the proton amplitude increases from $\beta(^{16}\text{C}) = 9.6(16)\,\%$ to $\beta(^{20}\text{C}) = 16.8(61)\,\%$. The increase in proton excitation can be explained by a reduced gap between the $1p_{3/2}$ and the $1p_{1/2}$ orbit due to the tensor force. The increasing number of neutrons in the $1d_{5/2}$ orbit has a repulsive effect on the $1p_{3/2}$ proton orbit and an attractive effect on the $1p_{1/2}$ proton orbit. It is one example of the effect that the tensor force has on the evolution of the single particle energies in neutron-rich nuclei.

However, the results exhibit large uncertainties. Especially in the case of ^{20}C, the lack of statistics is the main drawback. Even though the 2^+_1 state is the only bound excited state of this isotope and the γ-ray spectra and the fit are very clean, the small number of recorded events does not allow for more precise results. One possibility to collect a larger amount of events on a similar time scale than for the experimental campaign S393 is the increase of the beam intensity. This will be the case in the new R^{3}B setup, for which new tracking detectors and a new DAQ make a higher beam rate accessible. Another problem was that the bad energy resolution of the γ-ray detector XB made it hard to distinguish states with similar energies. This was especially the case for ^{16}C, for which the 2^+_2, 3^+, and 4^+ states are separated by 100 keV (2^+_2 and 3^+) and 57 keV (3^+ and 4^+), respectively. With XB having an energy resolution of $\sigma_E \approx 55$ keV for a γ-ray energy of 2 MeV in the lab system and the additional resolution introduced by the Doppler broadening due to the large opening angle of 14° of the single crystals, it was not possible to measure the branching ratio and the relative population for these states. Thus, their values were taken from the literature [PPC$^+$12]. In conclusion, an experiment with the updated R^{3}B setup explicitly dedicated to these isotopes could mitigate these issues.

Next, I reported on the inclusive and exclusive cross sections of the analyzed reactions. This included QFS reactions on the reconstructed H target and knockout reactions on the C target. I compared the exclusive cross sections with theoretical calculations in the Glauber framework done by Carlos Bertulani [Ber17]. The comparison of the experimental spectroscopic factors and the expectation from the two-state mixing model showed that this model is missing the description of short- and long-range correlations.

The analysis of the knockout data exhibited several problems. The first one was the lack in statistics, especially for the reactions of ^{21}N. The small number of events led to large uncertainties for the QFS case, while for the knockout reaction the number of fragments was too small to calculate the inclusive cross section, let alone determine those of the excited states. The second issue contributing to the large uncertainties was the missing reaction trigger for knockout

reactions. Since a reaction trigger for these events is not possible, two changes can improve the uncertainties. In case that the new DAQ can handle the increasing amount of data, a reduction of the downscaling factor for the *Fragment* trigger would improve the precision of the inclusive cross sections. Furthermore, if no trigger efficiency is lost due to the walk effect in XB, the relative downscaling factor between the *XB Sum* and *Fragment* trigger is known precisely. As a consequence, the measurements of the exclusive cross sections of the excited states are more accurate. Finally, one might want to test whether a shielding around the target area reduces the background in the γ-ray spectra.

In addition, I reported on the performance of two PSP prototype detectors for the new R^3B setup. The detectors were tested in a dedicated beam time at KVI-CART. In general, the two Micron X5 detectors worked well. An α-source measurement confirmed that the detectors are able to reach their specified energy resolution. However, the test showed that two different filter settings are essential for optimal performance. While the position resolution is best for short integration times, the energy resolution improves with higher integration times.

Nevertheless, additional tests are needed. First of all, the efficiency of the detectors has to be determined. Since the detectors are used for the identification of the incoming and outgoing particles, an efficiency of almost 100 % is required. Unfortunately, it was not possible to determine the efficiency during the test beam time. Since no data were taken with the Micron X5 detector in coincidence with any other detector, no correlations could be analyzed. Furthermore, the influence of the beam rate on the efficiency and the energy and position measurement needs to be examined. The beam rate has to be limited such that the performance of the detectors is not affected. Therefore, the in-beam tracking detectors can be a bottle neck at high intensities. Moreover, the effect of radiation damage on the detector performance has to be investigated. Although, one expects a worsening of the energy and position resolution, the magnitude of this effect is unknown. Its dependency on the rate of the incoming beam and the overall dose needs to be investigated as well as a possible deterioration of the linearity of the position measurement. In this case, the R3BRoot conversion routine from CAL to HIT level has to be adjusted to correct for such effects. The upcoming beam time S444 at GSI dedicated to the commissioning of the tracking detectors, the calorimeter CALIFA, the superconducting magnet GLAD, and the new neutron detector NeuLAND will give an opportunity to test the mentioned parameters.

A Appendix

A.1 Overview Runs

Table A.1: Overview over runs used in the analysis

	Target	Runs			
Setting 3: $^{17}\mathrm{N} \rightarrow {}^{16}\mathrm{C}$	CH_2	453	455		
	C	452			
	MT	454			
Setting 4: $^{19}\mathrm{N} \rightarrow {}^{18}\mathrm{C}$	CH_2	413	414	418	427
	C	426			
Setting 6: $^{21}\mathrm{N} \rightarrow {}^{20}\mathrm{C}$	CH_2	473	480	515	517
	C	476	514		
^{60}Co Source	-	644			
Cosmic Background	-	496			

A.2 Target Properties

Table A.2: Properties of targets used in the analysis

	Target	thickness d/mm	density ρ/g/cm^3	area density τ/1/cm^2
Setting 3: $^{17}\mathrm{N} \rightarrow {}^{16}\mathrm{C}$	CH_2	4.98	0.92	$1.97(4) \times 10^{22}$
	C	3.03	1.84	$2.80(6) \times 10^{22}$
Setting 4: $^{19}\mathrm{N} \rightarrow {}^{18}\mathrm{C}$	CH_2	9.81	0.94	$3.97(8) \times 10^{22}$
	C	5.08	1.84	$4.69(9) \times 10^{22}$
Setting 6: $^{21}\mathrm{N} \rightarrow {}^{20}\mathrm{C}$	CH_2	9.81	0.94	$3.97(8) \times 10^{22}$
	C	5.08	1.84	$4.69(9) \times 10^{22}$

A.3 Spectra for Setting 3: $^{17}N \rightarrow {}^{16}C$

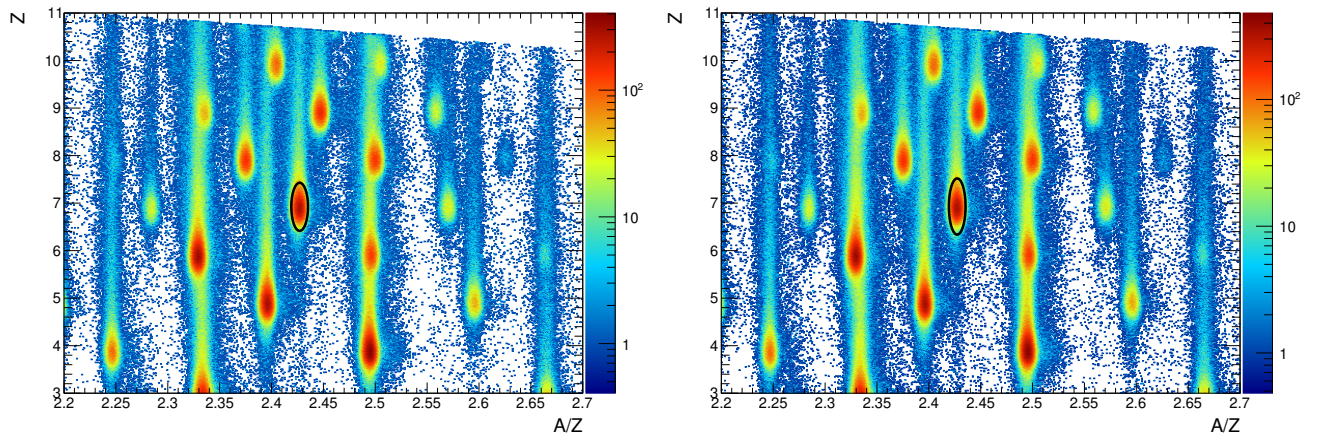

Figure A.1: Incoming ID for setting 3 and the C (left) and the empty (right) target. The applied cut on incoming ^{19}N is shown in black. This plot is drawn for the *Min Bias* Tbit.

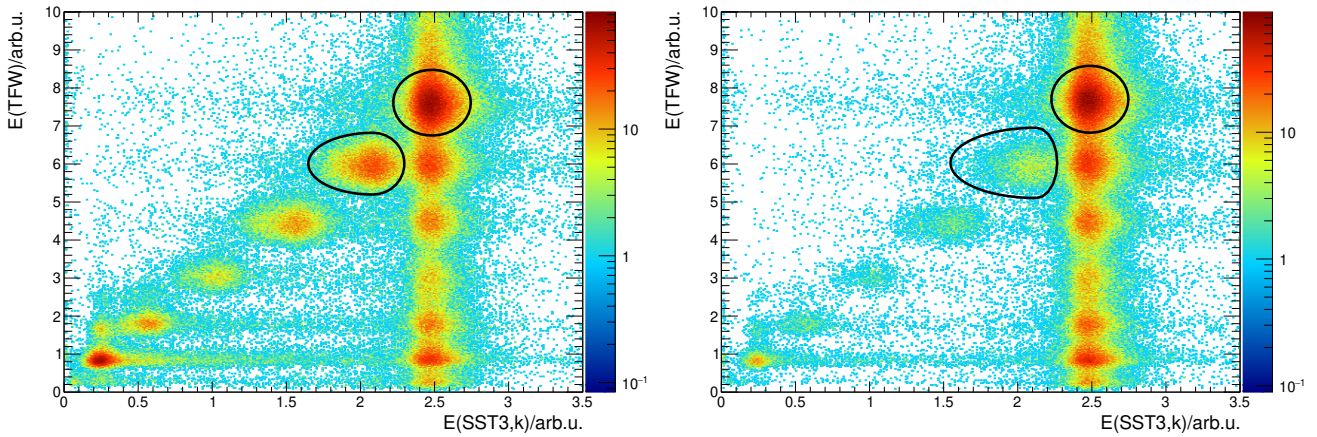

Figure A.2: Outgoing charge for setting 3 and the C (left) and the empty (right) target. The applied cuts on outgoing $Z=6$ and $Z=7$ are shown in black. This plot is drawn for the *LAND* Tbit.

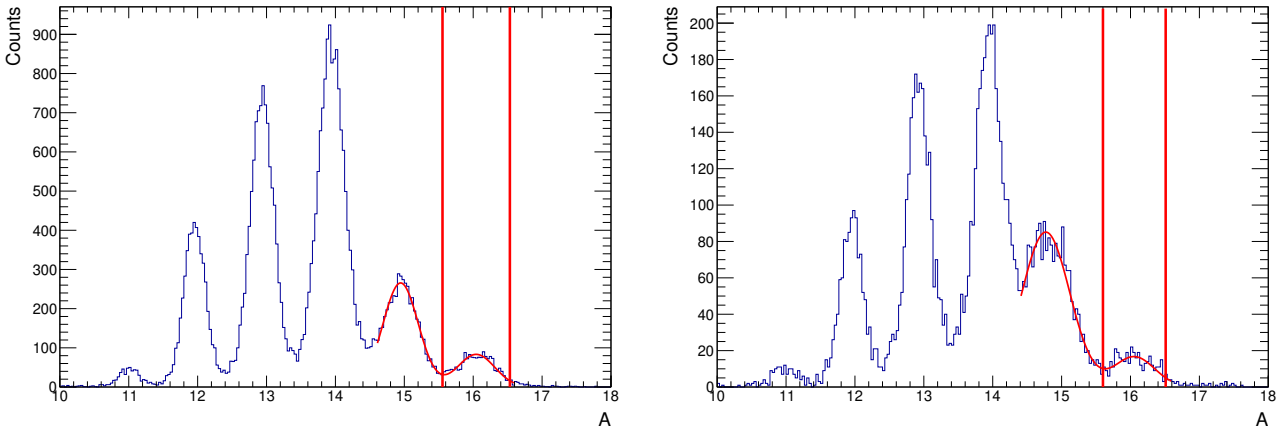

Figure A.3: Outgoing mass for setting 3 with a cut on $Z=6$ for the C (left) and the empty (right) target. The applied cut on outgoing $A=16$ is shown in red. The plot is drawn without a trigger condition.

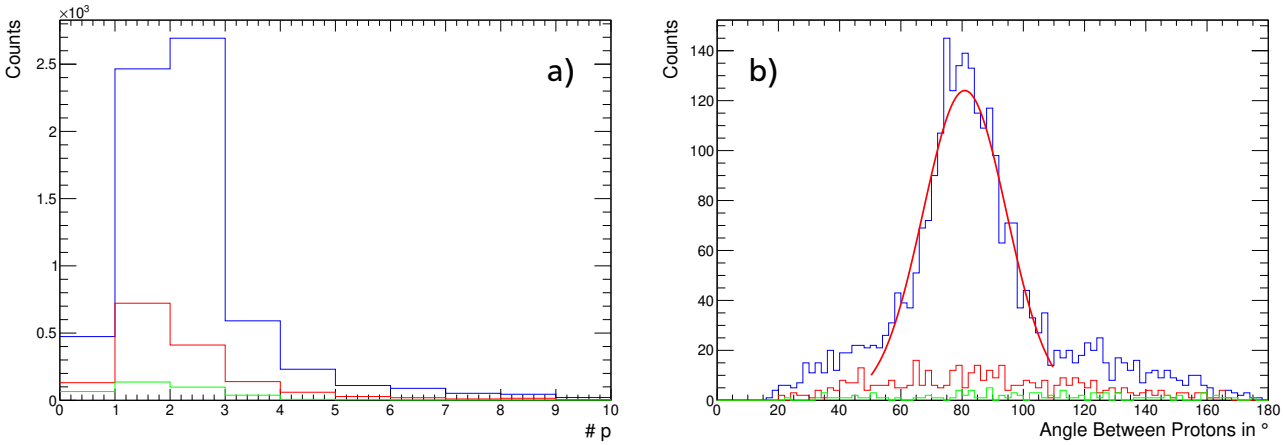

Figure A.4: a) Proton multiplicity and b) angle between two protons for the CH_2 (blue), C (red), and empty target (green). The plots are shown for setting 3 for the *XB Sum* Tbit and in case of the angle in b) with a cut on events with exactly two protons. The angles of the protons are randomized over the whole area of the corresponding crystal. The angle between the two protons for the CH_2 target (blue) shows a peak at 80.9°.

A.4 Spectra for Setting 4: $^{19}N \rightarrow {}^{18}C$

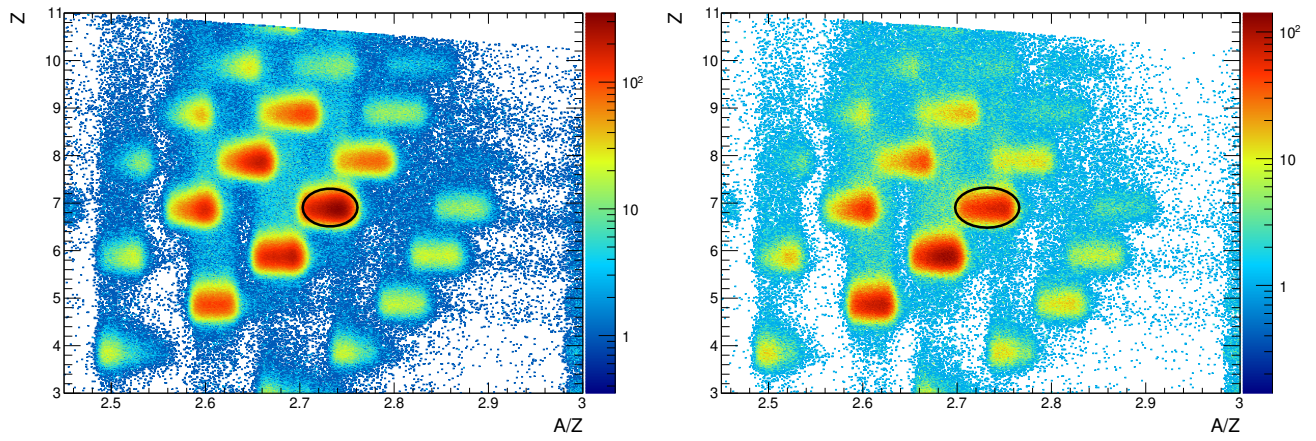

Figure A.5: Incoming ID for setting 4 and the CH_2 (left) and the C (right) target. The applied cut on incoming ^{19}N is shown in black. This plot is drawn for the *Min Bias* Tbit.

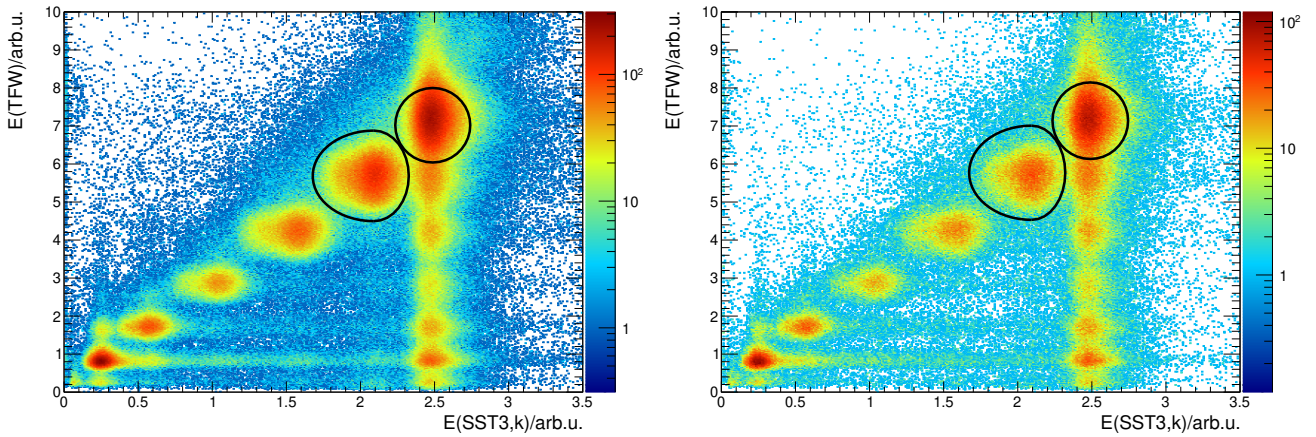

Figure A.6: Outgoing charge for setting 4 and the CH_2 (left) and the C (right) target. The applied cuts on outgoing $Z=6$ and $Z=7$ are shown in black. This plot is drawn for the *LAND* Tbit.

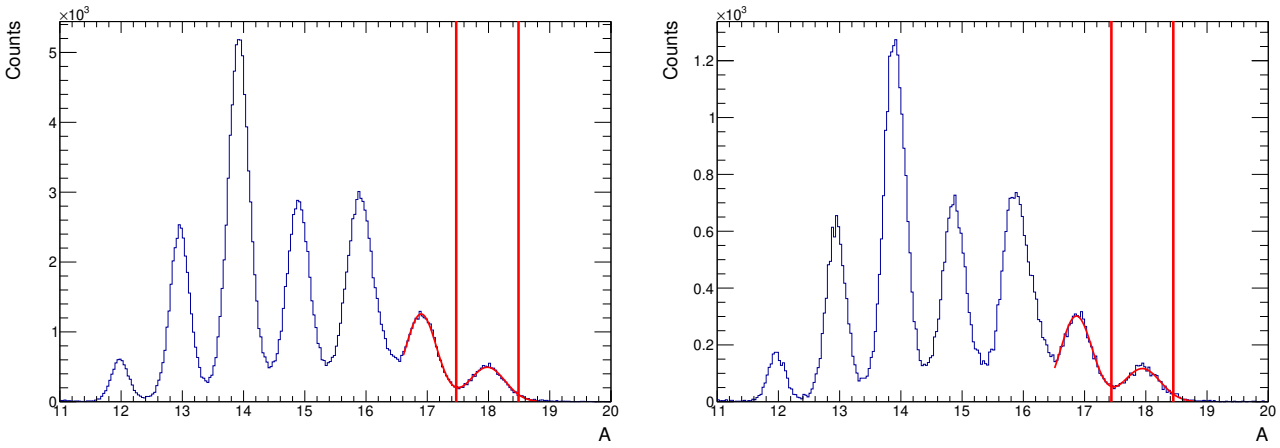

Figure A.7: Outgoing mass for setting 4 with a cut on $Z=6$ for the CH_2 (left) and the C (right) target. The applied cut on outgoing $A=18$ is shown in red. The plot is drawn without a trigger condition.

A.5 Spectra for Setting 6: $^{21}N \rightarrow {}^{20}C$

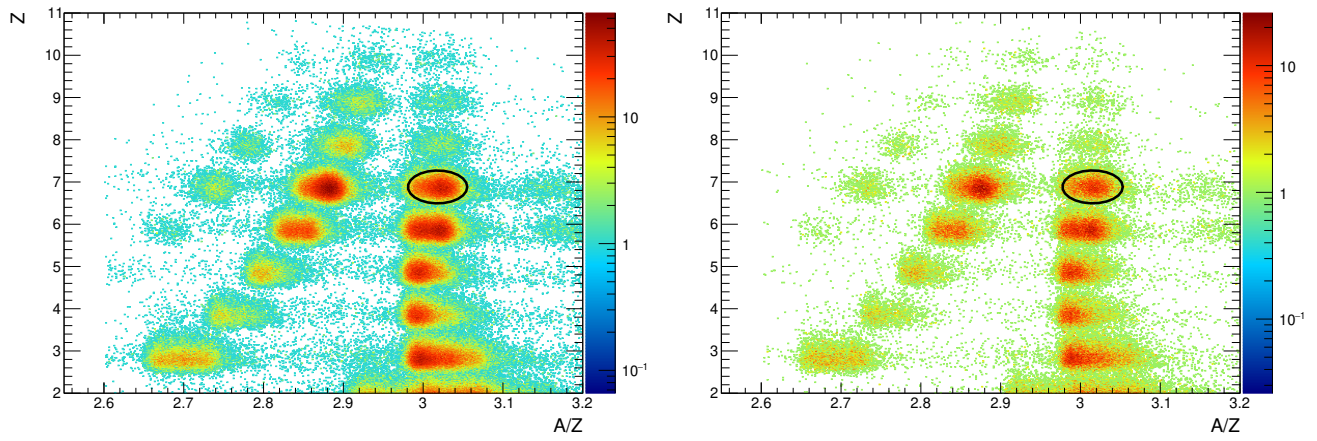

Figure A.8: Incoming ID for setting 6 and the CH_2 (left) and the C (right) target. The applied cut on incoming ^{21}N is shown in black. This plot is drawn for the *Min Bias* Tbit.

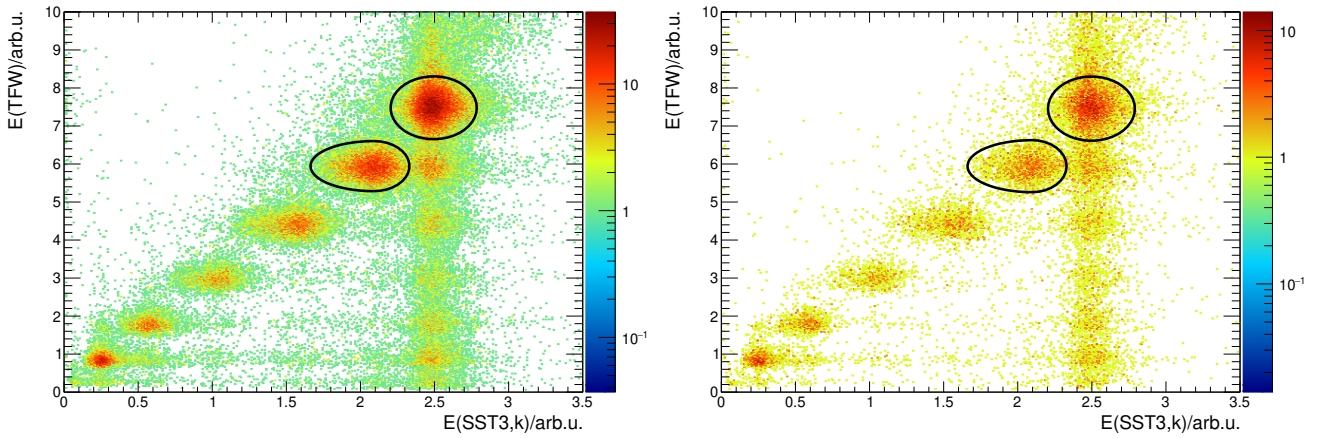

Figure A.9: Outgoing charge for setting 6 and the CH_2 (left) and the C (right) target. The applied cuts on outgoing $Z=6$ and $Z=7$ are shown in black. This plot is drawn for the *LAND* Tbit.

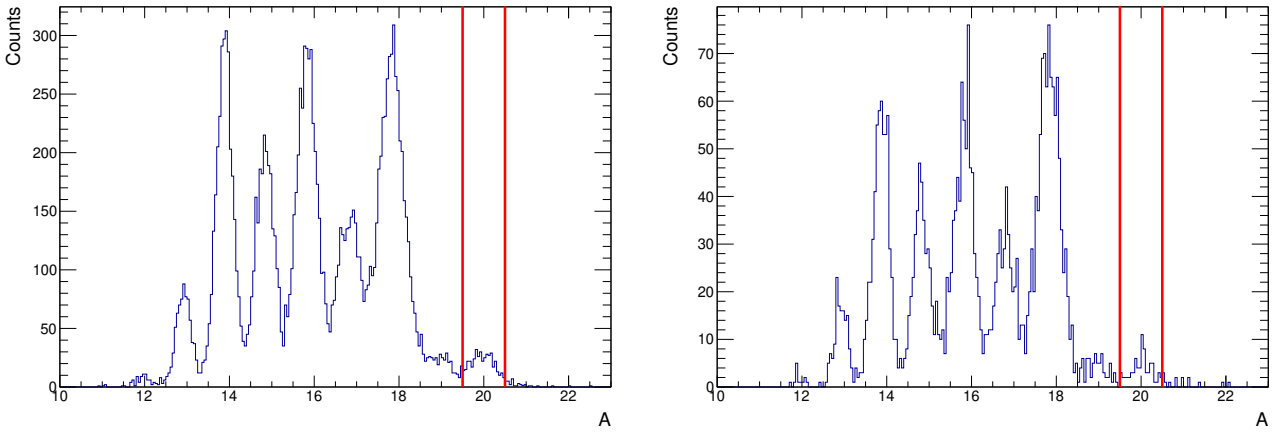

Figure A.10: Outgoing mass for setting 6 with a cut on $Z=6$ for the CH_2 (left) and the C (right) target. The applied cut on outgoing $A=20$ is shown in red. The plot is drawn without a trigger condition.

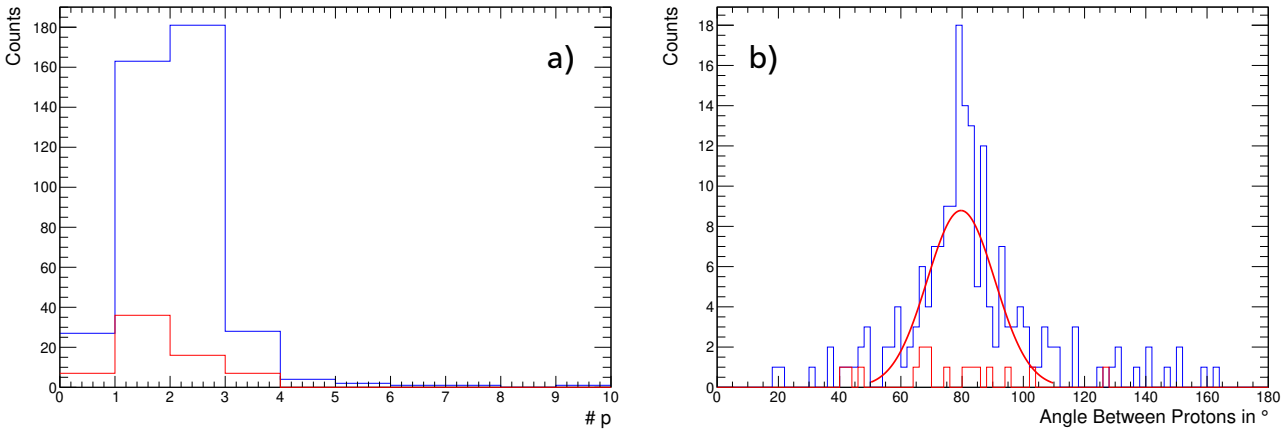

Figure A.11: a) Proton multiplicity and b) angle between two protons for the CH_2 (blue) and C target (red). The plots are shown for setting 6 for the *XB Sum* Tbit and in case of the angle in b) with a cut on events with exactly two protons. The angles of the protons are randomized over the whole area of the corresponding crystal. The angle between the two protons for the CH_2 target (blue) shows a peak at 79.7°.

Bibliography

[AAA+03] S. Agostinelli, J. Allison, K. Amako, et al. Geant4—a simulation toolkit. *Nuclear Instruments and Methods in Physics Research Section A: Accelerators, Spectrometers, Detectors and Associated Equipment*, 506(3):250–303, July 2003. doi:10.1016/s0168-9002(03)01368-8.

[AAA+06] J. Allison, K. Amako, J. Apostolakis, et al. Geant4 developments and applications. *IEEE Transactions on Nuclear Science*, 53(1):270–278, February 2006. doi:10.1109/tns.2006.869826.

[AAA+14] S. G. Altstadt, T. Adachi, Y. Aksyutina, et al. ^{13,14}B(n,γ) via Coulomb Dissociation for Nucleosynthesis towards the r-Process. *Nuclear Data Sheets*, 120:197–200, June 2014. doi:10.1016/j.nds.2014.07.045.

[AAA+16] J. Allison, K. Amako, J. Apostolakis, et al. Recent developments in GEANT4. *Nuclear Instruments and Methods in Physics Research Section A: Accelerators, Spectrometers, Detectors and Associated Equipment*, 835:186–225, November 2016. doi:10.1016/j.nima.2016.06.125.

[ABR13] T. Aumann, C. A. Bertulani, and J. Ryckebusch. Quasifree (p,2p) and (p,pn) reactions with unstable nuclei. *Physical Review C*, 88(6), December 2013. doi:10.1103/physrevc.88.064610.

[AEM+09] P. Adrich, D. Enderich, D. Miller, et al. A simulation tool for Recoil Distance Method lifetime measurements at NSCL. *Nuclear Instruments and Methods in Physics Research Section A: Accelerators, Spectrometers, Detectors and Associated Equipment*, 598(2):454–464, January 2009. doi:10.1016/j.nima.2008.09.055.

[AITS80] T. Ando, K. Ikeda, and A. Tohsaki-Suzuki. Nucleus-Nucleus Interaction and Nuclear Saturation Property: Microscopic Study of ^{16}O+^{16}O Interaction by New Effective Nuclear Force. *Progress of Theoretical Physics*, 64(5):1608–1626, November 1980. doi:10.1143/ptp.64.1608.

[APB+18] L. Atar, S. Paschalis, C. Barbieri, et al. Quasifree (p,2p) Reactions on Oxygen Isotopes: Observation of Isospin Independence of the Reduced Single-Particle Strength. *Physical Review Letters*, 120(5), January 2018. doi:10.1103/physrevlett.120.052501.

[AS87] F. Ajzenberg-Selove. Energy levels of light nuclei A = 18–20. *Nuclear Physics A*, 475(1):1–198, December 1987. doi:10.1016/0375-9474(87)90205-3.

[AS91] F. Ajzenberg-Selove. Energy levels of light nuclei A = 13–15. *Nuclear Physics A*, 523(1):1–196, February 1991. doi:10.1016/0375-9474(91)90446-D.

[BAM77] B. A. Brown, A. Arima, and J. B. McGrory. E2 core-polarization charge for nuclei near ^{16}O and ^{40}Ca. *Nuclear Physics A*, 277(1):77–108, February 1977. doi:10.1016/0375-9474(77)90263-9.

[Bar09] C. Barbieri. Role of Long-Range Correlations in the Quenching of Spectroscopic Factors. *Physical Review Letters*, 103(20), November 2009. doi:10.1103/physrevlett.103.202502.

[BBML77] G. Bertsch, J. Borysowicz, H. McManus, and W. G. Love. Interactions for inelastic scattering derived from realistic potentials. *Nuclear Physics A*, 284(3):399–419, July 1977. doi:10.1016/0375-9474(77)90392-x.

[BC84] Steve Baker and Robert D. Cousins. Clarification of the use of CHI-square and likelihood functions in fits to histograms. *Nuclear Instruments and Methods in Physics Research*, 221(2):437–442, April 1984. doi:10.1016/0167-5087(84)90016-4.

[BC10] C. A. Bertulani and C. De Conti. Pauli blocking and medium effects in nucleon knockout reactions. *Physical Review C*, 81(6), June 2010. doi:10.1103/physrevc.81.064603.

[BD04] Carlos A. Bertulani and Pawel Danielewicz. *Introduction to nuclear reactions*. Graduate Student Series in Physics. Institute of Physics Publishing, 2004.

[BEE+92] Th. Blaich, Th. W. Elze, H. Emling, et al. A large area detector for high-energy neutrons. *Nuclear Instruments and Methods in Physics Research Section A: Accelerators, Spectrometers, Detectors and Associated Equipment*, 314(1):136–154, April 1992. doi:10.1016/0168-9002(92)90507-Z.

[Ber17] Carlos Bertulani, May 2017. Private communication.

[BG06] C. A. Bertulani and A. Gade. MOMDIS: a Glauber model computer code for knockout reactions. *Computer Physics Communications*, 175(5):372–380, September 2006. doi:10.1016/j.cpc.2006.04.006.

[BH04] C. A. Bertulani and P. G. Hansen. Momentum distributions in stripping reactions of radioactive projectiles at intermediate energies. *Physical Review C*, 70(3), September 2004. doi:10.1103/physrevc.70.034609.

[BM69] Aage Bohr and Ben R. Mottelson. *Nuclear Structure – Single-Particle Motion*, volume 1. W. A. Benjamin, Inc., New York, 1969.

[BM75] Aage Bohr and Ben R. Mottelson. *Nuclear Structure – Nuclear Deformations*, volume 2. W. A. Benjamin, Inc., Reading, Massachuesetts, 1975.

[BMMR02] T. Bürvenich, D. G. Madland, J. A. Maruhn, and P.-G. Reinhard. Nuclear ground state observables and QCD scaling in a refined relativistic point coupling model. *Physical Review C*, 65(4), March 2002. doi:10.1103/physrevc.65.044308.

[BR97] Rene Brun and Fons Rademakers. ROOT — An object oriented data analysis framework. *Nuclear Instruments and Methods in Physics Research Section A: Accelerators,*

Spectrometers, Detectors and Associated Equipment, 389(1-2):81–86, April 1997. doi:10.1016/S0168-9002(97)00048-X. See also `http://root.cern.ch/`.

[BR03] Philip R. Bevington and D. Keith Robinson. *Data Reduction and Error Analysis for the Physical Sciences*. McGraw-Hill, 3rd edition, 2003.

[Bro11] B. Alex Brown. Lecture Notes in Nuclear Structure Physics. National Superconducting Cyclotron Laboratory and Department of Physics and Astronomy Michigan State University, E. Lansing, MI 48824, 2011.

[BT13] E. Browne and J. K. Tuli. Nuclear Data Sheets for A = 60. *Nuclear Data Sheets*, 114(12):1849–2022, December 2013. doi:10.1016/j.nds.2013.11.002.

[CAB+05] L. V. Chulkov, F. Aksouh, A. Bleile, et al. Quasi-free scattering with ^{6,8}He beams. *Nuclear Physics A*, 759(1-2):43–63, September 2005. doi:10.1016/j.nuclphysa.2005.05.148.

[CAB+06] A. Chester, P. Adrich, A. Becerril, et al. Application of the time-of-flight technique for lifetime measurements with relativistic beams of heavy nuclei. *Nuclear Instruments and Methods in Physics Research Section A: Accelerators, Spectrometers, Detectors and Associated Equipment*, 562(1):230–240, June 2006. doi:10.1016/j.nima.2006.02.182.

[Cae15] Christoph Caesar, January 2015. Private communication.

[Cas00] Richard F. Casten. *Nuclear Structure from a Simple Perspective*, volume 23 of *Oxford science publications*. Oxford University Press, Oxford, 2nd edition, 2000.

[CBH+98] E. Chabanat, P. Bonche, P. Haensel, J. Meyer, and R. Schaeffer. A Skyrme parametrization from subnuclear to neutron star densities Part II. Nuclei far from stabilities. *Nuclear Physics A*, 635(1-2):231–256, May 1998. doi:10.1016/s0375-9474(98)00180-8.

[Col17] Geant4 Collaboration. *Physics Reference Manual Release 10.4*, 2017.

[CSA+13] C. Caesar, J. Simonis, T. Adachi, et al. Beyond the neutron drip line: The unbound oxygen isotopes ^{25}O and ^{26}O. *Physical Review C*, 88(3), September 2013. doi:10.1103/PhysRevC.88.034313.

[CSG+98] J. Cub, G. Stengel, A. Grünschloß, et al. A large-area scintillating fibre detector for relativistic heavy ions. *Nuclear Instruments and Methods in Physics Research Section A: Accelerators, Spectrometers, Detectors and Associated Equipment*, 402(1):67–74, January 1998. doi:10.1016/s0168-9002(97)01078-4.

[Dol04] P. Doleschall. Influence of the short range nonlocal nucleon-nucleon interaction on the elastic n-d scattering: Below 30 MeV. *Physical Review C*, 69(5), May 2004. doi:10.1103/physrevc.69.054001.

[dS59] A. de Shalit. Effective Charge of Neutrons in Nuclei. *Physical Review*, 113(2):547–551, January 1959. doi:10.1103/physrev.113.547.

[EM03] D. R. Entem and R. Machleidt. Accurate charge-dependent nucleon-nucleon potential at fourth order of chiral perturbation theory. *Physical Review C*, 68(4), October 2003. doi:10.1103/physrevc.68.041001.

[fai18] FairRoot. `https://fairroot.gsi.de/`, March 2018.

[FAPC+18] P. Díaz Fernández, H. Alvarez-Pol, R. Crespo, et al. Quasifree (p,pN) scattering of light neutron-rich nuclei near N=14. *Physical Review C*, 97(2), February 2018. doi:10.1103/physrevc.97.024311.

[feb18] FEBEX3b. `https://www.gsi.de/work/forschung/experimentelektronik/digitalelektronik/digitalelektronik/module/font_end_module/febex/febex3b.htm`, April 2018.

[FMO+07] S. Fujii, T. Mizusaki, T. Otsuka, T. Sebe, and A. Arima. Microscopic shell-model description of the exotic nucleus ^{16}C. *Physics Letters B*, 650(1):9–14, June 2007. doi:10.1016/j.physletb.2007.04.067.

[FRN13] C. Forssén, R. Roth, and P. Navrátil. Systematics of 2^+ states in C isotopes from the no-core shell model. *Journal of Physics G: Nuclear and Particle Physics*, 40(5):055105, March 2013. doi:10.1088/0954-3899/40/5/055105.

[frs18] `https://www-win.gsi.de/frs-setup/AREAS.htm`, April 2018.

[GAB+92] H. Geissel, P. Armbruster, K. H. Behr, et al. The GSI projectile fragment separator (FRS): a versatile magnetic system for relativistic heavy ions. *Nuclear Instruments and Methods in Physics Research Section B: Beam Interactions with Materials and Atoms*, 70(1-4):286–297, August 1992. doi:10.1016/0168-583x(92)95944-m.

[gea18] `http://geant4.web.cern.ch/`, May 2018.

[GG08] A. Gade and T. Glasmacher. In-beam nuclear spectroscopy of bound states with fast exotic ion beams. *Progress in Particle and Nuclear Physics*, 60(1):161–224, January 2008. doi:10.1016/j.ppnp.2007.08.001.

[GKS+01] E. Gueorguieva, M. Kaci, C. Schück, et al. The recoil shadow anisotropy method. *Nuclear Instruments and Methods in Physics Research Section A: Accelerators, Spectrometers, Detectors and Associated Equipment*, 474(2):132–142, December 2001. doi:10.1016/s0168-9002(01)00877-4.

[GQN09] Doron Gazit, Sofia Quaglioni, and Petr Navrátil. Three-Nucleon Low-Energy Constants from the Consistency of Interactions and Currents in Chiral Effective Field Theory. *Physical Review Letters*, 103(10), September 2009. doi:10.1103/physrevlett.103.102502.

[GSI18] `https://www.gsi.de/en/researchaccelerators/accelerator_facility.htm`, April 2018.

[HCGR98] Z. Hu, R. Collatz, H. Grawe, and E. Roeckl. Energy and efficiency calibration of an array of six Euroball Cluster detectors used for beta-decay studies. *Nuclear Instruments and Methods in Physics Research Section A: Accelerators, Spectrometers, Detectors and Associated Equipment*, 419(1):121–131, December 1998. doi:10.1016/s0168-9002(98)01137-1.

[Hei15] Marcel Heine. *Measurement of (n,γ)-Rates of Light Neutron-Rich Nuclei for the r-Process Nucleosynthesis*. PhD thesis, Technische Universität Darmstadt, 2015.

[HJS49] Otto Haxel, J. Hans D. Jensen, and Hans E. Suess. On the "Magic Numbers" in Nuclear Structure. *Physical Review*, 75(11):1766–1766, June 1949. doi:10.1103/physrev.75.1766.2.

[HMM73] J. M. R. Hutchinson, W. B. Mann, and P. A. Mullen. Sum-peak counting with two crystals. *Nuclear Instruments and Methods*, 112(1-2):187–196, September 1973. doi:10.1016/0029-554X(73)90794-5.

[Hol14] Matthias Holl. *Quasi-Free Scattering from Relativistic Neutron-Deficient Carbon Isotopes*. PhD thesis, Technischen Universität Darmstadt, 2014.

[HS06] W. Horiuchi and Y. Suzuki. Structure of and E2 transition in ^{16}C in a ^{14}C+n+n model. *Physical Review C*, 73(3), March 2006. doi:10.1103/physrevc.73.037304.

[HS07] K. Hagino and H. Sagawa. Three-body model calculations for the ^{16}C nucleus. *Physical Review C*, 75(2), February 2007. doi:10.1103/physrevc.75.021301.

[HTB+78] G. Huber, F. Touchard, S. Büttgenbach, et al. Spins, magnetic moments, and isotope shifts of $^{21-31}$Na by high resolution laser spectroscopy of the atomic D_1 line. *Physical Review C*, 18(5):2342–2354, November 1978. doi:10.1103/physrevc.18.2342.

[HTW+17] M. Heine, S. Typel, M.-R. Wu, et al. Determination of the neutron-capture rate of ^{17}C for r-process nucleosynthesis. *Physical Review C*, 95(1), January 2017. doi:10.1103/physrevc.95.014613.

[IMA+00] H. Iwasaki, T. Motobayashi, H. Akiyoshi, et al. Low-lying intruder 1^- state in ^{12}Be and the melting of the N=8 shell closure. *Physics Letters B*, 491(1-2):8–14, October 2000. doi:10.1016/s0370-2693(00)01017-0.

[IOA+04] N. Imai, H. J. Ong, N. Aoi, et al. Anomalously Hindered E2 Strength B(E2;$2^+ \rightarrow 0^+$) in ^{16}C. *Physical Review Letters*, 92(6), February 2004. doi:10.1103/physrevlett.92.062501.

[Joh06] Håkan T. Johansson. *The DAQ always runs - Performing large scale nuclear physics experiments*. PhD thesis, Chalmers University of Technology, 2006.

[Joh18] Håkan T. Johansson. ucesb - unpack & check every single bit. `http://fy.chalmers.se/~f96hajo/ucesb/`, April 2018.

[Kah15] Julian Kahlbow. One-Neutron Removal Reactions on ^{11}Be & ^{12}Be. Master thesis, Technische Universtät Darmstadt, 2015.

[Kam14] Anwar Kamal. *Nuclear Physics*. Graduate Texts in Physics. Springer-Verlag Berlin Heidelberg, 2014.

[KE05] Y. Kanada-En'yo. Deformation of C isotopes. *Physical Review C*, 71(1), January 2005. doi:10.1103/physrevc.71.014310.

[KEKS13] Y. Kanada-En'yo, F. Kobayashi, and T. Suhara. Structures of ground and excited states in C isotopes. *Journal of Physics: Conference Series*, 445:012037, July 2013. doi:10.1088/1742-6596/445/1/012037.

[KH17] Aleksandra Kelic-Heil, November 2017. Private communication.

[Kno00] Glenn F. Knoll. *Radiation Detection and Measurement*. John Wiley & Sons, Inc., New York, 3rd edition, 2000.

[KNT+12] N. Kobayashi, T. Nakamura, J. A. Tostevin, et al. One- and two-neutron removal reactions from the most neutron-rich carbon isotopes. *Physical Review C*, 86(5), November 2012. doi:10.1103/physrevc.86.054604.

[Kra88] Kenneth S. Krane. *Introductory Nuclear Physics*. John Wiley & Sons, Inc., 1988.

[Læg79] E. Lægsgaard. Position-sensitive semiconductor detectors. *Nuclear Instruments and Methods*, 162(1-3):93–111, June 1979. doi:10.1016/0029-554x(79)90708-0.

[Leo94] William R. Leo. *Techniques for Nuclear and Particle Physics Experiments – A How-to Approach*. Springer-Verlag Berlin Heidelberg, 1994.

[Lin13] Simon Lindberg. Optimised Use of Detector Systems for Relativistic Radioactive Beams. Master thesis, Chalmers University of Technology, 2013.

[Mac01] R. Machleidt. High-precision, charge-dependent Bonn nucleon-nucleon potential. *Physical Review C*, 63(2), January 2001. doi:10.1103/physrevc.63.024001.

[May49] Maria Goeppert Mayer. On Closed Shells in Nuclei. II. *Physical Review*, 75(12):1969–1970, June 1949. doi:10.1103/physrev.75.1969.

[mbs18] `https://www.gsi.de/en/mbs`, April 2018.

[MDY10] Hai-Liang Ma, Bao-Guo Dong, and Yu-Liang Yan. Polarization effects and application to E2 transitions in even carbon isotopes. *Physics Letters B*, 688(2-3):150–153, May 2010. doi:10.1016/j.physletb.2010.03.067.

[ME11] R. Machleidt and D. R. Entem. Chiral effective field theory and nuclear forces. *Physics Reports*, 503(1):1–75, June 2011. doi:10.1016/j.physrep.2011.02.001.

[mGCK18a] mesytec GmbH & Co. KG. MHV-4. `http://www.mesytec.com/products/nuclear-physics/MHV-4.html`, April 2018.

[mGCK18b] mesytec GmbH & Co. KG. MPR-16. `http://www.mesytec.com/products/nuclear-physics/MPR-16.html`, April 2018.

[MHH+82] V. Metag, D. Habs, K. Helmer, et al. The Darmstadt-Heidelberg-Crystal-Ball. In *Proceedings of the Geiger Memorial Meeting*, October 1982.

[Mic15] Micron Semiconductor Ltd. Design X5 PSD E/PSD E readout across the strip length, 3D Assembly. Front and Rear View., February 2015. Technical drawing A-4381 and A-4382 provided by manufacturer together with detector.

[MII+95] T. Motobayashi, Y. Ikeda, K. Ieki, et al. Large deformation of the very neutron-rich nucleus ^{32}Mg from intermediate-energy Coulomb excitation. *Physics Letters B*, 346(1-2):9–14, March 1995. doi:10.1016/0370-2693(95)00012-a.

[MJP+09] K. Mahata, H. T. Johansson, S. Paschalis, H. Simon, and T. Aumann. Position reconstruction in large-area scintillating fibre detectors. *Nuclear Instruments and Methods in Physics Research Section A: Accelerators, Spectrometers, Detectors and Associated Equipment*, 608(2):331–335, September 2009. doi:10.1016/j.nima.2009.07.012.

[Mov13] Alina Movsesyan. *Quasi-free one-proton and one-neutron knockout reactions on ^{57}Ni*. PhD thesis, Technische Universität Darmstadt, 2013.

[MPF+14] A. O. Macchiavelli, M. Petri, P. Fallon, et al. Phenomenological analysis of B(E2) transition strengths in neutron-rich carbon isotopes. *Physical Review C*, 90(6):067305, December 2014. doi:10.1103/PhysRevC.90.067305.

[MSS96] R. Machleidt, F. Sammarruca, and Y. Song. Nonlocal nature of the nuclear force and its impact on nuclear structure. *Physical Review C*, 53(4):R1483–R1487, April 1996. doi:10.1103/physrevc.53.r1483.

[MW75] G. Mairle and G. J. Wagner. The decrease of ground-state correlations from ^{12}C to ^{14}C. *Nuclear Physics A*, 253(2):253–262, November 1975. doi:10.1016/0375-9474(75)90480-7.

[NAA+00] A. Navin, D. W. Anthony, T. Aumann, et al. Direct Evidence for the Breakdown of the N=8 Shell Closure in ^{12}Be. *Physical Review Letters*, 85(2):266–269, July 2000. doi:10.1103/physrevlett.85.266.

[Naj13] Mohammad Ali Najafi. *Quasi-free proton and neutron knockout reactions in ^{20}O*. PhD thesis, Rijksuniversiteit Groningen, 2013.

[NFH15] T. Neff, H. Feldmeier, and W. Horiuchi. Short-range correlations in nuclei with similarity renormalization group transformations. *Physical Review C*, 92(2), August 2015. doi:10.1103/physrevc.92.024003.

[OBC+01] A. Ozawa, O. Bochkarev, L. Chulkov, et al. Measurements of interaction cross sections for light neutron-rich nuclei at relativistic energies and determination of effective matter radii. *Nuclear Physics A*, 691(3-4):599–617, August 2001. doi:10.1016/S0375-9474(01)00563-2.

[OFU+01] Takaharu Otsuka, Rintaro Fujimoto, Yutaka Utsuno, et al. Magic Numbers in Exotic Nuclei and Spin-Isospin Properties of the NN Interaction. *Physical Review Letters*, 87(8), August 2001. doi:10.1103/physrevlett.87.082502.

[OIS+08] H. J. Ong, N. Imai, D. Suzuki, et al. Lifetime measurements of first excited states in ^{16,18}C. *Physical Review C*, 78(1):014308, July 2008. doi:10.1103/PhysRevC.78.014308.

[OMI+15] Yoshimune Ogata, Hiroshi Miyahara, Nobuhito Ishigure, et al. Development of a modified sum-peak method for activity determination of some gamma emitters. *Nuclear Instruments and Methods in Physics Research Section A: Accelera-*

tors, Spectrometers, Detectors and Associated Equipment, 775:34–40, March 2015. doi:10.1016/j.nima.2014.11.101.

[OSF+05] Takaharu Otsuka, Toshio Suzuki, Rintaro Fujimoto, Hubert Grawe, and Yoshinori Akaishi. Evolution of Nuclear Shells due to the Tensor Force. *Physical Review Letters*, 95(23), November 2005. doi:10.1103/physrevlett.95.232502.

[OSH+10] Takaharu Otsuka, Toshio Suzuki, Jason D. Holt, Achim Schwenk, and Yoshinori Akaishi. Three-Body Forces and the Limit of Oxygen Isotopes. *Physical Review Letters*, 105(3), July 2010. doi:10.1103/physrevlett.105.032501.

[Pan12] Valerii Panin. *Fully Exclusive Measurements of Quasi-Free Single-Nucleon Knockout Reactions in Inverse Kinematics*. PhD thesis, Technischen Universität Darmstadt, 2012.

[Pan16] Valerii Panin, March 2016. Private communication.

[Pas08] Stefanos Paschalis. *Relativistic One-Nucleon Removal Reactions*. PhD thesis, University of Liverpool, 2008.

[PFM+11] M. Petri, P. Fallon, A. O. Macchiavelli, et al. Lifetime Measurement of the 2_1^+ State in ^{20}C. *Physical Review Letters*, 107(10):102501, August 2011. doi:10.1103/PhysRevLett.107.102501.

[Pla18a] Ralf Plag. land02 - featuring the unofficial guide to the unofficial version of land02. `http://web-docs.gsi.de/~rplag/land02/`, February 2018. Only available with user and password.

[Pla18b] Ralf Plag. Some documentation on Ralf's tracker. `http://ralfplag.de/tracker/`, February 2018. Only available with user and password.

[PLM+13] S. Paschalis, I. Y. Lee, A. O. Macchiavelli, et al. The performance of the Gamma-Ray Energy Tracking In-beam Nuclear Array GRETINA. *Nuclear Instruments and Methods in Physics Research Section A: Accelerators, Spectrometers, Detectors and Associated Equipment*, 709:44–55, May 2013. doi:10.1016/j.nima.2013.01.009.

[PoPDG16] C. Patrignani and others (Particle Data Group). Review of Particle Physics. *Chinese Physics C*, 40(10):100001, October 2016. doi:10.1088/1674-1137/40/10/100001.

[PPC+12] M. Petri, S. Paschalis, R. M. Clark, et al. Structure of ^{16}C: Testing shell model and ab initio approaches. *Physical Review C*, 86(4):044329, October 2012. doi:10.1103/PhysRevC.86.044329.

[r3b18] R3BRoot - Simulations and Data Analysis for R3B. `https://www.r3broot.gsi.de/`, March 2018.

[RAA+16] Marko Röder, Tatsuya Adachi, Yulia Aksyutina, et al. Coulomb dissociation of ^{20,21}N. *Physical Review C*, 93(6), June 2016. doi:10.1103/physrevc.93.065807.

[Ray79] L. Ray. Proton-nucleus total cross sections in the intermediate energy range. *Physical Review C*, 20(5):1857–1872, November 1979. doi:10.1103/physrevc.20.1857.

[RNB88] S. Raman, C. W. Nestor, and K. H. Bhatt. Systematics of B(E2;$0_1^+ \rightarrow 2_1^+$) values for even-even nuclei. *Physical Review C*, 37(2):805–822, February 1988. doi:10.1103/PhysRevC.37.805.

[RNF10] Robert Roth, Thomas Neff, and Hans Feldmeier. Nuclear structure in the framework of the Unitary Correlation Operator Method. *Progress in Particle and Nuclear Physics*, 65(1):50–93, July 2010. doi:10.1016/j.ppnp.2010.02.003.

[RNJT01] S. Raman, C. W. Nestor Jr., and P. Tikkannen. Transition probability from the ground to the first-excited 2^+ state of even-even nuclides. *Atomic Data and Nuclear Data Tables*, 78(1):1–128, May 2001. doi:10.1006/adnd.2001.0858.

[RNT+18] G. Ribeiro, E. Nácher, O. Tengblad, et al. Structure of ^{13}Be studied in proton knockout from ^{14}B. *Physical Review C*, 98(2), August 2018. doi:10.1103/physrevc.98.024603.

[ROO18] ROOT - Data Analysis Framework Webpage. `http://root.cern.ch/`, May 2018.

[Ros09] Dominic M. Rossi. *Investigation of the Dipole Response of Nickel Isotopes in the Presence of a High-Frequency Electromagnetic Field*. PhD thesis, Johannes Gutenberg-Universität Mainz, 2009.

[SAD+04] M. Stanoiu, F. Azaiez, Zs. Dombrádi, et al. N=14 and 16 shell gaps in neutron-rich oxygen isotopes. *Physical Review C*, 69(3), March 2004. doi:10.1103/physrevc.69.034312.

[SGB+95] T. Suzuki, H. Geissel, O. Bochkarev, et al. Neutron Skin of Na Isotopes Studied via Their Interaction Cross Sections. *Physical Review Letters*, 75(18):3241–3244, October 1995. doi:10.1103/physrevlett.75.3241.

[SGB+96] H. Scheit, T. Glasmacher, B. A. Brown, et al. New Region of Deformation: The Neutron-Rich Sulfur Isotopes. *Physical Review Letters*, 77(19):3967–3970, November 1996. doi:10.1103/physrevlett.77.3967.

[SIN+15] D. Smalley, H. Iwasaki, P. Navrátil, et al. Lifetime measurements of ^{17}C excited states and three-body and continuum effects. *Physical Review C*, 92(6), December 2015. doi:10.1103/physrevc.92.064314.

[SIO+08] D. Suzuki, H. Iwasaki, H. J. Ong, et al. Lifetime measurements of excited states in ^{17}C: Possible interplay between collectivity and halo effects. *Physics Letters B*, 666(3):222–227, August 2008. doi:10.1016/j.physletb.2008.07.055.

[SP08] O. Sorlin and M.-G. Porquet. Nuclear magic numbers: New features far from stability. *Progress in Particle and Nuclear Physics*, 61(2):602–673, October 2008. doi:10.1016/j.ppnp.2008.05.001.

[SSM+08] R. Subedi, R. Shneor, P. Monaghan, et al. Probing Cold Dense Nuclear Matter. *Science*, 320(5882):1476–1478, June 2008. doi:10.1126/science.1156675.

[SSS+08] M. Stanoiu, D. Sohler, O. Sorlin, et al. Disappearance of the N=14 shell gap in the carbon isotopic chain. *Physical Review C*, 78(3):034315, September 2008. doi:10.1103/PhysRevC.78.034315.

[Sto17] Sonja Storck, March 2017. Private communication (poster presentation at DPG spring meeting 2017).

[Syn14] Ina Syndikus. Testing of Position Sensitive Silicon Detectors for the R^3B-Setup. Master thesis, Technische Universtität Darmstadt, 2014.

[Tan11] O. Tange. GNU Parallel - The Command-Line Power Tool. *;login: The USENIX Magazine*, 36(1):42–47, February 2011. doi:10.5281/zenodo.16303.

[THA+16] R. Thies, A. Heinz, T. Adachi, et al. Systematic investigation of projectile fragmentation using beams of unstable B and C isotopes. *Physical Review C*, 93(5), May 2016. doi:10.1103/physrevc.93.054601.

[THH+85] I. Tanihata, H. Hamagaki, O. Hashimoto, et al. Measurements of Interaction Cross Sections and Nuclear Radii in the Light p-Shell Region. *Physical Review Letters*, 55(24):2676–2679, December 1985. doi:10.1103/PhysRevLett.55.2676.

[Thi11] Ronja Thies. Prototype tests and pilot experiments for the R^3B scintillator-based detection systems. Master thesis, Chalmers University of Technology, 2011.

[THK+92] I. Tanihata, D. Hirata, T. Kobayashi, et al. Revelation of thick neutron skins in nuclei. *Physics Letters B*, 289(3-4):261–266, September 1992. doi:10.1016/0370-2693(92)91216-v.

[TYS+10] K. Tanaka, T. Yamaguchi, T. Suzuki, et al. Observation of a Large Reaction Cross Section in the Drip-Line Nucleus ^{22}C. *Physical Review Letters*, 104(6), February 2010. doi:10.1103/physrevlett.104.062701.

[VBB+12] P. Voss, T. Baugher, D. Bazin, et al. Excited-state transition-rate measurements in ^{18}C. *Physical Review C*, 86(1):011303, July 2012. doi:10.1103/PhysRevC.86.011303.

[VKL03] T. Vidmar, M. Korun, and A. Likar. Close-geometry efficiency calibration in gamma-ray spectrometry using radio-nuclides with a two-step cascade decay. *Nuclear Instruments and Methods in Physics Research Section A: Accelerators, Spectrometers, Detectors and Associated Equipment*, 508(3):404–413, August 2003. doi:10.1016/s0168-9002(03)01729-7.

[VLS+17] M. Vandebrouck, A. Lepailleur, O. Sorlin, et al. Effective proton-neutron interaction near the drip line from unbound states in ^{25,26}F. *Physical Review C*, 96(5), November 2017. doi:10.1103/physrevc.96.054305.

[Wam11] Felix Wamers. *Quasi-Free-Scattering and One-Proton-Removal Reactions with the Proton-Dripline Nucleus ^{17}Ne at Relativistic Beam Energies*. PhD thesis, Technischen Universität Darmstadt, 2011.

[WAW+12] M. Wang, G. Audi, A. H. Wapstra, et al. The Ame2012 atomic mass evaluation. *Chinese Physics C*, 36(12):1603–2014, December 2012. doi:10.1088/1674-1137/36/12/003.

[WB92] E. K. Warburton and B. A. Brown. Effective interactions for the 0p1s0d nuclear shell-model space. *Physical Review C*, 46(3):923–944, September 1992. doi:10.1103/physrevc.46.923.

[WBB90] E. K. Warburton, J. A. Becker, and B. A. Brown. Mass systematics for A=29–44 nuclei: The deformed A∼32 region. *Physical Review C*, 41(3):1147–1166, March 1990. doi:10.1103/physrevc.41.1147.

[WBB+10] A. H. Wuosmaa, B. B. Back, S. Baker, et al. ^{15}C(d,p)^{16}C Reaction and Exotic Behavior in ^{16}C. *Physical Review Letters*, 105(13), September 2010. doi:10.1103/physrevlett.105.132501.

[Wei18a] Helmut Weick. ATIMA. `http://web-docs.gsi.de/~weick/atima/`, April 2018.

[Wei18b] Helmut Weick. MOCADI. `https://web-docs.gsi.de/~weick/mocadi/`, May 2018.

[WFM+08] M. Wiedeking, P. Fallon, A. O. Macchiavelli, et al. Lifetime Measurement of the First Excited 2^+ State in ^{16}C. *Physical Review Letters*, 100(15), April 2008. doi:10.1103/physrevlett.100.152501.

[WKK+10] K. Wimmer, T. Kröll, R. Krücken, et al. Discovery of the Shape Coexisting 0^+ State in ^{32}Mg by a Two Neutron Transfer Reaction. *Physical Review Letters*, 105(25), December 2010. doi:10.1103/physrevlett.105.252501.

[WS54] Roger D. Woods and David S. Saxon. Diffuse Surface Optical Model for Nucleon-Nuclei Scattering. *Physical Review*, 95(2):577–578, July 1954. doi:10.1103/physrev.95.577.

[WSI+15] K. Whitmore, D. Smalley, H. Iwasaki, et al. Magnetic response of the halo nucleus ^{19}C studied via lifetime measurement. *Physical Review C*, 91(4), April 2015. doi:10.1103/physrevc.91.041303.

[WSS95] R. B. Wiringa, V. G. J. Stoks, and R. Schiavilla. Accurate nucleon-nucleon potential with charge-independence breaking. *Physical Review C*, 51(1):38–51, January 1995. doi:10.1103/physrevc.51.38.

[Y+06] W.-M. Yao et al. Review of Particle Physics. *Journal of Physics G: Nuclear and Particle Physics*, 33(1):1–1232, July 2006. doi:10.1088/0954-3899/33/1/001.

[YKNA79] N. Yamaguchi, T. Kasahara, S. Nagata, and Y. Akaishi. Effective Interaction with Three-Body Effects. *Progress of Theoretical Physics*, 62(4):1018–1034, October 1979. doi:10.1143/ptp.62.1018.

[YMR+11] J. M. Yao, J. Meng, P. Ring, et al. Microscopic description of quantum shape fluctuation in C isotopes. *Physical Review C*, 84(2), August 2011. doi:10.1103/physrevc.84.024306.

[Yuk35] Hideki Yukawa. On the Interaction of Elementary Particles. I. *Proceedings of the Physico-Mathematical Society of Japan*, 17:48–57, 1935. doi:10.1143/ptps.1.1.

[Zuc08] P. Zuccon. The AMS silicon tracker: Construction and performance. *Nuclear Instruments and Methods in Physics Research Section A: Accelerators, Spectrometers, Detectors and Associated Equipment*, 596(1):74–78, October 2008. doi:10.1016/j.nima.2008.07.116.

List of Figures

List of Tables

Acronyms

ADC	Analog-to-Digital Converter
ALADIN	A Large Acceptance DIpole magNet
AMD	Antisymmetrized Molecular Dynamics
AMP	Angular Momentum Projection
AMS	Alpha Magnetic Spectrometer
BCS	Bardeen-Cooper-Schriefer
CFD	Constant Fraction Discriminator
c.m.	Center-of-Mass
DAQ	Data Acquisition
DTF	Dicke ToF Wand
DWBA	Distorted Wave Born Approximation
DWIA	Distorted Wave Impulse Approximation
FEBEX3b	Front-End Board with optical link EXtension 3b
FRS	FRagment Separator
GCM	Generator Coordinate Method
GFI	Großer FIber detector
GSI	GSI Helmholtzzentrum für Schwerionenforschung GmbH
HF	Hartree-Fock
HV	High Voltage
ID	IDentification
ISS	International Space Station
IT-NCSM	Importance Truncated NCSM
KVI-CART	KVI-Center for Advanced Radiation Technology
LAND	Large Area Neutron Detector
lmd	List Mode Data
MBS	Multi Branch System
MPPC	Multi-Pixel Photon Counter
MT	empty
NCSM	No Core Shell Model
NN	Next-Neighbor
NNN	Next-to-Next-Neighbor
NSCL	National Superconducting Cyclotron Laboratory
PAV	Projection After Variation
PDC	Proton Drift Chamber

PMT	Photo Multiplier Tube
POS	POSition detector
PSP	Position Sensitive Pin diode
PSPM	Position-Sensitive PMT
QDC	Charge-to-Digital Converter
QFS	Quasi-Free Scattering
R^3B	Reactions with Relativistic Radioactive Beams
RDM	Recoil Distance Method
RMF	Relativistic Mean Field
r.m.s.	Root-Mean-Square
ROLU	Rechts-Oben-Links-Unten
RSM	Recoil Shadow Method
SIDEREM	SIlicon DEtector REadout Module
SIS18	SchwerIonenSynchrotron18
SRG	Similarity Renormalization Group
SSD	Silicon Strip Detector
Tbit	Trigger BIT
TDC	Time-to-Digital Converter
TFW	Time-of-Flight Wall
TOF	Time-Of-Flight
Tpat	Trigger PATtern
UCOM	Unitary Correlation Operator Method
UNILAC	UNIversal Linear ACcelerator
XB	Crystal Ball

Acknowledgment

This work could not be finished without the help and encouragement of others. First of all, I want to thank Marina Petri for giving me the possibility to work on this topic in her group. I appreciated the direct supervision and the interest in my topic. Thanks for the possibility to travel and to participate in several other experiments. The insight into different labs were very interesting and helped me to figure out in which environment I want to work. I enjoyed a lot the very productive visits in York. Together with a cider or two. :)

In addition, I want to thank Tom Aumann for being my second supervisor and welcoming me as part of his group. His comments on my work were always a great help. The different focus of his work was a personal gain. I appreciated the participation in the experiments at RIKEN, in which I learned a lot. And I fell in love with Japanese food.

I want to thank Stefanos Paschalis to draw my interest to silicon detectors. Although sometimes stressfull, I liked the possibility to have a side project in the lab. The discussion with him and later Dominic Rossi made me understand the detector and the setup even better. I also want to thank Sonja Storck for several years of hands-on help during preparation and beam times.

During the last six years, I got to know a lot of great people. And I wanted to say "Thank you" for the time together. I always appreciated the good mood and the willingness to help and to solve problems. In particular, I want to thank Marc Duchene for the help with formalities, Vadim Wagner for the R3BRoot support, and Julian Kahlbow for his knowledge of the R^3B setup and his willingness to share it. Andrea Horvat, Chris Lehr, Dima Symochko, Fabia Schindler, Joachim Tscheuschner, Michael Mathy, and Sonja Storck has to be thanked for a lot of – more or less – fruitfull discussions and all the nights out with more than one drink. And also everyone of our group – past and present members – whom I did not name. I will always remember the ifridge BBQs and the nights we went out for drinks in Tokio.

Thanks for proof reading to Ashton Falduto, Chris Lehr, Michael Mathy, Sebastian Heil, and Sonja Storck. Without them the thesis would be much harder to read ... and to understand.

Des Weiteren möchte ich all meinen Freunden danken. Für gute Gespräche und gutes Essen. Für Spiele, Musik und lange Nächte. Für die Geduld, wenn ich mal wieder viel beschäftigt oder im Ausland war. Für all die Ablenkung. Für die Welt außerhalb der Physik.

Außerdem ein großes "Danke" an meine Familie für die Unterstützung in jeder Hinsicht. An meine Eltern Manu und Rudolf, die mich während meines Studiums finanziell unterstützt und immer an mich geglaubt haben. An meine Schwester Sarah für die Ablenkung und das Aufzeigen ganz anderer Welten. Und an Familie Heil, dafür dass sie ein Ruhepol ist.

Und zu guter Letzt: Sebastian, für alles und noch viel mehr! <3

Erklärung zur Dissertation

Hiermit versichere ich, die vorliegende Dissertation ohne Hilfe Dritter nur mit den angegebenen Quellen und Hilfsmitteln angefertigt zu haben. Alle Stellen, die aus Quellen entnommen wurden, sind als solche kenntlich gemacht. Diese Arbeit hat in gleicher oder ähnlicher Form noch keiner Prüfungsbehörde vorgelegen.

Darmstadt, den 20. Juni 2019

(Ina Syndikus)